

# **Electrochemical Aptasensing of B-Type Natriuretic Peptide-A Biomarker for Myocardial Infarction**



By

**Marlon Oranzie (BSc Honours)**

A thesis submitted in partial fulfilment of the requirements for the degree

Of

**MAGISTER SCIENTIAE IN NANOSCIENCE**

Faculty of Natural Science

University of the Western Cape, South Africa

Supervisor: Prof Emmanuel Iwuoha

Co-supervisors: Dr Samantha Douman

November 2019

## ABSTRACT

Myocardial infarction (MI) affects many parts of the western world and in South Africa alone it is estimated that MI is responsible for 1 in 6 deaths (17.3%). Traditional diagnostic methods for MI include an electrocardiograms and blood tests. The problem with these diagnostic methods are that they are time consuming, require large sample volumes, expensive equipment and complicated machinery. To achieve early detection of MI the discovery of specific, sensitive and reliable biomarkers are required. Brain natriuretic peptide (BNP) has been identified as a reliable biomarker for MI due to the fact that it has a defined cutoff of 100 pg/ml and it is not susceptible to patient's age which could make early detection of BNP complicated. Early detection methods for BNP has been based on immunoradiometric assays but problems associated with immunoradiometric assays are that there is a restricted availability of antigens and incubation of the labeled antibody could take up to two weeks which affects the patients waiting time on results. Electrochemical biosensors are emerging as early detection method for MI because they can be designed to be sensitive, specific to BNP at a low cost. This research study reported for the first the successful fabrication and implementation of highly sensitive mercaptosuccinic acid capped nickel selenide quantum dots (MSA-NiSe<sub>2</sub> QDs) aptasensor for the detection of BNP. The poly-dispersed MSA-NiSe<sub>2</sub> QDs were synthesized via an inexpensive, simple and reproducible aqueous microwave assisted irradiation method. The prepared MSA-NiSe<sub>2</sub> QDs were characterized by Ultraviolet spectroscopy (UV-Vis), X-ray Diffraction (XRD), Fourier Transform Infrared spectroscopy (FTIR), High Resolution Transmission/Scanning Electron Microscopy (HR TEM/SEM) and Small Angle X-ray Scattering (SAXSpace). The electrochemical properties of the MSA-NiSe<sub>2</sub> QDs were investigated by Cyclic Voltammetry (CV) and Electrochemical Impedance Spectroscopy

(EIS). HR-TEM revealed the formation of small sized MSA-NiSe<sub>2</sub> QDs about 4 nm in diameter which was complemented by SAXSpace. UV-Vis studies showed absorption peaks in the ultraviolet region (100-400 nm) confirming the small size of these QDs as well confirming the direct and indirect bandgap of the QDs. XRD confirmed that the QDs are crystalline and belong to the bulk cubic MSA-NiSe<sub>2</sub> QDs phase. FTIR studies confirmed the successful capping of MSA on the QDs due to the disappearance of the thiol peak at 2652 cm<sup>-1</sup>. Electrochemical studies revealed that the MSA-NiSe<sub>2</sub> QDs showed good electrochemical properties on screen printed carbon electrodes (SPCE) which allowed them to be used as a mediating platform between the aptamer and SPCE. The successful detection of BNP was achieved by an incubation process between the aptamer drop coated on the MSA-NiSe<sub>2</sub> QDs/SPCE surface overnight. The response of the MSA-NiSe<sub>2</sub> QDs based aptasensor towards different concentrations of BNP was studied by differential pulse voltammetry (DPV). DPV showed a good linearly with correlation coefficient of  $R^2 = 0.98$ . DPV also showed a high sensitivity (0.4513  $\mu\text{A}/\text{pg/mL}$ ) towards detecting BNP with a detection limit of 11.93 pg/ml. The value of 11.93 pg/ml falls within the negative predictive value range of 10-100 pg/ml for early-stage diagnosis of BNP.

## **KEYWORDS**

BNP- Brain natriuretic peptide

LOD- Limit of detection

LOQ- Limit of quantification

MI- Myocardial infarction

MSA-NiSe<sub>2</sub>-QDs- Mercaptosuccinic acid capped nickel selenide quantum dots

DPV- Differential pulse voltammetry

## **ABBREVIATIONS**

AChE- Acetylcholine esterase

ANP- Arterial natriuretic peptide

AuE- Gold electrode

BNP-Brain natriuretic peptide

CdSe-Cadmium selenide

CdTe-Cadmium telluride

Ck-MB-Creatine kinase isoenzyme

CNP- C-type natriuretic peptide

CV-Cyclic voltammetry

DNA-Deoxyribonucleic acid

dsDNA- Double stranded DNA

DPV-Deep pulse voltammetry

ECG-Electrocardiogram

EDC-1-ethyl-3-(3-dimethylaminopropyl) carbodiimide

EGFR-Epidermal growth factor receptor

EIS-Electrochemical impedance spectroscopy

FTIR-Fourier transform infrared spectroscopy

GCE-Glassy carbon electrode

GSH-Gluthathione

HER2-Human epidermal growth factor receptor 2

HR-SEM- High resolution scanning electron microscopy

HR-TEM-High resolution transmission electron microscopy

LOD- Limit of detection

LOQ-Limit of quantification

MES- Mercaptoethanesulfanone

MI- Myocardial infarction

MPA- Mercaptopropionic acid

MSA- Mercaptosuccinic acid

NaHB<sub>4</sub>- Sodium borohydride

NHS-n-hydroxysuccimide

NiCl<sub>2</sub>.6H<sub>2</sub>O- Nickel chloride hexahydrate

NPR-A-Natriuretic peptide receptor type A

NT-proBNP- N-terminal fragment proBNP

PCR- Polymerase chain reaction

QDs- Quantum dots

SAXSpace- Small angle X-ray scattering

Se- Selenium

SiO<sub>2</sub>- Silicon dioxide

SPCE- Screen printed carbon electrode

SPGE- Screen printed gold electrode

ssDNA- Single stranded DNA

TOPO- Trioctylphosphine oxide

UV-Vis- Ultraviolet-visible spectroscopy

XRD- X-ray diffraction

WHO- World health organization

## DECLARATION

I declare that Electrochemical Aptasensing of B-Type Natriuretic Peptide-A Biomarker for Myocardial Infarction is my own work, that it has not been submitted before for any degree or examination in any other university, and that all the sources I have used or quoted have been indicated and acknowledged as complete references.



Signature -----

**Marlon Oranzie**

**November 2019**

## **DEDICATION**

This work is dedicated to my family; Elroy Oranzie (Father), Mary-Ann Oranzie (Mother), Leroy Oranzie (brother), Terri Francheschini (sister), Wilhelmina Malgas (grandmother), Rose Bruntjies (grandmother), Staycer Malgas (cousin), Marzelle Klink (cousin), Anthea Taylor (cousin), Gaynor Malgas (cousin), Liezil Malgas (cousin), Kyle Malgas (cousin) and Girshwin Malgas (cousin).

## **ACKNOWLEDGEMENTS**

I would like to thank God for the strength and motivation to complete my work.

A special thanks to my supervisor, Prof Emmanuel Iwuoha, for his support, guidance and for believing in me throughout my studies.

To my co-supervisor Dr Samantha Douman thank you for believing in me and for giving me advice that I will definitely carry with me throughout my entire career as researcher.

To my family and friends, without your love and support this journey would have definitely been a difficult one.

To the chemistry department and sensor lab researchers, thank you for your support and friendship.

## LIST OF PUBLICATIONS

Marlon Oranzie, Samantha Douman and Emmanuel I. Iwuoha, Novel MSA-NiSe<sub>2</sub> QDs based Aptasensor for detection of BNP, a Biomarker for Cardiovascular Disease.

*Submitted.*

# TABLE OF CONTENTS

<b>ABSTRACT</b> .....	<b>i</b>
<b>KEYWORDS</b> .....	<b>iii</b>
<b>ABBREVIATIONS</b> .....	<b>iv</b>
<b>DECLARATION</b> .....	<b>vii</b>
<b>DEDICATION</b> .....	<b>viii</b>
<b>ACKNOWLEDGEMENTS</b> .....	<b>ix</b>
<b>LIST OF PUBLICATIONS</b> .....	<b>x</b>
<b>TABLE OF CONTENTS</b> .....	<b>xi</b>
<b>LIST OF SYMBOLS</b> .....	<b>xvi</b>
<b>LIST OF FIGURES</b> .....	<b>xviii</b>
<b>LIST OF SCHEMES</b> .....	<b>xxiv</b>
<b>LIST OF TABLES</b> .....	<b>xxvi</b>
<b>LIST OF EQUATIONS</b> .....	<b>xxvii</b>
<b>1</b> <b>CHAPTER 1: Introduction</b> .....	<b>1</b>
1.1 <b>Background</b> .....	<b>1</b>
1.2 <b>Problem statement, research aims, approach and objectives</b> .....	<b>4</b>
1.3 <b>Conclusion</b> .....	<b>6</b>
<b>2</b> <b>CHAPTER 2: Literature Review</b> .....	<b>10</b>
2.1 <b>Quantum dots</b> .....	<b>10</b>
2.1.1 <b>Capping Agents</b> .....	<b>13</b>

2.1.1.1	<b>Mercaptosuccinic Acid.....</b>	<b>15</b>
2.2	<b>Self-assembled monolayer .....</b>	<b>16</b>
2.3	<b>Biomarkers.....</b>	<b>17</b>
2.3.1	<b>Brain natriuretic peptide (BNP) .....</b>	<b>19</b>
2.3.1.1	<b>Immunoradiometric assay .....</b>	<b>20</b>
2.4	<b>Electrochemical biosensors .....</b>	<b>22</b>
2.4.1	<b>Aptasensors.....</b>	<b>24</b>
2.5	<b>Characterization Techniques .....</b>	<b>27</b>
2.5.1	<b>Spectroscopic Techniques .....</b>	<b>27</b>
2.5.1.1	<b>Ultraviolet-Visible Spectroscopy.....</b>	<b>27</b>
2.5.1.2	<b>Fourier-Transform Infrared Spectroscopy .....</b>	<b>29</b>
2.5.1.3	<b>X-ray diffraction.....</b>	<b>30</b>
2.5.1.4	<b>Small Angle X-ray Scattering .....</b>	<b>32</b>
2.5.2	<b>Microscopic Techniques .....</b>	<b>33</b>
2.5.2.1	<b>High Resolution Transmission Electron Microscopy (HR-TEM) ..</b>	<b>33</b>
2.5.2.2	<b>High Resolution Scanning Electron Microscopy (HR-SEM) .....</b>	<b>35</b>
2.5.3	<b>Electrochemical Techniques .....</b>	<b>36</b>
2.5.3.1	<b>Cyclic voltammetry .....</b>	<b>36</b>
2.5.3.2	<b>Differential pulse voltammetry (DPV) .....</b>	<b>38</b>
2.5.3.3	<b>Electrochemical Impedance Spectroscopy (EIS).....</b>	<b>39</b>
2.6	<b>Conclusion.....</b>	<b>44</b>

<b>3</b>	<b>CHAPTER 3: Experimental</b> .....	<b>56</b>
<b>3.1</b>	<b>Reagents</b> .....	<b>56</b>
<b>3.2</b>	<b>Instrumentation</b> .....	<b>56</b>
<b>3.3</b>	<b>Procedure</b> .....	<b>57</b>
<b>3.3.1</b>	<b>Synthesis of MSA capped NiSe-QDs</b> .....	<b>57</b>
<b>3.3.1.1</b>	<b>Preparation of the sodium hydrogen selenide solution</b> .....	<b>57</b>
<b>3.3.1.2</b>	<b>Preparation of the MSA-NiCl<sub>2</sub> ion solution</b> .....	<b>58</b>
<b>3.4</b>	<b>Sample preparation</b> .....	<b>58</b>
<b>3.4.1</b>	<b>Ultraviolet-visible spectroscopy</b> .....	<b>58</b>
<b>3.4.2</b>	<b>Fourier Transform Infra-Red Spectroscopy</b> .....	<b>59</b>
<b>3.4.3</b>	<b>X-Ray Diffraction</b> .....	<b>59</b>
<b>3.4.4</b>	<b>Small Angle X-ray Scattering</b> .....	<b>59</b>
<b>3.4.5</b>	<b>High Resolution Transmission Electron Microscopy</b> .....	<b>59</b>
<b>3.4.6</b>	<b>High Resolution Scanning Electron Microscopy</b> .....	<b>60</b>
<b>3.4.7</b>	<b>Cyclic voltammetry</b> .....	<b>60</b>
<b>3.4.7.1</b>	<b>Preparation of MSA-NiSe<sub>2</sub>-QDs on conventional gold electrodes</b> ..	<b>60</b>
<b>3.4.7.2</b>	<b>Preparation of MSA-NiSe<sub>2</sub>-QDs on screen printed gold electrodes</b>	<b>61</b>
<b>3.4.7.3</b>	<b>Preparation of MSA-NiSe<sub>2</sub>-QDs on conventional glassy carbon electrodes</b> .....	<b>61</b>
<b>3.4.7.4</b>	<b>Preparation of MSA-NiSe<sub>2</sub>-QDs on screen printed carbon electrodes</b> .....	<b>62</b>

3.5	Fabrication of the MSA-NiSe <sub>2</sub> -QDs dots aptasensor .....	62
3.6	Conclusion.....	65
4	Chapter 4:.....	67
4.1	Results and discussion.....	67
4.1.1	Spectroscopic Techniques .....	67
4.1.1.1	Ultraviolet-visible spectroscopy (UV-Vis).....	67
4.1.1.2	Fourier transform infrared (FT-IR) Spectroscopy .....	70
4.1.1.3	X-ray diffraction (XRD) .....	71
4.1.1.4	Small Angle X-ray Scattering .....	73
4.1.2	Microscopic Techniques .....	76
4.1.2.1	High resolution transmission electron microscopy (HR-TEM) .....	76
4.1.2.2	High resolution scanning electron microscopy (HR-SEM) .....	78
4.1.3	Electrochemical techniques.....	82
4.1.3.1	Cyclic Voltammetry (CV).....	82
4.1.3.2	Electrochemical impedance spectroscopy (EIS).....	94
4.1.4	Characterization of the MSA-NiSe <sub>2</sub> -QDs Aptasensor .....	97
4.1.4.1	Sensor Fabrication .....	97
4.1.4.1.1	Cyclic Voltammetry (CV) .....	97
4.1.4.1.2	Electrochemical Impedance Spectroscopy (EIS) .....	98
4.1.4.2	Detection of brain natriuretic peptide (BNP) .....	100
4.1.4.2.1	Differential Pulse Voltammetry (DPV) .....	100

<b>4.2</b>	<b>Conclusion.....</b>	<b>105</b>
<b>5</b>	<b>CHAPTER 5: Conclusions and Recommendations.....</b>	<b>113</b>
<b>5.1</b>	<b>Conclusions .....</b>	<b>113</b>
<b>5.2</b>	<b>Recommendations .....</b>	<b>117</b>

## LIST OF SYMBOLS

**A- Geometric area of electrode**

**d- Interplanar spacing**

**$E_p$ - Peak potential**

**$E_{pa}$ - Anodic peak potential**

**$E_{pc}$ - Cathodic peak potential**

**$I_p$ - Peak Current**

**$I_{pa}$ - Anodic peak current**

**$I_{pc}$ - Cathodic peak current**

**$D_0$ - Diffusion coefficient**

**$C_0$ - Concentration**

**k- Scherrer constant**

**R- Ideal gas constant**

**$\theta$  – Theta**

**$\beta$  - Beta**

**$h$ - Plancks constant**

**$\alpha$ - absorption coefficient**

**$\nu$ - Scan rate**

**$\Gamma$ - Surface concentration**

**$\lambda$ - Wavelength**

**T- Temperature**

**$\omega$ - Radial frequency**

## LIST OF FIGURES

<b>Figure 1.1: Myocardial infarction illustration adapted from F. Moccetti and co-workers, Myocardial Infarction Produces Sustained Proinflammatory Endothelial Activation in Remote Arteries, <i>J. Am. Coll. Cardiol.</i>, 2018, 72, 1015–1026.....</b>	<b>2</b>
<b>Figure 2.1: Illustration of the different types of nanomaterials. Reprinted from S. Wu, L. Cheng and Q. Wang, Excitonic effects and related properties in semiconductor nanostructures: Roles of size and dimensionality, <i>Mater. Res. Express</i>, 2017,4,1-12.....</b>	<b>11</b>
<b>Figure 2.2: Quantum confinement of QDs based on shape and size dependences. Reprinted from J. McKittrick and L. E. Shea-Rohwer, Review: Down conversion materials for solid-state lighting, <i>J. Am. Ceram. Soc.</i>, 2014, 97, 1327–1352.....</b>	<b>12</b>
<b>Figure 2.3: Examples of capping agents. Reprinted from C. M. Phan and H. M. Nguyen, Role of Capping Agent in Wet Synthesis of Nanoparticles, <i>J. Phys. Chem. A</i>, 2017, 121, 3213–3219.....</b>	<b>14</b>
<b>Figure 2.4: Representation of MSA-Capped NiSe QDs .....</b>	<b>15</b>
<b>Figure 2.5: Operating principle of UV-Vis Spectroscopy. Reprinted from R. Wegh, H. Donker, A. Meijerink, R. Lamminmäki and J. Hölsä, Vacuum-ultraviolet spectroscopy and quantum cutting for, <i>Phys. Rev. B - Condens. Matter Mater. Phys.</i>, 1997, 56, 13841–13848. ....</b>	<b>28</b>
<b>Figure 2.6: Typical working principle of XRD. Reprinted from A. A. Bunaciu, E. gabriela Udriștioiu and H. Y. Aboul-Enein, X-Ray Diffraction: Instrumentation and Applications, <i>Crit. Rev. Anal. Chem.</i>, 2015, 45, 289–299.....</b>	<b>31</b>

<b>Figure 2.7: SAXSpace working principle. Reprinted from H. D. T. Mertens and D. I. Svergun, Structural characterization of proteins and complexes using small-angle X-ray solution scattering, <i>J. Struct. Biol.</i>, 2010, 172, 128–141.....</b>	<b>32</b>
<b>Figure 2.8: HR-TEM operating principle. Reprinted from G. C. Capitani and M. Mellini, High-resolution transmission electron microscopy (HRTEM) investigation of antigorite polysomes (m = 15 to 18), <i>Am. Mineral.</i>, 2007, 92, 64–71. ....</b>	<b>34</b>
<b>Figure 2.9: A typical SEM image of CdSe/ZnS quantum dots. Reprinted from H. Zhang, P. Wang, Q. Zhou and Y. Wang, A Novel Method for the Detection of Chlorpyrifos by Combining Quantum Dot-labeled Molecularly Imprinted Polymer with Flow Cytometry, <i>Anal. Lett.</i>, 2018, 51, 921–934.....</b>	<b>35</b>
<b>Figure 2.10: A typical Cyclic voltamogramme. Reprinted from H. Borchert, Solar Cells Based on Colloidal Nanocrystals, <i>Springer Ser. Mater. Sci.</i>, 978-3-319.....</b>	<b>37</b>
<b>Figure 2.11: Typical DPV graph. Reprinted from (W. Wu, Y. Fang, C. Zhu, S. Chen, T. Li, L. Wu, N. Bao, Y. Liu and H. Gu, Fabrication of highly stable and sensitive electrochemical sensor from hemoglobin-Au nanocomposites and its analytical applications, <i>RSC Adv.</i>, 2017, 7, 42884–42890.....</b>	<b>39</b>
<b>Figure 2.12: Current response to an applied sinusoidal potential in a linear EIS system. Reprinted from J. Halliwell, A. C. Savage, N. Buckley and C. Gwenin, Electrochemical impedance spectroscopy biosensor for detection of active botulinum neurotoxin, <i>Sens. Bio-Sensing Res.</i>, 2014, 2, 12–15.....</b>	<b>40</b>
<b>Figure 2.13: Typical Nyquist plots for EIS. Reprinted from 1R. Ramachandran, V. Mani, S. M. Chen, G. Gnanakumar and M. Govindasamy, Recent developments in electrode materials and methods for pesticide analysis - An overview, <i>Int. J. Electrochem. Sci.</i>, 2015, 10, 859–869.</b>	<b>42</b>

**Figure 2.14: A typical Bode plot. Reprinted from F. Shahdost-fard and M. Roushani, An impedimetric aptasensor based on water soluble cadmium telluride (CdTe) quantum dots (QDs) for detection of ibuprofen, *JEAC*, 2016, 763, 18–24. 43**

**Figure 4.1: UV-Vis spectrum of MSA-NiCl<sub>2</sub> (black line), NaHSe (red line) and MSA (blue line). .....68**

**Figure 4.2: UV-Vis spectrum of MSA-NiSe<sub>2</sub> QDs. The left inset shows the direct bandgap energy plot, while the right inset shows the indirect bandgap energy plot. ....68**

**Figure 4.3: FT-IR spectrum of MSA (A) and MSA-NiSe<sub>2</sub> QDs (B).....70**

**Figure 4.4: XRD pattern of MSA-NiSe<sub>2</sub> QDs .....72**

**Figure 4.5: PDDF (A) and Size distributions by number (B) of MSA-NiSe<sub>2</sub> QDs synthesized for 15 mins.....74**

**Figure 4.6: PDDF (A) and Size distribution by number (B) of the MSA-NiSe<sub>2</sub> QDs synthesized for 45 mins.....75**

**Figure 4.7: HR-TEM micrographs of MSA-NiSe<sub>2</sub> QDs taken at 50 nm (A), 20 nm (B), 10 nm (C) and 2 nm (D), respectively. ....77**

**Figure 4.8: HR-SEM micrographs of MSA-NiSe<sub>2</sub> QDs taken at 10µm (A), 1µm (B) and 200 nm (C), respectively, while EDS spectra of the MSA-NiSe QDs are shown in (D).....80**

**Figure 4.9: HR-SEM micrographs of Apt-MSA-NiSe<sub>2</sub> QDs at 10 µm (A), 1 µm (B) and 200 nm (C), respectively.....81**

<b>Figure 4.10: Cyclic voltammograms of conventional bare AuE and NaHSe precursor in 10 mM PBS, pH 7.4 at a scan rate of 10, 50 and 100 mV/s, respectively. ....</b>	<b>83</b>
<b>Figure 4.11: Cyclic voltammograms of conventional bare AuE and MSA-NiCl<sub>2</sub> precursor in 10 mM PBS, pH 7.4 at a scan rate of 10, 50 and 100 mV/s, respectively. ....</b>	<b>83</b>
<b>Figure 4.12: Cyclic voltammograms of conventional bare GCE and NaHSe precursor in 10 mM PBS, pH 7.4 at a scan rate of 10, 50 and 100 mV/s, respectively. ....</b>	<b>85</b>
<b>Figure 4.13: Cyclic voltammograms of conventional bare GCE and MSA-NiCl<sub>2</sub> precursor in 10 mM PBS, pH 7.4 at a scan rate of 10, 50 and 100 mV/s, respectively. ....</b>	<b>86</b>
<b>Figure 4.14: Cyclic voltammograms of MSA-NiSe<sub>2</sub> QDs in solution at a conventional AuE (A) and immobilized on a conventional AuE (B) in 10 mM PBS, pH 7.4, at multiple scan rates ranging from 10 to 100 mV/s.....</b>	<b>87</b>
<b>Figure 4.15: Cyclic voltammograms of MSA-NiSe<sub>2</sub> QDs in solution at a conventional GCE (A) and immobilized on a conventional GCE (B) in 10 mM PBS, pH 7.4, at multiple scan rates ranging from 10 to 100 mV/s.....</b>	<b>89</b>
<b>Figure 4.16: Cyclic voltammograms of MSA-NiSe<sub>2</sub> QDs in solution at a SPAuE (A) and immobilized on a SPAuE surface (B) in 10 mM PBS, pH 7.4, at multiple scan rates ranging from 10 to 100 mV/s. ....</b>	<b>90</b>
<b>Figure 4.17: Cyclic voltammograms of MSA-NiSe<sub>2</sub> QDs in solution at a SPCE (A) and immobilized on a SPCE surface (B) in 10 mM PBS, pH 7.4, at multiple scan rates ranging from 10 to 100 mV/s. ....</b>	<b>91</b>

<b>Figure 4.18: Shows the anodic plot (peak A1) of peak current (<math>I_{p,a}</math>) versus scan rate (<math>v</math>) (A) and plot of log peak current (<math>I_{p,a}</math>) versus log scan rate (<math>v</math>) (B). .....</b>	<b>94</b>
<b>Figure 4.19: Nyquist plots of bare SPCE and MSA-NiSe<sub>2</sub> QDs/SPCE, respectively, in 10 mM PBS, pH 7.4. ....</b>	<b>95</b>
<b>Figure 4.20: Bode plots of bare SPCE and MSA-NiSe<sub>2</sub> QDs/SPCE in 10 mM PBS, pH 7.4. ....</b>	<b>96</b>
<b>Figure 4.21: Overlapping CV curves of bare SPCE, bare SPCE-4-aminophenyl, bare SPCE-4-aminophenyl-QD, bare SPCE-4-aminophenyl-QDs-aptamer, bare SPCE-4-aminophenyl-QDs-Aptamer-blocking agent and bare SPCE-4-aminophenyl-QDs-aptamer-blocking agent-analyte in [Fe(CN)<sub>6</sub>]<sup>3-</sup>, in 10 mM PBS, pH 7.4 .....</b>	<b>97</b>
<b>Figure 4.22: Nyquist plots of bare SPCE, bare SPCE-4-aminophenyl, bare SPCE-4-aminophenyl-QD, bare SPCE-4-aminophenyl-QDs-aptamer, bare SPCE-4-aminophenyl-QDs-Aptamer-blocking agent and bare SPCE-4-aminophenyl-QDs-aptamer-blocking agent-analyte in [Fe(CN)<sub>6</sub>]<sup>3-</sup>, in 10 mM PBS, pH 7.4.....</b>	<b>98</b>
<b>Figure 4.23: DPV response of the aptasensor towards different concentrations of BNP in 5 mM [Fe(CN)<sub>6</sub>]<sup>3-</sup>, in 10 mM PBS, pH 7.4 .....</b>	<b>100</b>
<b>Figure 4.24: Calibration plots showing the relationship between the current and the BNP concentration. Each error bar corresponds to the average of no less than three independent replicates (n=3). ....</b>	<b>101</b>
<b>Figure 5.1: An Microfluidic system. Reprinted from L. Y. Shiroma, M. Santhiago, A. L. Gobbi and L. T. Kubota, Separation and electrochemical detection of paracetamol and 4-aminophenol in a paper-based microfluidic device, <i>Anal. Chim. Acta</i>, 2012, 725, 44–50.....</b>	<b>114</b>

**Figure 5.2: A magnetic microfluidic system. Reprinted from S. Lindsay, T. Vázquez, A. Egatz-Gómez, S. Loyprasert, A. A. Garcia and J. Wang, Discrete microfluidics with electrochemical detection, *Analyst*, 2007, 132, 412–416.....115**

**Figure 5.3: Representation of a wearable glucose sensor. Reprinted from J. Kim, A. S. Campbell and J. Wang, Talanta Wearable non-invasive epidermal glucose sensors : A review , *Talanta*, 2018, 177, 163–170.....116**

## LIST OF SCHEMES

<b>Scheme 2.1: Example of the formation of a SAM on a gold electrode metal substrate. Reprinted from M. Tanaka, T. Hayashi and S. Morita, The roles of water molecules at the biointerface of medical polymers, <i>Polym. J.</i>, 2013, 45, 701–710. ....</b>	<b>17</b>
<b>Scheme 2.2: BNP secretion in the heart. Reprinted from M. Weber and C. Hamm, Role of B-type natriuretic peptide (BNP) and NT-PROBNP in clinical routine, <i>Heart</i>, 2006, 92, 843–849.....</b>	<b>19</b>
<b>Scheme 2.3: Illustration of the working principle of immunoradiometric assays. Reprinted from W. L. Hutchinson, W. Koenig, M. Fröhlich, M. Sund, G. D. O. Lowe and M. B. Pepys, Immunoradiometric assay of circulating C-reactive protein: Age-related values in the adult general population, <i>Clin. Chem.</i>, 2000, 46, 934–938. ....</b>	<b>21</b>
<b>Scheme 2.4: Typical working principle of biosensors. Reprinted from D. Pizzoni, P. Pittia, M. Del Carlo, D. Compagnone and C. Di Natale, Oligopeptides-Based Gas Sensing for Food Quality Control, Sensors and Microsystems, Proceedings of the 17th National Conference, Brescia, Italy, 5-7 February 2013, <i>Springer Netherlands</i>, 2013, 268, 15–23. ....</b>	<b>23</b>
<b>Scheme 2.5: Working principle of an electrochemical aptasensor. Reprinted from J. Wang, Electrochemical biosensors: Towards point-of-care cancer diagnostics, <i>Biosens. Bioelectron.</i>, 2006, 21, 1887–1892. ....</b>	<b>25</b>
<b>Scheme 2.6: General Operating principle of FTIR. Reprinted from D. Ami, R. Posterl, P. Mereghetti, D. Porro, S. M. Doglia and P. Branduardi, Fourier</b>	

<b>transform infrared spectroscopy as a method to study lipid accumulation in oleaginous yeasts, <i>Biotechnol. Biofuels</i>, 2014, 7, 1–14. ....</b>	<b>29</b>
<b>Scheme 3.1: Brain natriuretic peptide (BNP) aptasensor fabrication. ....</b>	<b>64</b>

## LIST OF TABLES

<b>Table 2.1: A list of biomarkers associates with myocardial infarction. Reprinted from P. Garg, P. Morris, A. L. Fazlanie, S. Vijayan, B. Dancso, A. G. Dastidar, S. Plein, C. Mueller and P. Haaf, Cardiac biomarkers of acute coronary syndrome: from history to high-sensitivity cardiac troponin, <i>Intern. Emerg. Med.</i>, 2017, 12, 147–155. ....</b>	<b>18</b>
<b>Table 4.1: Electrochemical data of MSA-NiSe<sub>2</sub>-QDs acquired from cyclic voltammograms ran at different scan rates in the range 10 to 100 mV/s presented in Figure 4.17.....</b>	<b>92</b>
<b>Table 4.2: Charge transfer resistance (<math>R_{ct}</math>) values for the different modification steps in the sensor fabrication process.....</b>	<b>99</b>
<b>Table 4.3: Comparative study for the different detection methods of BNP.....</b>	<b>103</b>

## LIST OF EQUATIONS

$A = abc$	2.1		27
$n\lambda = 2d\sin\theta$	2.2		30
$R \leftrightarrow O + ne^-$	2.3		36
$O + ne^- \leftrightarrow R$	2.4		36
$i_p = (2.69 \times 10^5)n^{\frac{3}{2}}ACD^{\frac{1}{2}}V^{\frac{1}{2}}$	2.5		37
$\Delta E_p = E_{pa} - E_{pc} = 57mV/n$	2.6		38
$i_p = (2.99 \times 10^5)n(\alpha n_a)^{\frac{1}{2}}ACD^{\frac{1}{2}}V^{\frac{1}{2}}$	2.7		38
$E_t = E_0 \sin(\omega t)$	2.8		40
$\omega = 2\pi f$	2.9		40
$I_t = I_0 \sin(\omega t + \phi)$	2.10		41
$Z = E_t I_t = E_0 \sin(\omega t) I_0 \sin(\omega t + \phi) = Z_0 \sin(\omega t) \sin(\omega t + \phi)$	2.11		41
$z\omega = E_I = Z_0 (\cos\phi + \sin\phi)$	2.12		41
$NaBH_4 + Se + H_2O \rightarrow NaHSe + H_2$	3.1		57
$R_f =$			
Charge passed (Ah) Charge associated with Au $\mu Cm - 2 \times$			
Geometric area of electrode (cm <sup>2</sup> )			3.2
.....			60
$\alpha h\nu = A(h\nu - E_g)^n$	4.1		67
$\Delta E = h\nu = hc\lambda_{max}$	4.2		69

<b><math>D = K\lambda/\beta\cos\theta</math></b>	<b>4.3</b>	<b>72</b>
<b><math>2\text{Se} + 4 \text{NaBH}_4 \rightarrow 2\text{NaHSe} + \text{Na}_2\text{B}_4\text{O}_7 + 14 \text{H}_2</math></b>	<b>4.4</b>	<b>84</b>
<b><math>i_{pa} = n^2 F^2 A\Gamma/4RT</math></b>	<b>4.5</b>	<b>93</b>
<b>LOD = 3 × standard deviation of blank/Sensitivity</b>	<b>4.6</b>	<b>102</b>
<b>LOQ = 10 × standard deviation of blank/Sensitivity</b>	<b>4.7</b>	<b>102</b>

# 1 CHAPTER 1: Introduction

## Summary

*This chapter gives an overview of the problem statement, aims, approach and objectives. Included as well is a brief overview on the background of myocardial infarction, with focus on the biomarker known as brain natriuretic peptide and its existing detection methods. Other important factors such as nanomaterials and aptasensors are also discussed.*

## 1.1 Background

Myocardial infarction (MI) is the manifestation of a cardiovascular disease (CVD) and is the major cause of death in developed countries; it is becoming more prevalent in developing countries due to urbanization and changes to the western lifestyle.<sup>1</sup> The cause of MI is due to a blockage or an extremely slow blood flow of one of the hearts coronary arteries as depicted in figure 1.1 and another term to describe this process is known as acute coronary syndrome. The coronary artery supplies blood to a specific part of the hearts muscular wall, therefore a blocked artery leads to pain and malfunctions in the area of the heart it supplies.<sup>2</sup> The symptoms of MI can be classified as typical and atypical symptoms. Typical symptoms include pressure or tightness in the chest, shortness of breath, nausea and anxiety.<sup>3</sup> A typical symptom of MI are more prevalent in women and they include pain in the neck, jaw, shoulder or arms, breaking out in a cold sweat, dizziness and vomiting.<sup>4</sup> MI is associated with a 30% mortality rate and about 50% of the deaths occur prior to the arrival at the hospital. An additional 5-10% of survivors die within the first year after the MI attack, however, this all depends on the extent of the infarct.<sup>5</sup> Patients with a history of MI are likely to have a recurrent MI, and have an increased risk for complications and death, especially if the next MI attack occurs years after the first MI attack.<sup>6</sup>

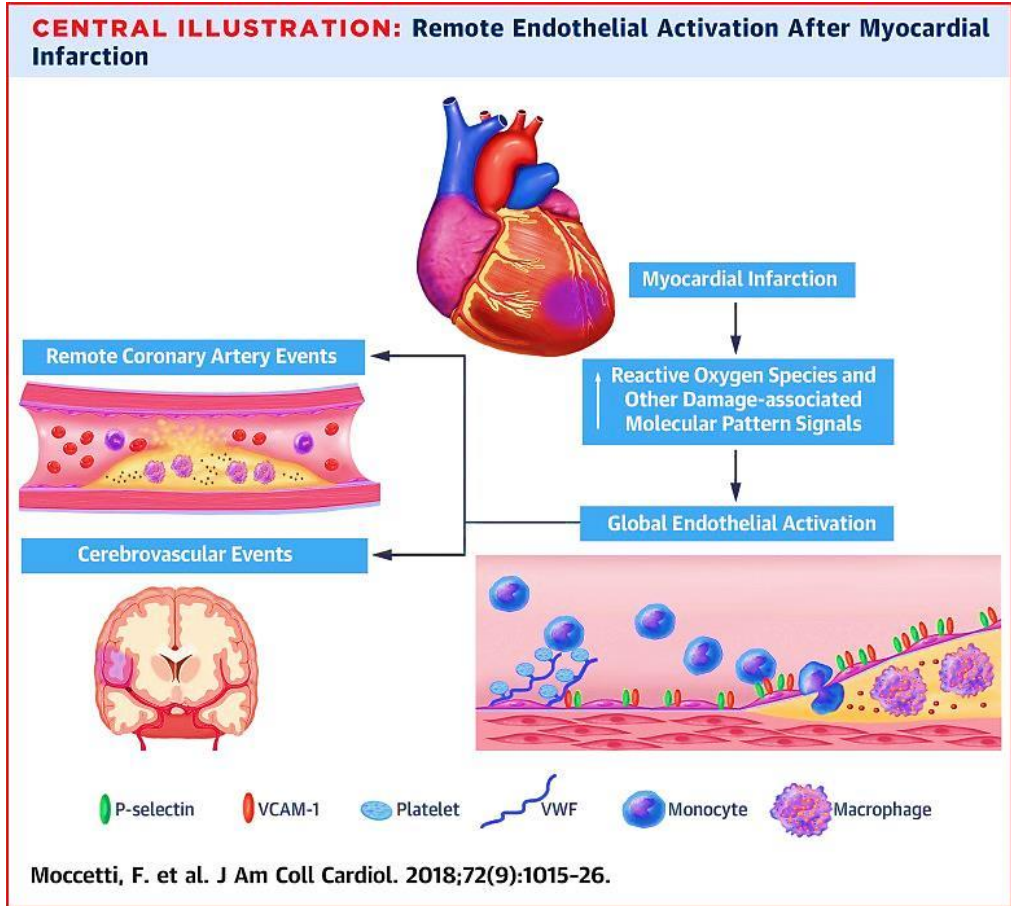


**Figure 1.1:** Myocardial infarction illustration adapted from F. Mocchetti and co-workers, Myocardial Infarction Produces Sustained Proinflammatory Endothelial Activation in Remote Arteries, *J. Am. Coll. Cardiol.*, 2018, 72, 1015–1026.

The most common diagnostic methods for MI are electrocardiograms (ECGs) and blood tests. An ECG provides information about the amount of damage done to the heart muscle as well as monitors the heart rate and rhythm. Blood tests measure the levels of cardiac enzymes (biomarkers for heart disease) which indicate whether the heart muscle is damaged.<sup>7</sup> Even though these are the most common methods for the diagnosis of MI, these methods are only effective once a patient has suffered a MI attack and as such are not considered a reliable method for early detection of MI. Therefore, to achieve early detection of MI, other ways and means need to be studied and explored, such as looking for reliable, specific and sensitive markers for cardiovascular diseases. Biomarkers are the best way to detect MI because a biomarker can be used to predict and monitor different diseases in patients ranging from cancer, tuberculosis and heart attacks.<sup>8</sup> Brain natriuretic peptide (BNP) is identified as one of the biomarkers for early diagnostics of

MI.<sup>9</sup> The release of BNP is due to myocardial wall stress which is due to volume and/or pressure overload.<sup>10</sup> Early detection of BNP has been extensively studied that is through first-generation assays which includes competitive radioimmunoassay, that requires the extraction and purification of plasma sample; second-generation assays, that is based on monoclonal antibodies; and third-generation assays, that are based on immunofluorescent methods.<sup>11</sup> One of the detection methods of BNP in recent years has been the use of immunoradiometric assays which falls under third –generation assays. However, there are short falls with this method such as cross reactivity, and finding primary antibodies that is not raised in the same species when performing multiple-labelling experiments. In addition, incubation of the antibody with the target can take up to several weeks and waiting on results can be time-consuming.<sup>12</sup> Electrochemical aptasensors are emerging as an alternative for detection of MI due to the fact that aptamers can be selected in vitro based on systematic evolution of ligands by exponential enrichment (SELEX), with high affinity and specificity and with no limitation to the target size.<sup>13</sup> Aptamers are considered advantageous over antibodies due to their high specificity, low generation cost, quick chemical synthesis and excellent batch unity.<sup>14</sup> Applying aptamers in electrochemical sensors has its advantages such as the fact that aptamers can be easily modified which allows it to be immobilized over a wide range of transducer surfaces. The conformational change of aptamers upon target analyte binding makes it a suitable candidate to design-label free and portable devices for applications in analytical chemistry. The conformational characteristics of aptamers enhances the detection phenomena of small size target analyte by enfolding them in the folded DNA structures.<sup>15</sup> Nanomaterials such as quantum dots (QDs), carbon nanotubes, graphene or polymeric nanoparticles has been incorporated in aptasensors for increase performances due to the unique properties of these materials at the nanoscale compared to their bulk counterparts.<sup>16</sup> QDs are particularly interesting because they show size-dependent properties that gives rise to a unique phenomenon known as quantum confinement. Quantum confinement is the changes in the electronic and optical properties of a material that is extremely small usually 10 nm or less.<sup>17</sup> QDs are semiconductor nanomaterials that ranges from 1-10 nm in size.<sup>18</sup> The optical properties of QDs depends on their size, shape and their synthesis method which can be easily tuned to match the specific requirements of any application.<sup>19</sup> For example QDs can be applied in electrochemical aptasensors where biomolecules adsorbed or immobilized on the QDs surface cause changes in the optical

properties of QDs and these optical properties are exploited to develop highly sensitive bioanalytical tools. In addition the high conductivity, easy bio- functionalization and large surface area are the basis of QDs applications in these sensors and thus they can be used for detection of MI biomarkers.<sup>20</sup> Research studies have been published on electrochemical aptasensors using nanoparticles for the detection of cardiac biomarkers for example Jo and co-workers reported a sensitive electrochemical aptasensor using ferrocene modified nanoparticles for the detection of cardiac troponin I (cTnI), a biomarker for myocardial infarction.<sup>21</sup> The aptamers were selected via the SELEX method and had a high sensitivity and selectivity toward cTnI. The binding affinity of the aptamer was investigated based on their dissociation constants by surface plasma resonance. The electrochemical aptasensor was then designed based on square-wave voltammetry using ferrocene-modified silica nanoparticles. The developed aptasensor showed an excellent analytical performance for cTnI with a wide linear range of 1-10000 pM and a detection limit of 1 pM which was lower than the cut-off values of 70-400 pg/mL.

## **1.2 Problem statement, research aims, approach and objectives**

According to the World Health Organization (WHO) it was estimated that in 2004, 17.1 million people around the world died from cardiovascular disease (CVD) and the number is expected to grow to 23.4 million in 2030.<sup>22</sup> This is a problem for the world population, especially for people living in South Africa. In South Africa alone CVD is responsible for 1 in 6 deaths (17.3%), therefore even though there is extensive research in the detection of MI; the survival rate of people affected with heart attacks are still low.<sup>23</sup> Contributing factors to the survival rate is the fact that South Africa is a developing country and there is a lack of access and effective treatment methods in disadvantage communities. The lack of knowledge of new treatment methods, and lastly traditional diagnostic methods that are not effective when it comes to early detection of MI.<sup>24</sup> The traditional diagnostic methods for MI are electrocardiograms, blood tests, chest X-ray, coronary catheterization and cardiac computerized tomography (CT) or magnetic resonance imaging (MRI).<sup>25</sup> These methods are limited, time-consuming and expensive and can indicate false positive results. Some of these techniques are invasive and causes unpleasant visits to the doctor's office.<sup>26</sup> Therefore

early detection of MI is important for effective treatment and patient survival. Biological markers have become quite essential when it comes to detecting heart diseases, however, some of the available MI biomarkers have low specificity and sensitivity which make them unreliable for early MI detection.<sup>27</sup> BNP is considered an ideal biomarker for the diagnosis of MI because it has a sensitivity of 95% and a specificity of 76% when compared to other available cardiac biomarkers.<sup>28</sup>

For this reason, the proposed research study aimed to develop a sensitive, fast and cost-effective quantum dot based aptasensor for the detection of BNP, a biomarker for MI. The prospective outcome of this research study was to design and construct a device that can give results in real-time thus eliminating long waiting periods at the doctor's office. The device should be able to detect very low amounts of BNP and it should be easy to operate. The device should be portable such that it can be distributed in rural areas where there is no access to proper health facilities and effective treatment methods.

In this study the research aim was achieved through the following objectives:

- I. Syntheses of novel mercaptosuccinic acid-nickel selenide quantum dots (MSA-NiSe<sub>2</sub> QDs).
- II. Spectroscopic analysis of QDs using fourier transform infrared (FTIR) and ultraviolet-visible (UV) spectroscopy.
- III. Microscopic analysis of QDs using high resolution transmission electron microscopy (HR-TEM) and high resolution scanning electron microscopy (HR-SEM).
- IV. Electrochemical analysis of various electrode platforms using cyclic voltammetry and impedance spectroscopy.
- V. Modification of the electrode platforms with various materials, these include QDs, aptamer and analyte; and characterization of these different surface modified surfaces using electrochemical methods.
- VI. Detection of analyte using differential pulse voltammetry (DPV).

### **1.3 Conclusion**

Myocardial infarction (MI) affects many people across the world; however, in South Africa alone the death statistic of MI is quite large. Traditional diagnostic methods for the detection of MI are not effective in obtaining results fast and in real time at the doctor's office. One approach to address this issue is to make use of electrochemical sensors which are emerging as alternatives for traditional diagnostic methods. Biomarkers such as brain natriuretic peptide are becoming popular as early diagnostic protocols for cardiovascular diseases. Electrochemical aptasensors which is a class of biosensors can be used to detect cardiovascular diseases rapidly with the incorporation of nanomaterials which improves its sensitivity and specificity for the detection of the disease. Therefore creating a sensor that is fast, sensitive and specific will address issues that people in South Africa as well as people around the world faces when it comes to early detection of cardiovascular diseases and the medical sector as a whole.

## References

- 1 G. Anand Kumar, Biomarkers in Acute Myocardial Infarction, *Natl. J. Basic Med. Sci.*, 2018, **8**, 137–141.
- 2 C. K. Meier and M. A. Oyama, Chapter 41 MYOCARDIAL INFARCTION, 2004, **12** 174–176.
- 3 K. Fox, S. Street, C. Daly and S. Street, Prognostic role of combination of coronary flow reserve with aortic distensibility indices Downloaded from <http://eurheartj.oxfordjournals.org/> by guest on November 14 , 2015 References typical presentation and unrecognized myocardial infarction, 2003, 21000.
- 4 General Cardiology 2, *Eur. Hear. J. Suppl.*, 2010, **12**, S15–S16.
- 5 M. Saleh and J. A. Ambrose, Understanding myocardial infarction [ version 1 ; referees : 2 approved ] Referee Status :, 2018, **7**, 1–8.
- 6 R. Carlisle, standing give, *British medical journal.*, 1979, **6**, 1583-1584.
- 7 S. Greer, L. J. Schieb, M. Ritchey, M. George and M. Casper, County health factors associated with avoidable deaths from cardiovascular disease in the United States, 2006-2010, *Public Health Rep.*, 2016, **131**, 438–448.
- 8 P. C. Guest, Biomarkers and mental illness: It's not all in the mind, *Biomarkers Ment. Illn. It's Not All Mind*, 2016, 1–203.
- 9 S. Fu, P. Ping, Q. Zhu, P. Ye, L. Luo and G. G. Schiattarella, Brain Natriuretic Peptide and Its Biochemical , Analytical , and Clinical Issues in Heart Failure : A Narrative Review, 2018, **9**, 1–8.
- 10 J. Krupicka, T. Janota and J. Hradec, Natriuretic peptides in heart failure, *Cor Vasa*,

- 2013, **55**, 370–376.
- 11 B. Peptides, A. G. Semenov and E. E. Feygina, *Standardization of BNP and NT-proBNP Immunoassays in Light of the Diverse and Complex Nature of Circulating*, Elsevier Inc., 1st edn., 2018.
  - 12 M. Jones and R. J. Thompson, A two-site immunoradiometric assay for the MB isoenzyme of creatine kinase.
  - 13 X. Fang and W. Tan, Aptamers Generated from Cell-SELEX for Molecular Medicine : A Chemical Biology.
  - 14 K. Sefah, D. Shangguan, X. Xiong, M. B. O. Donoghue and W. Tan, Development of DNA aptamers using Cell-SELEX, *Nat. Protoc.*, 2010, **5**, 1169–1185.
  - 15 A. Hayat and J. L. Marty, Aptamer based electrochemical sensors for emerging environmental pollutants, 2014, **2**, 1–9.
  - 16 A. Rhouati, J. Marty and A. Vasilescu, *Metal Nanomaterial-Assisted Aptasensors for Emerging Pollutants Detection*, Elsevier Inc., 2018.
  - 17 M. Jha, *Current Trends in Industrial Scale Synthesis of Quantum Dots and Its Application in Electronics*, Elsevier Inc., 2018.
  - 18 B. Veigas, L. Giestas, C. Almeida, P. V Baptista, N. De Lisboa, C. De Caparica, M. Esquillor, U. N. De Lisboa, C. De Caparica, U. Nova, D. Lisboa and C. De Caparica, Noble Metal Nanoparticles for Biosensing Applications, 2012, 1657–1687.
  - 19 V. A. Online, S. Pang, T. P. Labuza and L. He, Development of a single aptamer-based surface enhanced Raman scattering method for rapid detection of multiple pesticides , 2014, 1895–1901.

- 20 J. E. Smith, C. D. Medley, Z. Tang, D. Shangguan, C. Lofton and W. Tan, Aptamer-Conjugated Nanoparticles for the Collection and Detection of Multiple Cancer Cells, 2007, **79**, 3075–3082.
- 21 H. Jo, H. Gu, W. Jeon, H. Youn, J. Her, S. Kim, J. Lee, J. H. Shin and C. Ban, Electrochemical Aptasensor of Cardiac Troponin I for the Early Diagnosis of Acute Myocardial Infarction, DOI:10.1021/acs.analchem.5b02312.
- 22 B. Jena and A. Kadithi, Study of risk factors affecting the survival rate of emergency victims with ‘chest pain’ as chief complaint, *Indian J. Community Med.*, 2009, **34**, 293.
- 23 A. R. P. Walker and P. Sareli, Coronary heart disease: Outlook for Africa, *J. R. Soc. Med.*, 1997, **90**, 23–27.
- 24 V. Salomaa, H. Koukkunen, M. Ketonen, P. Immonen-Räihä, P. Kärjä-Koskenkari, J. Mustonen, S. Lehto, J. Torppa, A. Lehtonen, J. Tuomilehto, Y. A. Kesäniemi and K. Pyörälä, A new definition for myocardial infarction: What difference does it make?, *Eur. Heart J.*, 2005, **26**, 1719–1725.
- 25 J. E. Udelson and L. W. Stevenson, The future of heart failure diagnosis, therapy, and management, *Circulation*, 2016, **133**, 2671–2686.
- 26 I. Daghlas, H. S. Dashti, J. Lane, K. G. Aragam, M. K. Rutter and R. Saxena, Sleep Duration and Myocardial Infarction, , DOI:10.1016/j.jacc.2019.07.022.
- 27 D. Chan and L. L. Ng, Biomarkers in acute myocardial infarction Review, *National Journal of Basic Medical Sciences*, 2018, **8**, 137-141.
- 28 M. R. Cowie, P. Jourdain, A. Maisel, U. Dahlstrom, F. Follath, R. Isnard, A. Luchner, T. McDonagh, J. Mair, M. Nieminen and G. Francis, Clinical applications of B-type natriuretic peptide (BNP) testing, *Eur. Heart J.*, 2003, **24**, 1710–1718.

## **2 CHAPTER 2: Literature Review**

### **Summary**

*This chapter discusses the background of QDs as well as their role as supporting materials in electrochemical biosensors, especially aptasensors. Furthermore, this chapter outlines the importance of aptasensors as detection systems for cardiovascular diseases with special focus directed towards biological markers which acts as target analyte during disease diagnosis.*

### **2.1 Quantum dots**

Nanomaterials are an important feature of nanoscience and nanotechnology. Over the past few years research and development of nanomaterials have grown exponentially and is expected to rise in the near future.<sup>1</sup> Nanomaterials is defined as a set of substances where at least one dimension is less than a 100 nm and at this scale unique optical, magnetic, electric and other properties emerge.<sup>2</sup> Due to these unique properties nanomaterials shows a great potential in electronics, medicine and other fields.<sup>3</sup> Nanomaterials can be zero dimension (e.g. quantum dots), one dimension (e.g. surface films), two dimensions (e.g. strands or fibers) and three dimensions (e.g. graphite) as depicted in figure 2.1.<sup>4</sup> Nanomaterials can exist in different forms such as single, fused, aggregated or agglomerated forms with spherical, tubular and irregular shapes.<sup>5</sup> Common types of nanomaterials include nanorods, nanotubes, quantum dots and fullerenes.

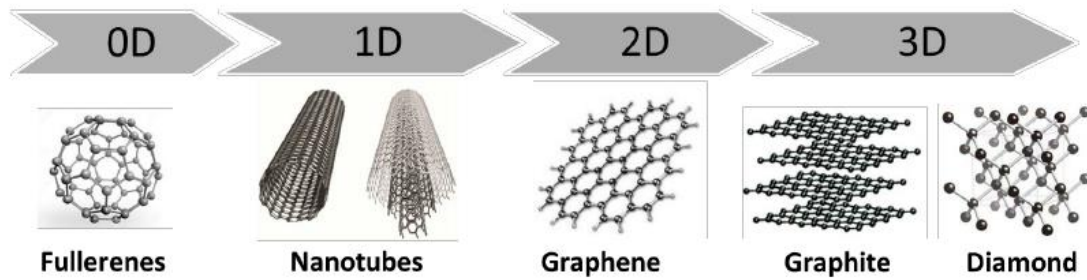


**Figure 2.1:** Illustration of the different types of nanomaterials. Reprinted from S. Wu, L. Cheng and Q. Wang, Excitonic effects and related properties in semiconductor nanostructures: Roles of size and dimensionality, *Mater. Res. Express*, 2017,4,1-12.

Quantum dots (QDs) are semiconductor nanoparticles made up of elements from group II-VI or group II-V on the periodic table and are classified as inorganic colloids with physical dimensions of 1 to 20 nm, smaller than the bulk excitation Bohr radius.<sup>6</sup> The bulk excitation Bohr radius is the distance between the electron-hole pair.<sup>7</sup> The Bohr radius is significant to QDs because it is used as a reference point to describe the degree of confinement of the QDs.<sup>8</sup> The degree of confinement in QDs is due to a unique phenomenon known as the quantum confinement.<sup>9</sup> The quantum confinement phenomenon is observed when the size of the particle is too small to be comparable to the wavelength of an electron.<sup>10</sup> Therefore as the size of the QDs decrease, the degree of confinement increases which results in the production of an exciton (which is a excited electron and its associated hole) of higher energy leading to an increase in the bandgap energy. While an increase in the size of the QDs results in a decrease in the degree of confinement and thus, produce an exciton of lower energy leading to a decrease in the bandgap energy as depicted in figure 2.2.<sup>11</sup> By manipulating the QD size, larger particles will emit light toward the infra-red region (red shift) while smaller particles will emit toward the ultraviolet region (blue shift).

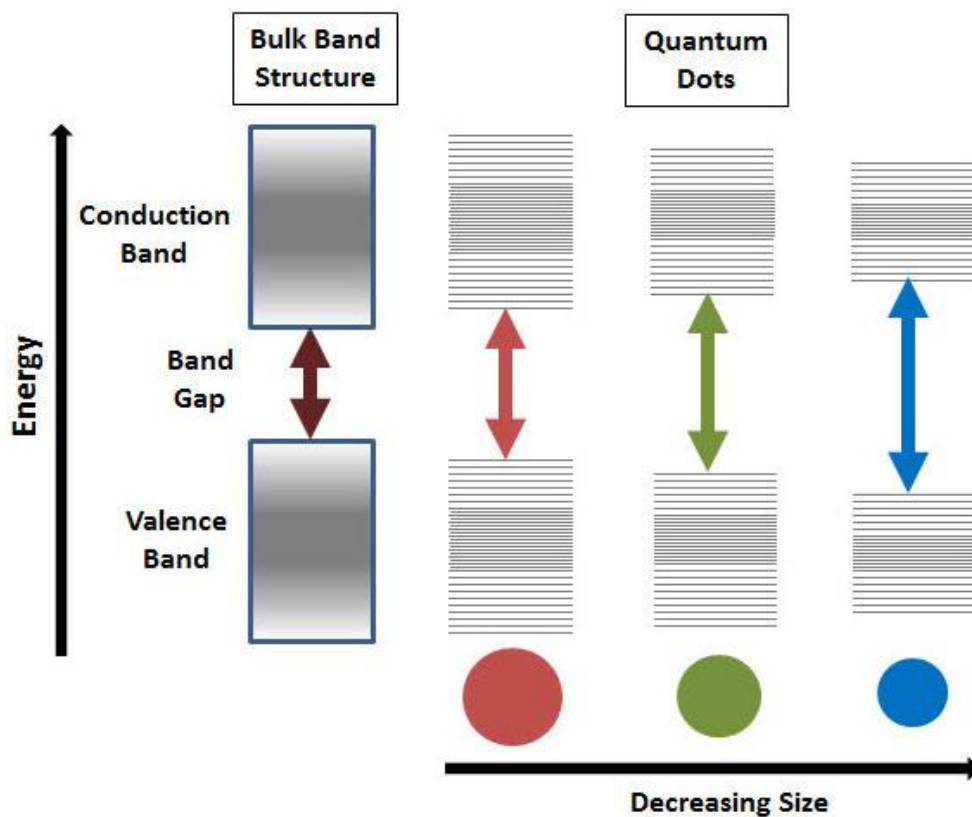


**Figure 2.2:** Quantum confinement of QDs based on shape and size dependences. Reprinted from J. McKittrick and L. E. Shea-Rohwer, Review: Down conversion materials for solid-state lighting, *J. Am. Ceram. Soc.*, 2014, 97, 1327–1352.

QDs are commonly produced via two synthesis routes that is, organic and aqueous synthesis routes. Following the organic synthesis route QDs are produced by common ligands such as trioctylphosphine oxide (TOPO) and trioctylphosphine. These ligands allows the QDs to be soluble in organic solvents.<sup>12</sup> The aqueous synthesis route use water as the solvent and results in water soluble QDs, and for this reason, can be used in biological applications.<sup>13</sup> The aqueous synthesis method has advantages over the organic approach due to the fact that it is inexpensive, simple and has a higher degree of reproducibility compared to the organic synthesis route. The most conventional method for the production of water soluble QDs are via the reflux condensation method. During the reflux condensation method the sample is heated for a specific amount of time, producing a vapor that is continuously cooled back into liquid form by a condenser that has a continuous flow of water coming in, and water going out.<sup>14</sup> The disadvantages of heating under reflux is that it is time consuming, fluctuation in heating distribution, and low product yields.<sup>15</sup> For this reason researchers have investigated other forms of

synthesis methods like microwave assisted synthesis. Microwave irradiation is being implemented as a new method for producing QDs with a high quantum yield and high degree of monodispersity.<sup>16</sup> Other advantages of microwaves assisted heating includes high heating rates, leading to an increase in reaction rates, it is reproducible with improved selectivity due to reduced side reactions and it allows for a high throughput synthesis.<sup>17</sup> There are a number of researches who adopted this synthesis method for the production of QDs for example, Atkins and co-workers synthesized silicon QDs via microwave assisted heating in an aqueous solution and it resulted in photoluminescent QDs obtained in just 12 min with a high quantum yield of 23%.<sup>18</sup> While Rebeiro and co-workers used microwave assisted heating to produce highly luminescent thiol capped cadmium telluride (CdTe) QDs with a quantum yield of 60% within a reaction time of 2 to 90 min.<sup>19</sup> The present research study employed microwave assisted heating method to produce water soluble QDs for application in electrochemical biosensors.

### **2.1.1 Capping Agents**

Capping agents which are molecules such as surfactants, dendrimers and polymers are key parameters when preparing nanomaterials. The capping agent can be thought of as a primary stabilizing agent providing colloidal stability to QDs.<sup>20</sup> Primary amines, carboxylic acids, thiols and long chained organo-phosphorates are common capping agents employed in QDs synthesis.<sup>21</sup> The capping agents control the rate of growth, particle morphology, reaction pathway and the particle size distribution.<sup>22</sup> An example of a QD/capping agent system is the CdTe QDs/thiol capping system and the role of the capping agent in this system is to inhibit hole trapping, and thus results in extremely luminescent CdTe QDs without the need for further inorganic shells or prolonged processing.<sup>23</sup> Hole trapping or surface traps occurs when localized electronic states or highly reactive sites on the QDs surface are prone to chemical and redox processes.<sup>24</sup> This provides a pathway for non-radiative recombination of electrons. Nonradiative recombination of electrons is a process where an excited electron in the conduction band does not return to its original hole in the valence band and as a result does not emit light, which in turn, has an effect on the photoluminescent properties of the QDs.<sup>25</sup> Therefore capping agents especially the thiol capping agents are important because it prevents surface traps.

Accurate determination of the amount of capping agent for any synthesis route is important, so that the capping agent to QDs bond is strong and not weak. Weakly bound capping agents attached to QDs cause agglomeration, change in morphology and it causes the QDs to be unstable in solution, thus, ultimately causing the QDs to precipitate out of solution.<sup>26</sup> Some examples of capping agents can be seen in Figure 2.3 below.

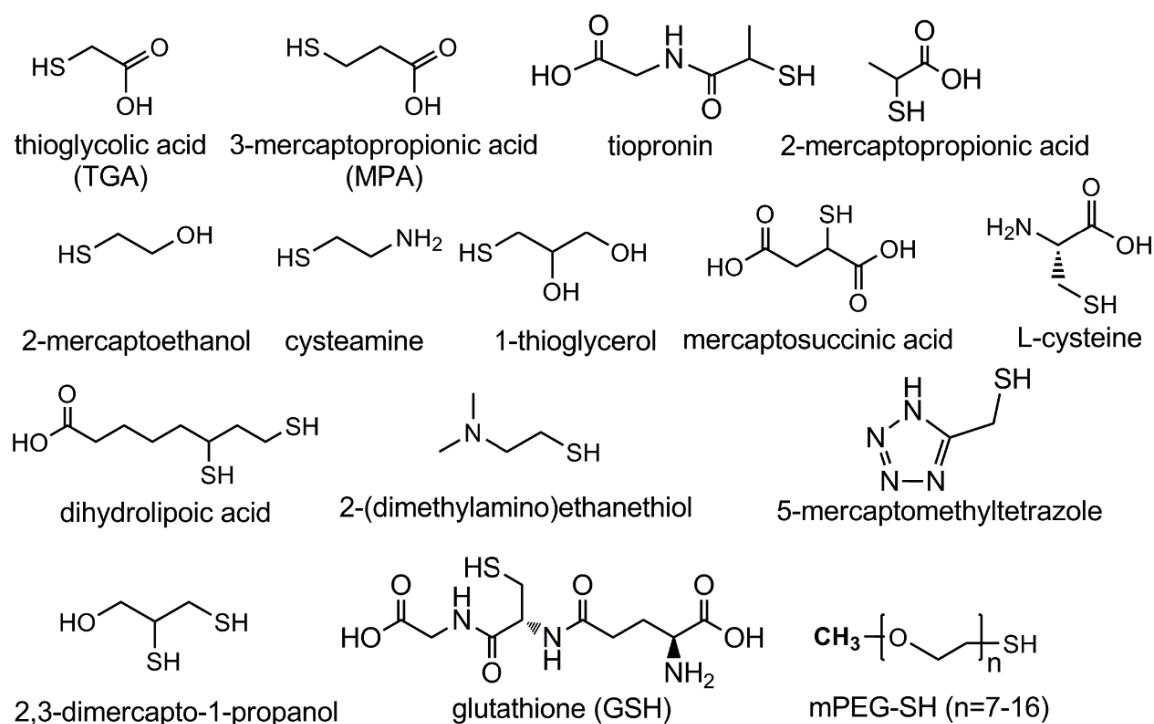


**Figure 2.3:** Examples of capping agents. Reprinted from C. M. Phan and H. M. Nguyen, Role of Capping Agent in Wet Synthesis of Nanoparticles, *J. Phys. Chem. A*, 2017, 121, 3213–3219.

Another use of capping agents is to make QDs water soluble for application in biological studies. QDs are hydrophobic by nature and as such requires bio-functional capping agents in order to be redispersed in water.<sup>27</sup> These bio-functional molecules help in bioconjugation with peptides, carbohydrates, DNA fragments, virus and natural products through hydrophobic interactions or electrostatic and covalent coupling.<sup>28</sup> Thiol capping agents such as, mercaptosuccinic acid is an example of a bio-functional capping agent and more information about this molecule is outlined in the section below.

### 2.1.1.1 Mercaptosuccinic Acid

Mercaptosuccinic acid (MSA) is an important chiral multifunctional intermediate in organic synthesis and has been widely employed in the synthesis of various biologically active sulphurs, such as antimicrobial and antitubercular. Recently it has also been used as a building block in the synthesis of potential novel polyanionic inhibitors for HIV and AIDS.<sup>29</sup> In comparison to other thiols such as, 3-mercaptopropanoic acid (MPA), the structure of MSA combines different properties. MSA can stabilize QDs at acidic as well as alkaline pH whereas capping agents such as MPA can only stabilize QDs at an alkaline pH which limits their applications.<sup>30</sup>

MSA capped QDs is widely used for nanotechnology applications such as biological labelling when detected by fluorescence.<sup>31</sup> The presence of MSA increases the QDs sensitivity as well as improves the stability against photobleaching and makes the QDs more chemically stable when compared to other fluorophores. Ying and co-workers synthesized highly luminescent MSA coated Cadmium telluride (CdTe) nanocrystals for bio-imaging applications. The QDs was synthesized via a one-pot aqueous method and refluxed under open-air conditions for 30 min. By selecting MSA as a capping agent it resulted in highly luminescent QDs with a quantum yield of 70% at an optimal pH range of 6-9.<sup>32</sup> In this research study MSA was used as a capping agent for novel water soluble NiSe<sub>2</sub> quantum dots

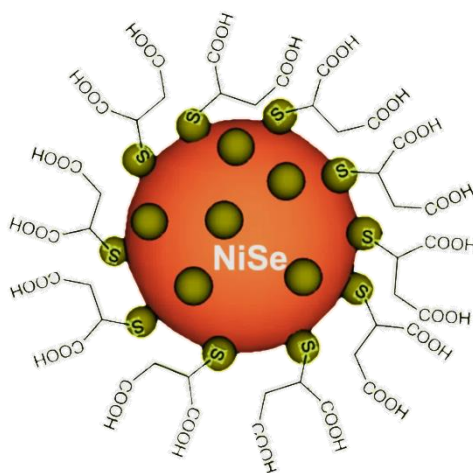
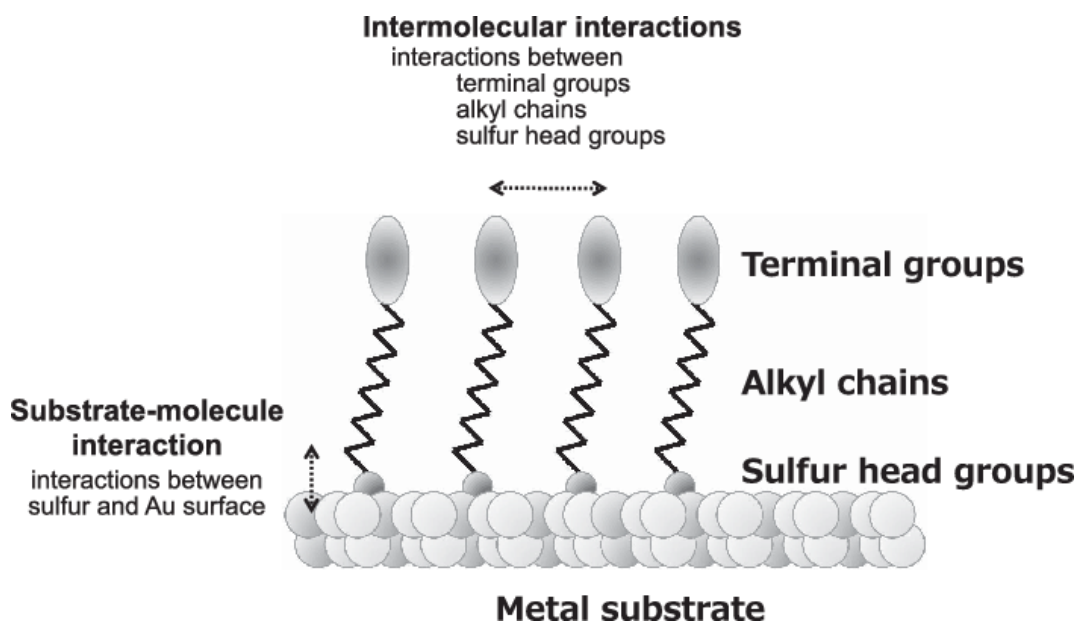


**Figure 2.4:** Representation of MSA-Capped NiSe<sub>2</sub> QDs

## 2.2 Self-assembled monolayer

The formation of self-assembled monolayers (SAMS) is an effective method to generate an appropriate surface structure for binding QDs to the surface of any substrate of interest.<sup>33</sup> For example on a gold substrate a suitable choice of monolayer formation is using alkanethiols. The sulphur atom of alkanethiols binds to the surface of the gold atoms and results in amino-terminated Au surfaces. The amino groups on the modified Au surface can bind with the carboxyl groups on the QDs by forming amide bonds.<sup>34</sup>

In order to link QDs to Au surfaces via the self-assembled monolayer is through the use of a cross-linking agent known as 1-ethyl-3-(3-dimethylaminopropyl) carbodiimide (EDC) and n-hydroxysuccinimide (NHS). EDC is used to couple carboxyl groups to primary amines in the presence of NHS which is often included in EDC coupling to improve efficiency or create dry-stable (amine reactive) intermediates.<sup>35</sup> Patel and co-workers used homogenous and mixed carboxylate-terminated self-assembled monolayers to immobilize protein molecules. For protein immobilization the carboxylic terminated SAMS were immersed in a 1:5 ratio of EDC /NHS for 30 min. The resultant NHS ester monolayers reacted for 30 min in a protein solution consisting of catalase in sodium phosphate buffer. Deprotonating the lysine residues on the catalase surface by adjusting the pH above 8 allowed a reaction to take place with the NHS ester. After the removal of the SAM from the protein solution the surface was rinsed with deionized water, dried under argon gas and used.<sup>36</sup> Another method of forming a monolayer is through an electrographing method. In an electrographing procedure the organic layer is formed on a conductive substrate surface such as carbon electrodes electrochemically whereas on gold electrodes it occurs spontaneously through the thiol-gold interaction thus SAMS are commonly associated with AuE.<sup>37</sup> In this research study a SAM was formed on conventional gold electrodes (AuE) and screen printed gold electrodes (AuE) using cysteamine and on conventional glassy carbon electrodes (GCE) and screen printed carbon electrodes (SPCE) the monolayer was formed through an electrographing procedure by the electrochemical reduction of 4-nitrophenyl to 4-aminophenyl.



**Scheme 2.1:** Example of the formation of a SAM on a gold electrode metal substrate. Reprinted from M. Tanaka, T. Hayashi and S. Morita, The roles of water molecules at the biointerface of medical polymers, *Polym. J.*, 2013, 45, 701–710.

## 2.3 Biomarkers

Biomarkers are biological molecules found in blood, tissues or other bodily fluids that are indicators of normal or abnormal processes within the body.<sup>38</sup> Typically biomarkers can differentiate between an affected patient with the disease like myocardial infarction and a patient without heart disease. There are currently a variety of biomarkers such as proteins (enzyme or receptor), nucleic acids (DNA and RNA), antibodies and peptides.<sup>38</sup> The World Health Organization (WHO) states that the true definition of biomarkers includes almost any measurement reflecting an interaction between a biological system and a potential hazard which may be physical, chemical or biological.<sup>39</sup> Over the last 50 years cardiac biomarkers has evolved as essential tools in cardiology for primary and secondary prevention, the diagnosis and management of myocardial infarction.<sup>40</sup>

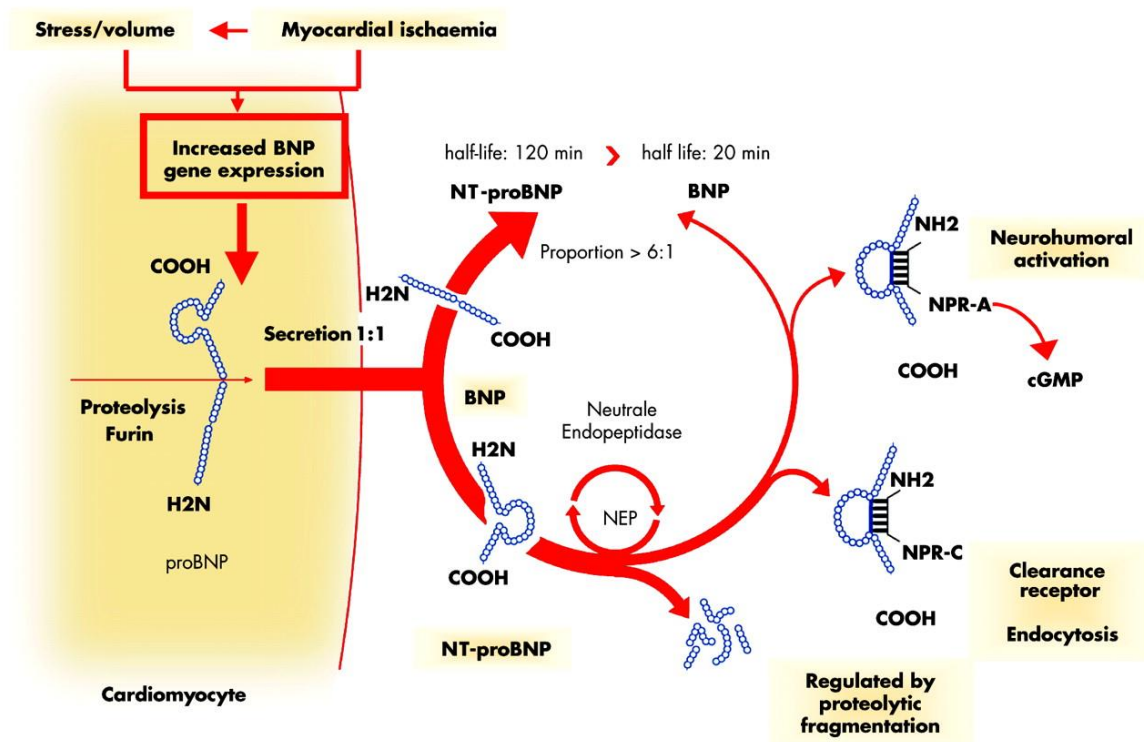
**Table 2.1:** A list of Biomarkers associates with myocardial infarction. Reprinted from P. Garg, P. Morris, A. L. Fazlanie, S. Vijayan, B. Dancso, A. G. Dastidar, S. Plein, C. Mueller and P. Haaf, Cardiac biomarkers of acute coronary syndrome: from history to high-sensitivity cardiac troponin, *Intern. Emerg. Med.*, 2017, 12, 147–155.

Biomarker	Year of first appearance in literature
H-FABP	1988
AST	1954
LDH	1948
CK	1954
HBDH	1963
CK-MB	1962
CK-MB mass	1986
Myoglobin	1941
TnT	1940
TnI	1987
miRNA	2009
PAMP	2002

The sensitivity and specificity of an ideal biomarker needs to be 100%, but there are currently no cardiac biomarkers that can achieve such a good combined sensitivity and specificity.<sup>41</sup> For example cardiac biomarkers such as creatinine kinase isoenzyme (CK-MB) has a sensitivity of 62.5% and a specificity of 95.7% while glycogen phosphorylase isoenzyme (GP-BB) has a sensitivity of 96% and specificity of 43,7%.<sup>42</sup> The need for cardiac biomarkers with an ideal sensitivity and specificity is important to avoid unnecessary biopsies and false positive predictive values.<sup>43</sup> Today troponin and natriuretic peptides remains essential biomarkers for myocardial infarction due to the information that can be obtained from the results of these biomarkers. For this reason, the present research study focused on one of the natriuretic peptides namely brain natriuretic peptide. The following section gives a brief overview of this promising cardiac biomarker.

### 2.3.1 Brain natriuretic peptide (BNP)

Brain natriuretic peptide (BNP) is a hormone that is secreted by the ventricles in the heart as response to the left ventricular stretching or wall stress.<sup>44</sup> BNP belongs to the natriuretic peptide family along with other similar structures such as arterial natriuretic peptide (ANP), C-type natriuretic peptide (CNP) and urodilatin. BNP is synthesized in the heart as a pre-hormone consisting of 108 amino acids. When released into circulation it is split into two equal proportions consisting of the biologically active 32 amino acid BNP which represents the C fragment, and the biologically inactive 76 amino acid which represents the N-terminal fragment (NT-proBNP).<sup>45</sup> Both molecules are constantly released in the heart and can be detected in the blood. During circulation BNP brings out a variety of effects by interacting with the natriuretic peptide receptor type A (NPR-A). These effects are biological and physiological in nature such as cGMP production and, natriuresis/diuresis and peripheral vasodilation respectively.<sup>46</sup>



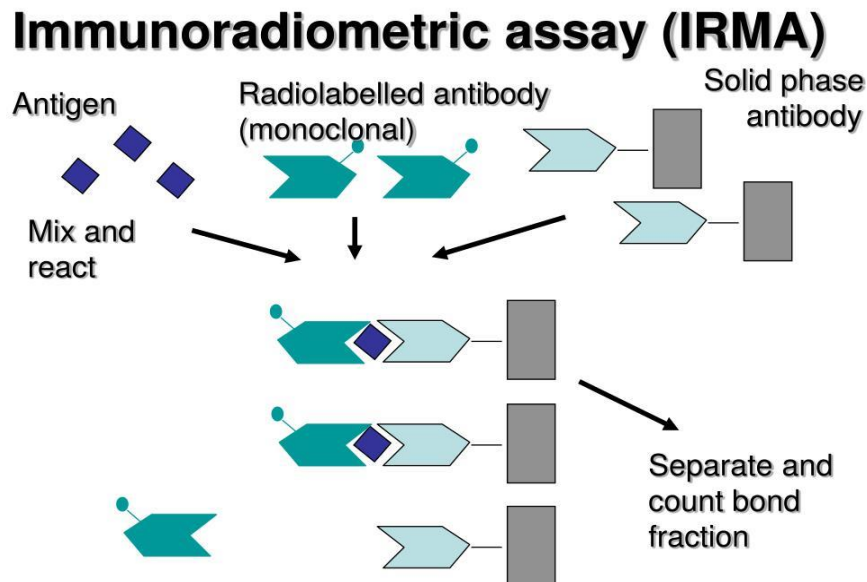
**Scheme 2.2:** BNP secretion in the heart. Reprinted from M. Weber and C. Hamm, Role of B-type natriuretic peptide (BNP) and NT-PROBNP in clinical routine, *Heart*, 2006, 92, 843–849.

BNP has a half-life of 20 min and is cleared from the plasma of blood by binding to the natriuretic peptide receptor type C (NRP-C) and through proteolysis by neutral endopeptidase; whereas NT-proBNP has a half-life of 120 min and is cleared from the plasma of blood by renal excretion.<sup>47</sup> Many medications (e.g. spironolactone, angiotensin-II receptor blockers, aldactone) to treat a heart disease such as myocardial infarction (MI) reduce natriuretic peptide concentrations. Therefore many patients with MI will have BNP levels in the normal diagnostic range, that is BNP levels less than a 100 pg/mL.<sup>48</sup> There is no first line test for MI due to the fact that MI is usually diagnosed in patients with known heart disease that present nonspecific symptoms such as breathlessness, ankle swelling etc.<sup>49</sup> To confirm clinically suspected MI physicians rely on electrocardiograms and left ventricular ejection fraction, but there are still a large number of patients that have diastolic heart failure which is when the left ventricle becomes stiffer than normal and the heart cannot relax the way it should.<sup>50</sup> The best way to diagnose and treat these patients is still unclear, but since BNP increases due to wall stress of the heart muscle it is considered an effective method for detecting MI with or without systolic dysfunction; in addition what makes BNP more desirable biomarker than NT-proBNP is its defined cut-off of 100 pg/ml which makes it easier to make a judgment compared to NT-proBNP, whose cut-off is susceptible to a patient's age. An Early detection method for BNP relies on immunoradiometric assays.

### **2.3.1.1 Immunoradiometric assay**

In immunoradiometric assays the MI biomarker is assayed directly by combination with the specific labeled antibody. In the assay development process the samples of antigen reacts with excess of labeled antibody followed by an immunoabsorbent consisting of an antigen coupled to a solid phase; which is then added to bind to the unreacted antibody and then removed by centrifugation.<sup>51</sup> The signal obtained from the radioactive material in the supernatant is a function of the concentration of the antigen. The technique was introduced by Miles and Hales who proposed theoretical advantages that would improve the sensitivity and specificity of immunoassays.<sup>52</sup> Since then, the practical advantages of the immunoradiometric assays have been exploited for particular antigens where standard techniques were proven difficult to use as detection methods for certain diseases. The main advantages of immunoradiometric assays are the use of labeled antibodies. Labeled antibodies appear to be stable for several days when

incubated with high concentrations of plasma. This is because the assay properties of labeled antibodies undergo little deterioration over long periods of time and it avoids the problems concerning the iodination of peptide molecules. Below is a scheme illustrating the working principles of immunoradiometric assays.



**Scheme 2.3:** Illustration of the working principle of immunoradiometric assays. Reprinted from W. L. Hutchinson, W. Koenig, M. Fröhlich, M. Sund, G. D. O. Lowe and M. B. Pepys, Immunoradiometric assay of circulating C-reactive protein: Age-related values in the adult general population, *Clin. Chem.*, 2000, 46, 934–938.

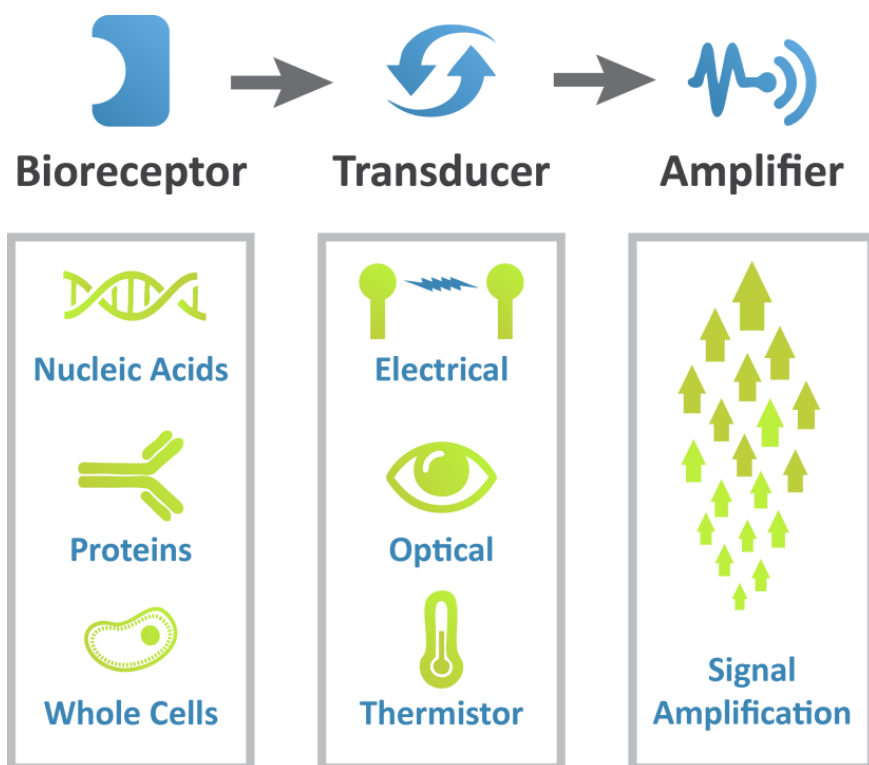
Al-Sheikh and co-workers evaluated an immunoradiometric assays specific for the CK-MB isoenzyme for detection of acute MI. In this study 215 patients were evaluated, from the 215 patients, 103 were admitted to the coronary care unit and the rest was admitted to the emergency room. It was found the immunoradiometric assay had a diagnostic sensitivity, specificity and accuracy of 100% and was found to be more accurate than electrophoresis, another technique used to detect the MI biomarker.<sup>53</sup> Brieitbart and co-workers used an immunoradiometric sandwich assay for the highly specific detection of myostatin predomain in serum of healthy individuals and patients. They test the serum samples of 169 patients with heart failure, 53 patients with cancer and 44 patients with chronic pulmonary disease. The immunoradiometric assay had a detection limit of 0.7 ng/mL and the specificity of the assays was demonstrated with size-exclusion chromatography, but they could not detect increase in myostatin levels in

patients with chronic pulmonary disease.<sup>54</sup> It is evident that the immunoradiometric has been a popular option for MI detection; however, there are some drawbacks which limit its use as a high throughput detection system. The restricted availability of antigens may be a factor in limiting the immunoradiometric assays since large amounts of peptides are required as an immunoadsorbent. In addition, the preparation of reagents is demanding and the labeled antibody has to incubate for up to two weeks therefore waiting on results takes time.<sup>55</sup> Electrochemical biosensors are emerging as an alternative for the early detection of MI biomarkers as they are simple and fast.

## **2.4 Electrochemical biosensors**

Research and development of biosensors has become important over the last few years mainly due to their advantageous properties such as potential miniaturization, portability and low cost as compared to the heavy desktop lab-based methods. Another element contributing the interest in the research and development of biosensors is the rapid growth of biomaterials, especially when it comes to availability and application.<sup>56</sup> Biosensors are analytical devices that convert a biological recognition system into an electrical signal.<sup>57</sup> A typical biosensor consist of three main components, that is, a mediator which converts substrate to products; a transducer which converts a reaction to a measurable signal; and an amplifier where the signal gets processed for display.<sup>58</sup> The purpose of the recognition system is to provide the sensor with a high degree of selectivity for the analyte to be measured. There are various types of biosensors being used such as aptamer-based, enzyme-based, tissue-based, immunosensor and DNA - based.<sup>59</sup> Today more than half of the sensors described in literature is electrochemical and can be classified as potentiometric, conductometric and amperometric sensors.<sup>60</sup> A potentiometric sensor measures the potential difference between two electrodes under the conditions of no current flow. The measured potential may then be used to measure the analytical quantity of interest, which is generally the concentration of some component in solution.<sup>61</sup> A conductometric sensor relies on the disassociation of a dissolved substance and the electrolyte into ions which then migrate due to an induced electric field. The induced electric field is caused by the potential difference applied, thus the current measured is caused by the ion movement towards the electrodes where the ions are neutralized and isolated as neutral atoms.<sup>62</sup> Amperometric sensors measure the current response to detect the concentration of an analyte at a fixed potential. A

voltage is applied between two electrodes during the measurement and the current is measured only when the potential is applied.<sup>63</sup> Below is a scheme illustrating the operating principles of a typical biosensor.



**Scheme 2.4:** Typical working principle of biosensors. Reprinted from D. Pizzoni, P. Pittia, M. Del Carlo, D. Compagnone and C. Di Natale, Oligopeptides-Based Gas Sensing for Food Quality Control, Sensors and Microsystems, Proceedings of the 17th National Conference, Brescia, Italy, 5-7 February 2013, *Springer Netherlands*, 2013, 268, 15–23.

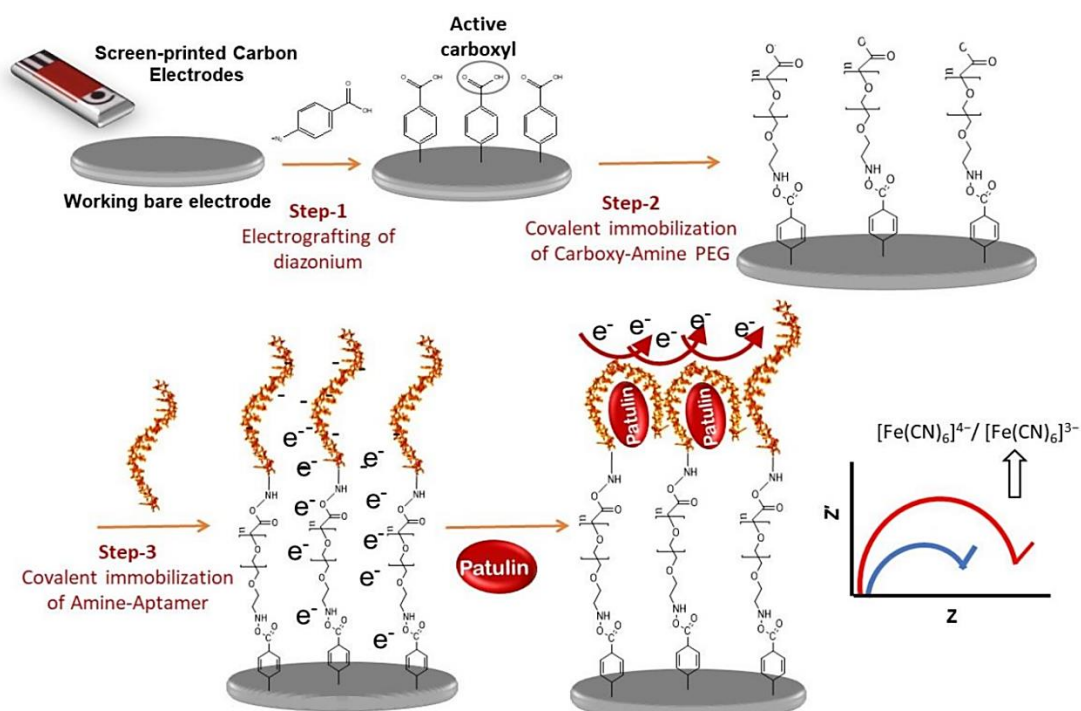
The applications of biosensors are vast ranging from the food sector, environmental sector to the medical field. In the environmental sector biosensors are used to detect heavy metals. Heavy metals are currently the cause of serious pollution problems and even in small concentrations they are a threat to the environment and human population; due to the fact that they are non-biodegradable.<sup>64</sup> Dominguez-Renedo and co-workers developed a urease based amperometric biosensor for the inhibitive determination of Hg (II). Screen-printed carbon electrodes (SPCE) and gold modified screen printed carbon electrodes (AuNPs/SPCE) were used as supports for the cross-linking immobilization of the enzyme urease. The limit of detection obtained for Hg (II) for the urease/SPCE biosensor was,  $4.2 \times 10^{-6}M$ , and for the urease/AuNPs/SPCE it

was,  $5,6 \times 10^{-8} M$ , which shows significant advantages in terms of selectivity and sensitivity over other urea amperometric biosensors for the determination of Hg (II).<sup>65</sup> In the food sector due to the recent advancements in nanotechnology, biosensors are being applied in food safety and becoming a key focus in research and development.<sup>66</sup> Antiochia and co-workers developed an amperometric mediated carbon nanotube paste biosensor for fructose determination. The biosensor was formed by a carbon nanotube paste electrode (CNTPE) modified with an electropolymerized film of 3,4-dihydroxybenzaldehyde for fructose determination. The biosensor had a detection limit of  $1 \times 10^{-6} M$  and showed good reproducibility.<sup>67</sup> In the medical field biosensors are constantly being applied for early detection of biomarkers for cancer, tuberculosis and heart attacks. Myuang and co-workers developed a graphene-encapsulated nanoparticle-biosensor for the selective determination of human epidermal growth factor receptor 2 (HER-2) and epidermal growth factor receptor (EGFR) which are biomarkers for breast cancer. The biosensor was able to detect HER-2 and EGFR at very low detection limits of 1 pM and 100 pM respectively with a high specificity.<sup>68</sup> It is evident that biosensors have become the alternatives to most systems (lab on bench or floor standing laborious equipment) due to the fact that new and exciting approaches can be applied to make these detection systems more specific, simple, sensitive, portable and reliable. For this reason, the presented study focused on developing an aptamer-based sensor as detection strategy. The following section describes the working principle of aptasensors.

### **2.4.1 Aptasensors**

Aptamers are single stranded DNA or RNA oligonucleotides which are able to bind to their target with a high selectivity and affinity; they are identified from a library of nucleic acids by an in vitro selection process known as Systematic Evolution of Ligands by Exponential Enrichment (SELEX).<sup>69</sup> The SELEX process starts off with a chemically synthesized random DNA oligonucleotide library of  $10^{13}$ - $10^{15}$  sequences. The DNA pool is then incubated with the target followed by subsequent washing steps to separate the unbound and weakly bound oligonucleotides from the resulting bound complex. The target bound oligonucleotide sequence is eluted and amplified by polymerase chain reaction (PCR) leading a double stranded DNA sequence (dsDNA).

The dsDNA is then transformed into the single stranded DNA sequence (ssDNA) aptamer by purification.<sup>70</sup> Aptamers has been proposed a substitute for antibodies due to their similar recognition abilities, but aptamers have superior characteristics as compared to antibodies. Aptamers are small in size, high stability, easy synthesis, adaptive modification with various functional groups and nanomaterials and cell free evolution.<sup>71</sup> An aptasensor is a particular class of biosensor where the DNA or RNA aptamer act as the biological recognition element. In an aptasensor, the aptamer recognizes its molecular target against which it was previously in vitro selected. Aptasensors can be easily manipulated to detect a variety of aptamer-target reactions simultaneously.<sup>72</sup> Electrochemical aptasensors uses an electrode surface to immobilize the aptamer and hold an electrochemical transducer to monitor the aptamer-target interaction, by detecting current or potential changes that occurs at the transducer/bioreceptor interface/surface.<sup>73</sup> Below is a schematic representation of an electrochemical aptasensor.



**Scheme 2.5:** Working principle of an electrochemical aptasensor. Reprinted from J. Wang, Electrochemical biosensors: Towards point-of-care cancer diagnostics, *Biosens. Bioelectron.*, 2006, 21, 1887–1892.

QDs are important in aptasensor systems as it creates a sensitive, robust and specific sensing system due to the unique properties associated with it. QDs assists in the transfer of electrons between the aptamer and the target creating mediating platform that increases the electrochemical signal.<sup>74</sup> Aptamers can be modified onto QDs using four major strategies i) self-assembly between QDs and DNA; ii) biospecific interactions such as the biotin-avidin where biotin can be linked to the QDs by its carboxyl groups; iii) covalent interactions where the aptamer is covalently bonded to chemical groups e.g. hydroxyl groups; iv) nucleic acid hybridization where aptamer functionalization is achieved through hybridization of the extended nucleotide sequence with its complementary sequence modified on the surface of the QDs.<sup>75</sup> In literature aptasensors has been applied in early detection methods for heart disease. Bruno and co-workers preliminary developed a DNA aptamer-magnetic bead capture electrochemiluminescence sandwich assay for brain natriuretic peptide (BNP). They selected fifty-two DNA sequence aptamer candidates for binding to the biomarker BNP. The aptamers were screened to rank their affinities against BNP by an aptamer-based enzyme-linked immunosorbent assay (ELISA) microplate assay. The aptamers with the highest affinity from the ELISA screening were also paired in all aptamer combinations and screened for electrochemiluminescence assay potential in capture aptamer-magnetic bead and ruthenium trisbipyridine-reporter aptamer sandwich formats. The top electrochemiluminescence sandwich combinations utilized the same aptamer pair in either capture or reporting roles with nanogram to low pictogram per milliliter levels in 50% human serum.<sup>76</sup> Negahdary and co-workers developed an aptasensor for the detection of human cardiac troponin I (cTnI) which is a biomarker for MI using an array of gold-nanodumbbells. The gold-nanodumbbells were applied as the transducer for the immobilization of the 76-mer cTnI aptamer to form the electrochemical cTnI aptasensor. The cTnI aptasensor demonstrated a wide linear range from 0,05 ng/mL to 500 ng/mL with a limit of detection of 8 pg/mL. The aptasensor showed a sensitivity of 100% and specificity of 85% when challenged with blood serum samples.<sup>77</sup> The detection of BNP has also been explored. Patil and co-workers developed a platinum wire array aptasensor for the detection of BNP. Various platinum wire diameters and surface preparation conditions were selected to determine ideal electrode parameters for the impedimetric detection of BNP.<sup>78</sup> Matsuura and co-workers developed a surface electrochemical enzyme immunoassay for the detection of BNP. First a certain concentration of BNP sample was added to a solution containing anti-BNP antibody

modified with acetylcholinesterase (AChE) to undergo the immunological reaction. Then BNP-modified gold nanoparticles were added into the BNP/AChE-labeled anti-BNP antibody solution so that unreacted AChE-labeled anti-BNP antibody was removed from the assay solution. Then the AChE activity was measured in solution based on the chemisorption/electrochemical reductive desorption process of the thiol compound on a silver electrode. BNP could be determined in the concentration range of 20-200 pg/mL which was high enough for the measurement of the peptide hormone in blood samples.<sup>79</sup>

This research study will use an amine functionalized aptamer sequence that will be modified on novel NiSe<sub>2</sub> QDs attached to a carbon based substrate by using a self-assembly interaction, thus creating an aptasensor for the detection of a cardiac biomarker known as brain natriuretic peptide.

## **2.5 Characterization Techniques**

### **2.5.1 Spectroscopic Techniques**

#### **2.5.1.1 Ultraviolet-Visible Spectroscopy**

Ultraviolet-visible spectroscopy (UV-Vis spectroscopy) is a physical technique that uses light in the visible, ultraviolet and near infra-red ranges. According to Beer Lamberts law the absorbance of a solution is directly proportional to the concentration of the absorbing species in solution and the path. Absorbance can be denoted by Equation 2.1 below,

$$A = abc \tag{2.1}$$

where A is the absorbance; a the absorptivity in (mol/cm); b the path length in (cm); and c is the concentration in (mol/L).<sup>80</sup> Therefore at a fixed path length one will be able to measure the concentration of the absorber in solution using UV-Vis. The working principle of UV-Vis can be described as follows: a light source will pass light through a

collimator that transfers the light to a prism grating that splits the wavelength through the sample and reaches the detector producing an absorbance spectrum. When the light passes through the molecule or ion it will absorb in the visible or ultraviolet region due to the radiation that causes an electronic transition within its structure. The energy supplied by light will promote electrons from their ground state orbitals to higher energy excited orbitals or anti-bonding orbitals.<sup>81</sup> There are potentially three types of ground state orbitals that can be involved namely, i)  $\sigma$  (bonding) molecular orbital; ii)  $\pi$  (bonding) molecular orbital, and iii)  $n$  (non-bonding) atomic orbital.<sup>82</sup> Therefore the following electronic transitions can occur by the absorption of visible and ultraviolet light:

- i)  $\sigma$  to  $\sigma^*$
- ii)  $n$  to  $\sigma^*$
- iii)  $n$  to  $\pi^*$
- iv)  $\pi$  to  $\pi^*$

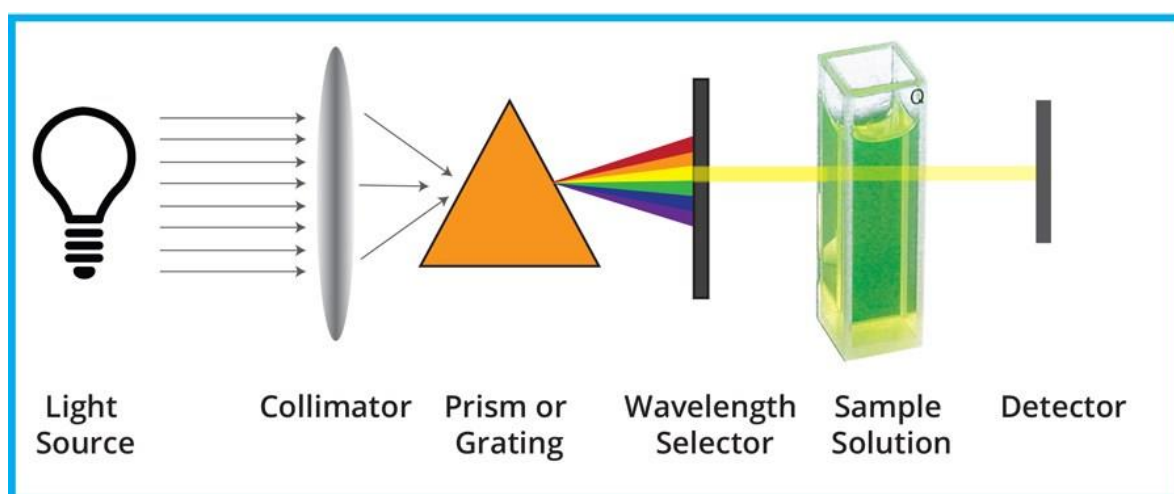


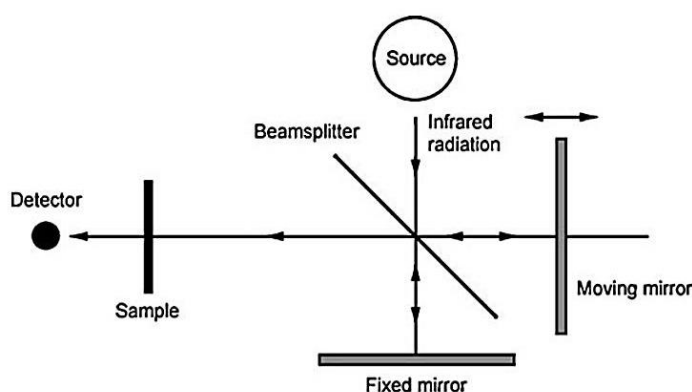
**Figure 2.5:** Operating principle of UV-Vis Spectroscopy. Reprinted from R. Wegh, H. Donker, A. Meijerink, R. Lamminmäki and J. Hölsä, Vacuum-ultraviolet spectroscopy and quantum cutting for, *Phys. Rev. B - Condens. Matter Mater. Phys.*, 1997, 56, 13841–13848.

Applications of UV-Vis spectroscopy include quantitative analysis of different materials, measuring reaction rates, measuring equilibrium constants and measuring film thickness.<sup>83</sup> Hamam and co-workers used UV-Vis spectroscopy to measure the

band gap of zinc phthalocyanide nanoparticles (ZnPc-np) and its bulk counterpart.<sup>88</sup> It was concluded that the shift in the absorption spectrum was evident of nanoparticle formation. The nanoparticles bandgap energy was recorded at 3.91 eV and its bulk counterpart band gap energy was recorded at 1.59 eV, therefore the ZnPc-np absorption spectrum shows a shift towards higher energy photons.<sup>84</sup> UV-Vis spectroscopy will be used to measure the absorbance and band-gap of the novel mercaptosuccinic capped nickel selenide quantum dots.

### 2.5.1.2 Fourier-Transform Infrared Spectroscopy

Fourier-transform infrared spectroscopy (FTIR) is a technique used to obtain an infrared spectrum of emission or of absorption of different species such as solids, liquids and gases. The operating principle of FTIR consists of irradiation of sample material with infrared radiation. The absorbed infrared radiation by the material excites molecules to a higher vibrational state. The wavelength of light absorbed is a function of the energy difference between the at rest and excited vibrational states.<sup>85</sup> Through this operating principle FTIR is used as an analytical tool to detect the functional groups of molecules and convey covalent bond information.<sup>86</sup> In the FTIR spectrometer an interferometer is used to modulate the wavelength from a broadband infrared source and the detector measures the intensity of the transmitted or reflected light as a function of its wavelength.<sup>87</sup>



**Scheme 2.6:** General Operating principle of FTIR. Reprinted from D. Ami, R. Posteri, P. Mereghetti, D. Porro, S. M. Doglia and P. Branduardi, Fourier transform infrared spectroscopy as a method to study lipid accumulation in oleaginous yeasts, *Biotechnol. Biofuels*, 2014, 7, 1–14.

Applications of FTIR include analysis of thin films and coatings, microanalysis of small sections of materials to identify contaminants and verification of the quality of incoming/outgoing materials.<sup>88</sup> Kapatkar and co-workers synthesized thioglycolic acid capped cadmium selenide quantum dots (TGA-CdSe QDs) to investigate its optical and structural properties. FTIR was used to characterize the structural properties of the QDs by confirming the capping of TGA on the QDs. This was done by comparing the FTIR spectrum of the TGA capping agent alone with that of the TGA-CdSe QDs. The disappearance of the thiol peak at  $2650\text{ cm}^{-1}$  is a clear indicator of the successful capping of TGA on the CdSe QDs as well as the carboxylic stretch, at  $1672\text{ cm}^{-1}$ , and C-H bend, at  $2969\text{ cm}^{-1}$ .<sup>89</sup> FTIR will be used in this study to measure the functional groups present on the mercaptosuccinic acid capped nickel selenide quantum dots and confirm if the novel synthesized QDs are capped with mercaptosuccinic acid.

### **2.5.1.3 X-ray diffraction**

X-ray diffraction (XRD) is a non-destructive technique used to characterize crystalline materials. It provides information on the structures, phases, preferred crystal orientations and other structural parameters such as average grain size, crystallinity, strain and crystal defects.<sup>90</sup> The X-ray diffraction peaks are produced by the constructive interference of a monochromatic beam of X-rays scattered at specific angles from each set of lattice planes in a sample. The peak intensities are determined by the distribution of the atoms within the lattice.<sup>91</sup> The sample only produces X-rays when the interaction of the incident rays with the sample produces constructive interference and satisfies Bragg's law given by Equation 2.2 below.

$$n\lambda = 2d\sin\theta \quad 2.2$$

where,  $\lambda$  is the wavelength of the X-ray,  $n$  is an integer denoting the order of reflection,  $\theta$  is one half of the angle between the incident and scattered beams and  $d$  is the interplanar spacing.<sup>92</sup>

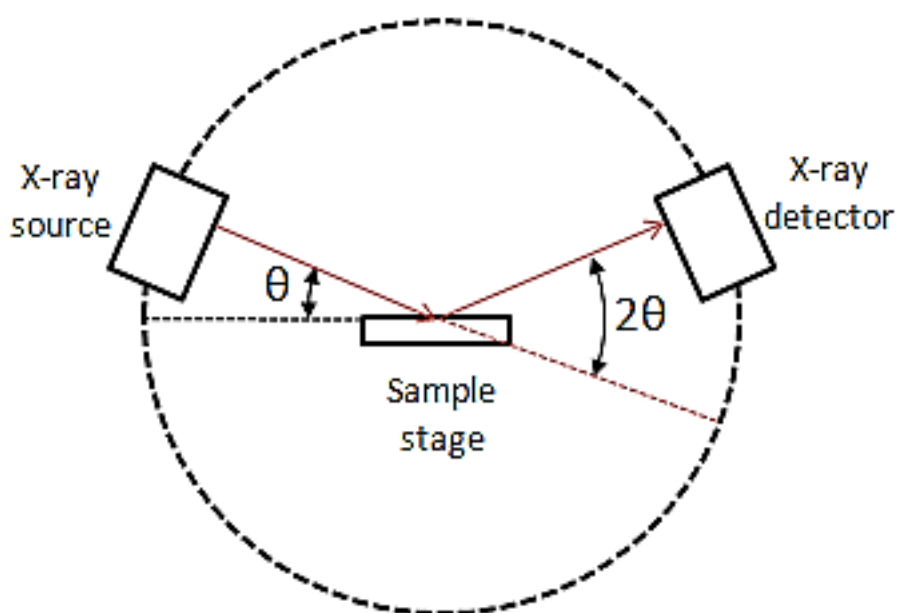


**Figure 2.6:** Typical working principle of XRD. Reprinted from A. A. Bunaciu, E. gabriela Udriștioiu and H. Y. Aboul-Enein, X-Ray Diffraction: Instrumentation and Applications, *Crit. Rev. Anal. Chem.*, 2015, 45, 289–299.

Applications of XRD include measuring sample purity, determination of unit cell dimensions and characterize crystalline materials.<sup>93</sup> Jian and co-workers prepared zinc selenide quantum dots (ZnSe QDs) embedded in silicon dioxide (SiO<sub>2</sub>) thin films by the sol-gel process. The phase structure of the thin films was investigated by XRD characterization. The XRD pattern of thin films indicated that the ZnSe QDs belong to the sphalerite phase structure or in other words the cubic ZnSe.<sup>94</sup> In the present study XRD will be employed to measure the crystallinity and phase structure of the mercaptosuccinic acid capped nickel selenide quantum dots.

### 2.5.1.4 Small Angle X-ray Scattering

Small angle X-ray scattering (SAXSpace) is an analytical tool used to determine the structure of particles in terms of average particle size or shapes. The material for analysis can be either a solid or a liquid. In SAXSpace the atoms inside the sample will scatter the incident radiation into all directions, which gives a background radiation that is constant at small angles.<sup>95</sup> The particles inside the sample will produce additional scattering which is due to the fact that the particles are made of different materials or density, and are in the size range of the X-ray wavelength. By measuring the angle-dependent distribution of the scattered radiation, it is therefore possible to draw conclusions about the average particle structure. Surface-near particles can also be measured selectively when the X-rays hit a flat sample almost parallel to its surface and the scattering signal is measured in reflection mode.<sup>96</sup> This is new variant of SAXSpace called GI-SAXS where GI stands for grazing incidence. The SAXSpace method is accurate, non-destructive and it requires only a minimum of sample preparation. Application areas of SAXSpace include biological materials, polymers, colloids, nanocomposites, metals and pharmaceuticals.

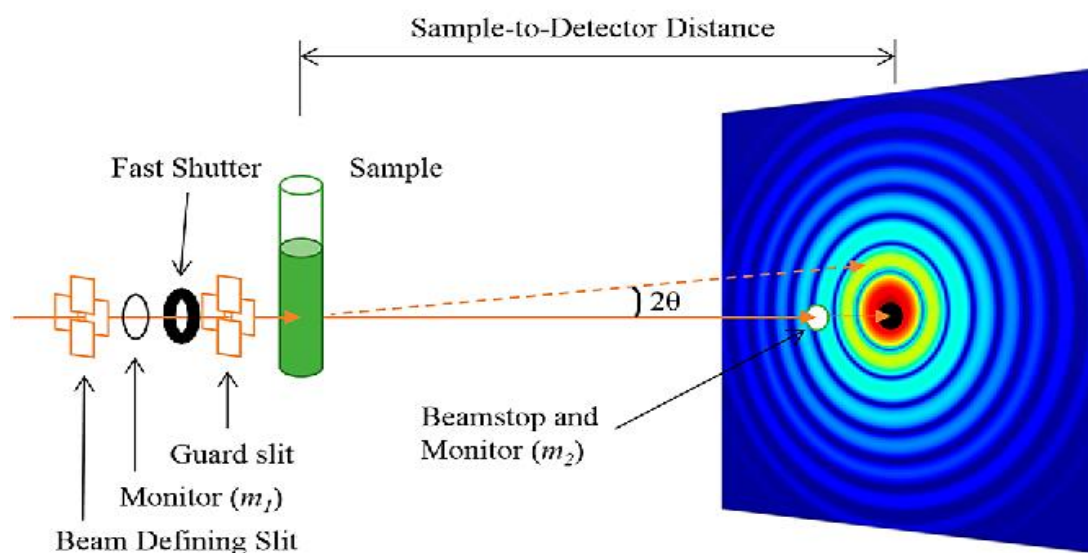


**Figure 2.7:** SAXSpace working principle. Reprinted from H. D. T. Mertens and D. I. Svergun, Structural characterization of proteins and complexes using small-angle X-ray solution scattering, *J. Struct. Biol.*, 2010, 172, 128–141.

Champagon and co-workers investigated the size of cadmium sulphide quantum dots (CdS-QDs) in glasses using SAXSpace and high resolution transmission microscopy (HR-TEM) and investigating the correlation between these two measurements. It was discovered that the size of the QDs investigated through SAXSpace was 8nm and the size of the QDs investigated through HR-TEM was 7.8 nm which was slightly lower than SAXSpace but still in good agreement. It was concluded that the discrepancies in the sizes of the QDs is due probe in each technique and the interactions used by each technique.<sup>97</sup> SAXSpace will be used to measure the size and morphology of the mercaptosuccinic acid capped nickel selenide quantum dots.

## **2.5.2 Microscopic Techniques**

### **2.5.2.1 High Resolution Transmission Electron Microscopy (HR-TEM)**

High resolution transmission electron microscopy (HR-TEM) is techniques that allows for the direct imaging of the atomic structure of a sample as well as provide information about the topographical, morphological and crystallographic information about the particles of the atom.<sup>98</sup> HR-TEM is not only a technique that provides atomic resolution lattice images it also provides chemical information at a spatial of 1 nm. In HR-TEM a beam of electrons passes through the sample causing some parts of the sample to be transmitted which depend on the thickness and electron transparency of the sample. The transmitted part of the sample is then focused by an objective lens into an image on a charge coupled device (CCD) camera. The image is then passed down a column by a projector lens which causes the image to enlarge for the user to see.<sup>99</sup>

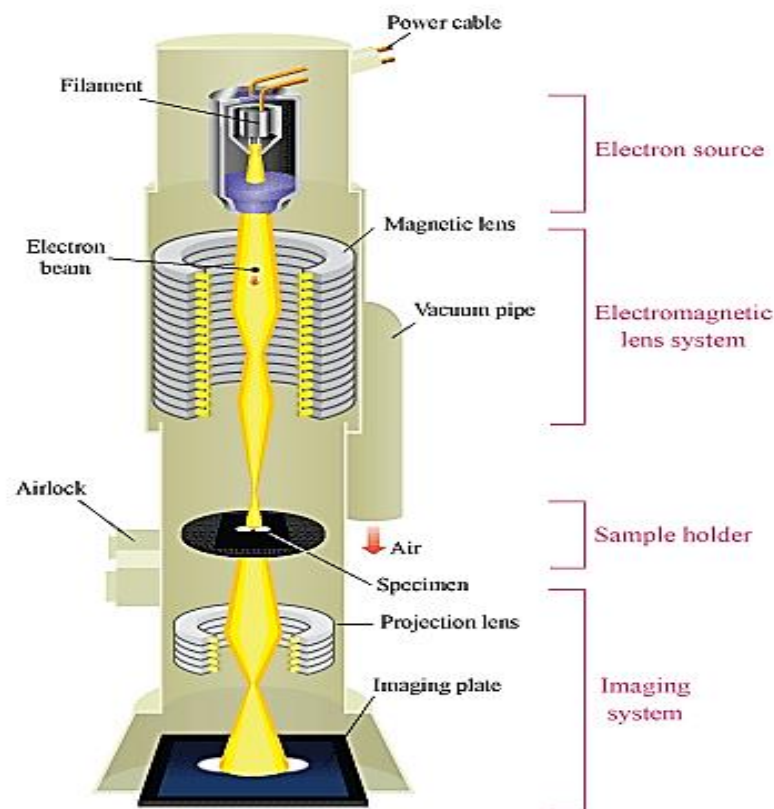


**Figure 2.8:** HR-TEM operating principle. Reprinted from G. C. Capitani and M. Mellini, High-resolution transmission electron microscopy (HRTEM) investigation of antigorite polysomes ( $m = 15$  to  $18$ ), *Am. Mineral.*, 2007, 92, 64–71.

The structural characteristics of single nanocrystals can be characterized by the finely focused electron probe of the HR-TEM tool. The structural characteristics include surface morphology, size, density and strain fields.<sup>100</sup> Li and co-workers prepared carbon quantum dots with tunable photoluminescence by laser passivation.<sup>104</sup> HR-TEM was used to study the morphology and size of the carbon quantum dots. The carbon quantum dots were 10 nm in size, it had a core-shell structure with the outer layer being amorphous and the inner layer was polygon-like with a shallow centre.<sup>101</sup> Here, HR-TEM will be used to study the morphology and size of the mercaptosuccinic acid capped nickel selenide quantum dots and will be complemented alongside small angle x-ray scattering.

### 2.5.2.2 High Resolution Scanning Electron Microscopy (HR-SEM)

High resolution scanning electron microscopy (HR-SEM) is a technique that is used to study the surface topography and morphology specimen. HR-SEM is coupled to an energy dispersive X-ray spectrometer and with this feature, it can provide quantitative and qualitative chemical analysis.<sup>102</sup> In HR-SEM a beam of electrons is generated by a tungsten filament; the electron beam is then accelerated with a high voltage (20 kV) and passes through a system of apertures and electromagnetic lenses to produce a thin beam of electrons. The beam then scans the surface of the specimen. The interaction of the beam of electrons and the specimen causes backscattered electrons which are then picked up by the detector to produce an image<sup>103</sup>

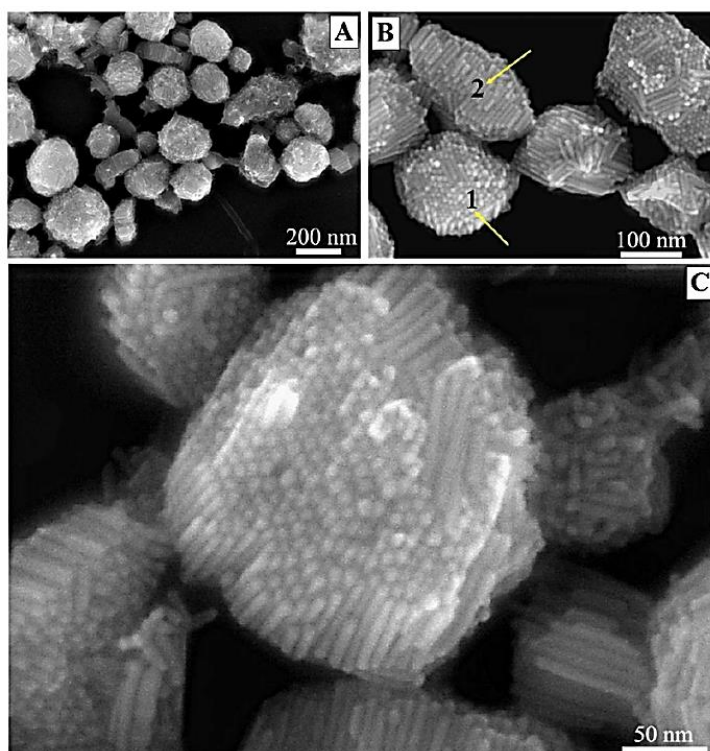


**Figure 2.9:** A typical SEM image of CdSe/ZnS quantum dots. Reprinted from H. Zhang, P. Wang, Q. Zhou and Y. Wang, A Novel Method for the Detection of Chlorpyrifos by Combining Quantum Dot-labeled Molecularly Imprinted Polymer with Flow Cytometry, *Anal. Lett.*, 2018, 51, 921–934.

The main difference between HR-SEM and HR-TEM is that HR-SEM detects scattered electrons emitted from the surface of the sample, while HR-TEM detects transmitted electrons. The accelerated voltage ranges from 10 to 40 kV for HR-SEM and for HR-

TEM >100 kV.<sup>104</sup> Ermakov and co-workers synthesized lead sulphide quantum dots (PbS QDs) and used HR-SEM to investigate the three-dimensional lattice of these PbS QDs in flakes.<sup>105</sup> It was observed that the QDs had a flower-like structure in the form of flakes. In this study, HR-SEM will be used to investigate the topography as well as morphology of the mercaptosuccinic acid nickel selenide quantum dots.

## 2.5.3 Electrochemical Techniques

### 2.5.3.1 Cyclic voltammetry

Cyclic voltammetry (CV) is an electrochemical technique used to investigate the oxidation and reduction redox processes of a molecular species. The essential elements needed for an electrochemical setup are the working electrode, like carbon, platinum or gold; reference electrode, like silver/silver chloride and counter electrode like a platinum wire. Another component is the electrolyte solution like phosphate buffer, which allows the current to pass and is used in high concentrations (normally 0.1 M). In addition to see an electrochemical response an electro active probe is also required, which is added in low concentrations typically  $10^{-3}$  M.<sup>106</sup> CV working principle is based on monitoring the current when the potential applied at the working electrode is varied in both forward and reverse directions at a certain scan rate. For example, when scanning in the forward direction to more positive potentials an oxidation reaction for species R occurs and produces species O given by the Equation 2.3 below:<sup>107</sup>



When scanning in the reverse direction to more negative potentials the species O is reduced back to species R given by the Equation 2.4:



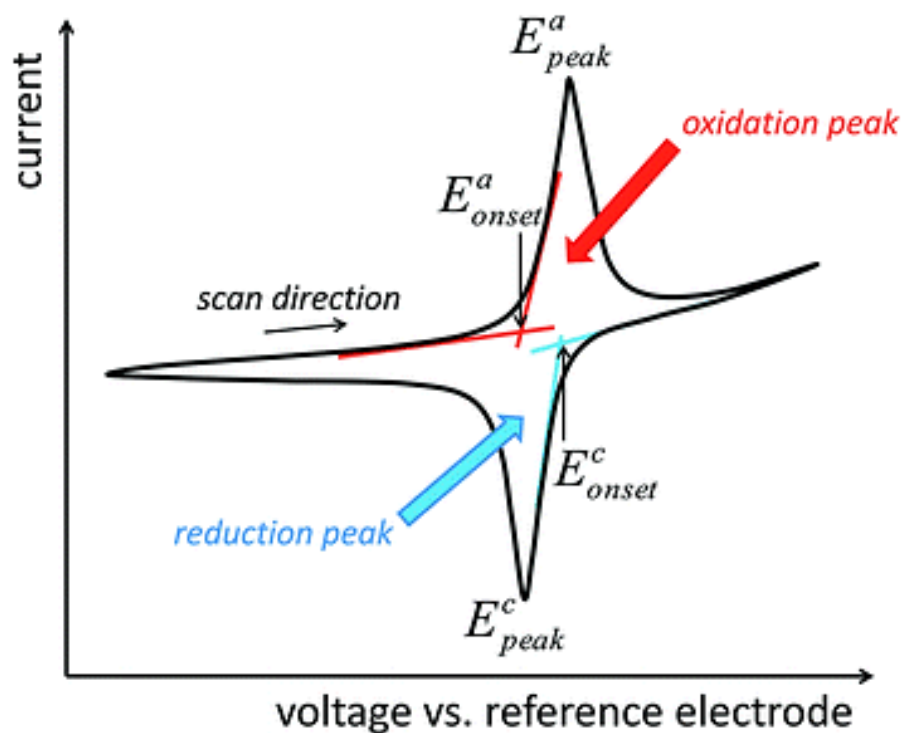


**Figure 2.10:** A typical Cyclic voltammogram. Reprinted from H. Borchert, Solar Cells Based on Colloidal Nanocrystals, *Springer Ser. Mater. Sci.*, 978-3-319.

The redox systems that can be obtained in CV are reversible, quasi-reversible and irreversible systems. Characterizing a cyclic voltammogram as one of these redox systems depends on the two peak currents and two peak potentials. For a reversible system the peak current is given by the Randels-Sevick, Equation 2.5:<sup>108</sup>

$$i_p = (2.69 \times 10^5) n^{\frac{3}{2}} A C D^{\frac{1}{2}} v^{\frac{1}{2}} \quad 2.5$$

where  $n$  is the number of electrons,  $A$  is the area of the electrode ( $\text{cm}^2$ ),  $C$  is the concentration ( $\text{mol}/\text{cm}^3$ ),  $D$  is the diffusion coefficient ( $\text{cm}^2/\text{s}$ ) and  $v$  is the scan rate ( $\text{V}/\text{s}$ ). Another important parameter is the peak to peak separation for a reversible system. Thus, the peak to peak separation is:

$$\Delta E_p = E_{pa} - E_{pc} = 57 \text{ mV}/n \quad 2.6$$

For a irreversible systems the size of the individual peaks are reduced and they are widely separated. The peak current is given by the Equation 2.7:<sup>109</sup>

$$i_p = (2.99 \times 10^5) n (\alpha n_a)^{\frac{1}{2}} A C D^{\frac{1}{2}} \nu^{\frac{1}{2}} \quad 2.7$$

where  $\alpha$  is the charge transfer coefficient,  $n_a$  is the number of electrons involved in the charge transfer step,  $A$  is the area of the electrode in  $\text{cm}^2$ ,  $D$  is the diffusion coefficient in  $\text{cm}^2/\text{s}$ ,  $\nu$  is the scan rate in  $\text{V}/\text{s}$  and  $C$  is the concentration in  $\text{mol}/\text{cm}^3$ . Therefore, for an irreversible system the peak to peak separation is larger than  $57 \text{ mV}/n$ .<sup>110</sup>

Osipovich and co-workers synthesized water-soluble thioglycolic acid capped cadmium telluride quantum dots (TGA-CdTe-QDs) and used CV to measure the electrochemical behavior of the CdTe QDs. The CV measurement was carried out on a gold electrode surface in an acetate buffer with pH 5. The CV results showed that when the CdTe QDs are introduced into the buffer solution with pH 5, the thiolic groups are protonated and the cadmium sulphur bonds (Cd-S) on the surface is disrupted. This causes the drop of the QDs stability against oxidation.<sup>111</sup> In this present study CV will be used to investigate the electrochemical behavior of the mercaptosuccinic acid capped nickel selenide quantum dots (MSA-NiSe<sub>2</sub> QDs) on carbon and gold electrodes as well as to show the analytical response for the different steps in the sensor fabrication process.

### 2.5.3.2 Differential pulse voltammetry (DPV)

Deep pulse voltammetry (DPV) is an electrochemical technique and a derivative of staircase voltammetry. In DPV a series of regular voltage pulses are superimposed on the potential linear sweep or stair steps. The current is then measured before each potential change and the current difference is plotted as a function of potential.<sup>112</sup>

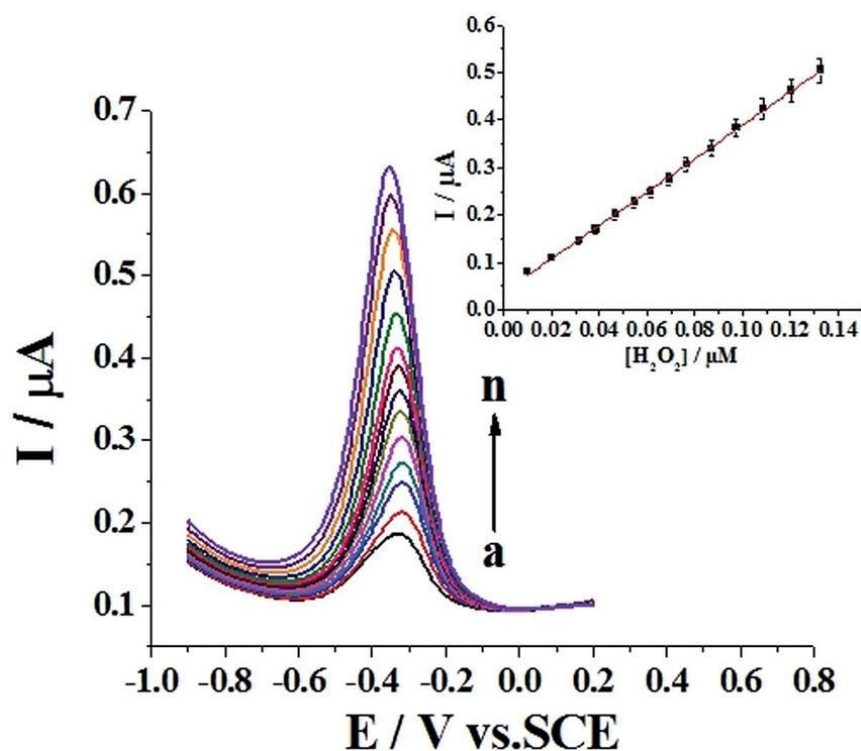


**Figure 2.11:** Typical DPV graph. Reprinted from (W. Wu, Y. Fang, C. Zhu, S. Chen, T. Li, L. Wu, N. Bao, Y. Liu and H. Gu, Fabrication of highly stable and sensitive electrochemical sensor from hemoglobin-Au nanocomposites and its analytical applications, *RSC Adv.*, 2017, 7, 42884–42890.

Applications of DPV include the determination of metal ion concentrations in aqueous solutions to parts-per-billion levels and the quantitative determination of pharmaceutical compounds.<sup>113</sup> Dong and co-workers used DPV anodic stripping for the sensitive detection of Pb (II) on a gold nanoparticle/polyaniline/graphene modified electrode. Under optimal conditions it was discovered that there was good linear relationship with the stripping peak currents and the concentration of Pb (II) with correlation coefficient of  $R^2 = 0.9995$  in the concentration range of 0.5 to 10 nM. The limit of detection was 0.1 nM. In this research study DPV was used a detection system for the detection of Brain natriuretic peptide (BNP).

### 2.5.3.3 Electrochemical Impedance Spectroscopy (EIS)

Electrochemical Impedance Spectroscopy (EIS) is an electrochemical tool that is used to study the mechanisms of electrochemical reactions and evaluating the properties of wide range of materials.<sup>114</sup> EIS is measured by applying an alternating potential to an

electrochemical cell and measuring the current through the cell. The response to this applied potential is an alternating current signal that can be analyzed as a sum of sinusoidal functions. In EIS the applied potential is a small excitation signal this is done so that the response is linear. In a linear system, the current response to a sinusoidal potential will be a sinusoid at the same frequency but shifted in phase.<sup>115</sup>

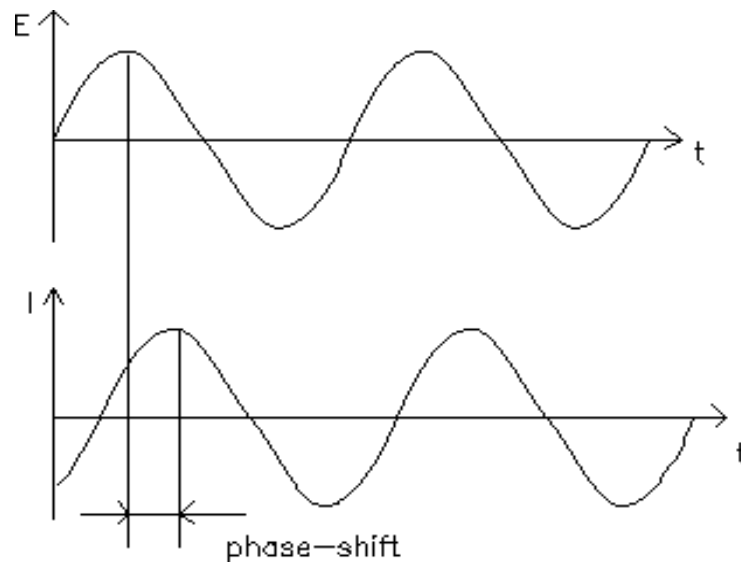


**Figure 2.12:** Current response to an applied sinusoidal potential in a linear EIS system. Reprinted from J. Halliwell, A. C. Savage, N. Buckley and C. Gwenin, *Electrochemical impedance spectroscopy biosensor for detection of active botulinum neurotoxin*, *Sens. Bio-Sensing Res.*, 2014, 2, 12–15.

The excitation signal can be expressed as a function of time, in the form:

$$E_t = E_0 \sin(\omega t) \quad 2.8$$

where  $E_t$  is the applied potential at time  $t$  is,  $E_0$  is the amplitude of the signal and  $\omega$  is the radial frequency. The correlation between radial frequency (rad/second) and frequency (hertz) is expressed as follows:

$$\omega = 2\pi f \quad 2.9$$

In a linear system the response of  $I_t$  is shifted in phase ( $\phi$ ) and has a different amplitude  $I_0$ . Expressed as follows:

$$I_t = I_0 \sin(\omega t + \phi) \quad 2.10$$

An expression for the impedance can then be derived and expressed as follows:

$$Z = \frac{E_t}{I_t} = \frac{E_0 \sin(\omega t)}{I_0 \sin(\omega t + \phi)} = Z_0 \frac{\sin(\omega t)}{\sin(\omega t + \phi)} \quad 2.11$$

The impedance can be represented as a complex number by the following equation below:

$$z(\omega) = \frac{E}{I} = Z_0 (\cos\phi + j\sin\phi) \quad 2.12$$

The data for EIS can be represented by a nyquist plot where the expression of  $Z(\omega)$  is composed of a real and an imaginary part. In a nyquist plot the real part is plotted on the y-axis and the imaginary part is plotted on the x-axis. Also each plot on the nyquist plot is a representation of the impedance at one frequency.<sup>116</sup>

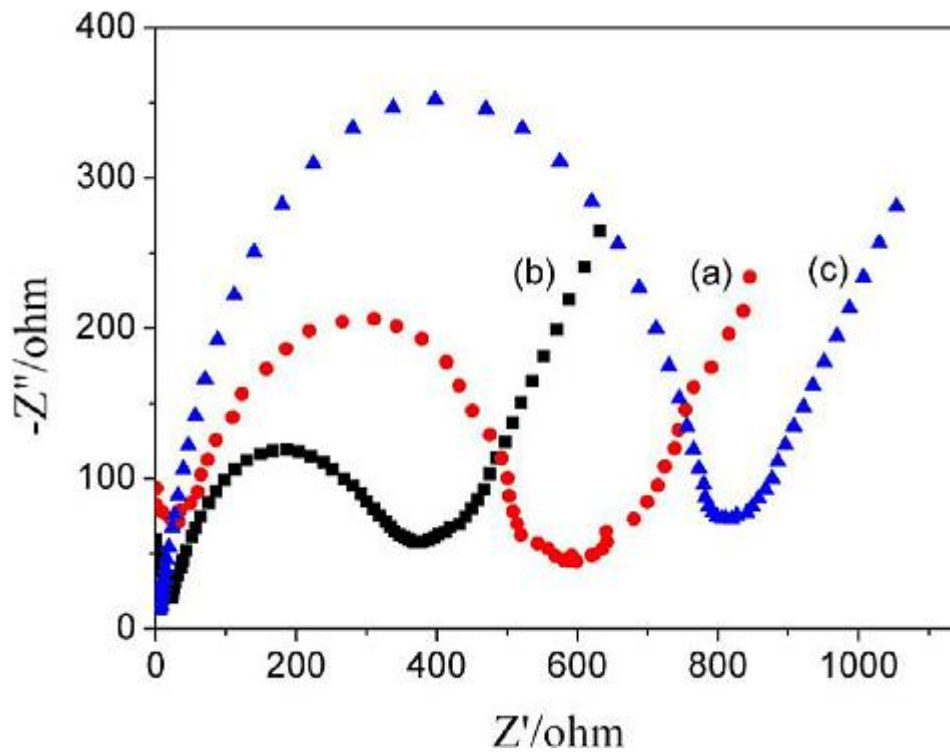


**Figure 2.13:** Typical Nyquist plots for EIS. Reprinted from I. R. Ramachandran, V. Mani, S. M. Chen, G. Gnanakumar and M. Govindasamy, Recent developments in electrode materials and methods for pesticide analysis - An overview, *Int. J. Electrochem. Sci.*, 2015, 10, 859–869.

A disadvantage of just using a nyquist plot to represent data is that when you look at any point on the nyquist plot, you cannot tell what frequency was used to record that point. A bode plot is used to complement a nyquist plot and is plotted with log frequency on the x-axis and both the absolute values of impedance and the phase shift on the y-axis.<sup>117</sup>

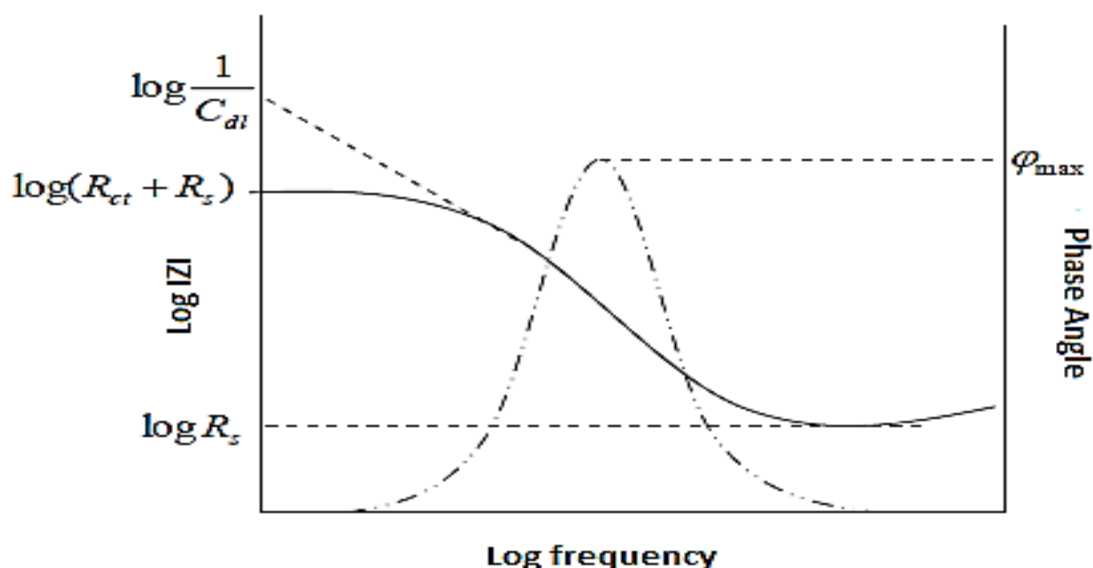


**Figure 2.14:** A typical Bode plot. Reprinted from F. Shahdost-fard and M. Roushani, An impedimetric aptasensor based on water soluble cadmium telluride (CdTe) quantum dots (QDs) for detection of ibuprofen, *JEAC*, 2016, 763, 18–24.

Fard and co-workers designed an impedimetric aptasensor for the detection of ibuprofen using water soluble cadmium telluride (CdTe QDs). The aptamer was amino modified and consisted of 12 bases in addition; it was fabricated on a gold electrode surface. For electrochemical characterization electrochemical impedance was used due to the fact that it provides details in the kinetics of charge transfer through the sensing layer that occurs at the electrodes. A nyquist plot of different electrodes was obtained, at a frequency range of 100 kHz to 0.01 Hz. The results indicated that the charge transfer values ( $R_{ct}$ ) increased for each modification step that is, for the bare gold electrode a  $R_{ct}$  value of 50  $\Omega$  was obtained; by adding CdTe QDs the  $R_{ct}$  value increased to 1680  $\Omega$ , the attachment of the aptamer increased the  $R_{ct}$  value further to 6180  $\Omega$  and finally with the attached of the analyte, ibuprofen, the  $R_{ct}$  value increased to 7090  $\Omega$ . The aptasensor had an excellent linear range up to 20  $\mu\text{M}$ .<sup>118</sup> EIS will be employed in this study to investigate the different steps in the aptasensor fabrication process.

## 2.6 Conclusion

It is evident from literature that quantum dots are of particular interest due to the fact that the size of these materials can be tuned for certain applications such as biological applications. Capping agents such as mercaptosuccinic acid assisted in this application by making the quantum dots water-soluble, which was needed for biological applications. Biomarkers are emerging as alternative methods for early diagnosis of cardiovascular diseases. Brain-natriuretic peptide is considered a good biomarker for cardiovascular disease due to its high sensitivity and specificity. Electrochemical biosensors are emerging as new detection methods for cardiovascular diseases as compared to other early detection methods such as immunoradiometric assays. Aptasensors which are an emerging class of electrochemical biosensors are considered to be more sensitive and specific to cardiovascular diseases due to the incorporation of the QDs which creates a mediating platform by assisting in the electron transfer process between the aptamer and biomarker increasing its sensitivity for detecting cardiovascular diseases. In addition, discussed are the structural, microscopic and electrochemical techniques for characterization of the mercaptosuccinic capped nickel selenide quantum dots.

## References

- 1 A. Alagarasi, Chapter - INTRODUCTION TO NANOMATERIALS, Natl. Cent. Catal. Res., 2011, **3**, 1–23.
- 2 M. Saleh and J. A. Ambrose, Understanding myocardial infarction, 2018, **7**, 1–8.
- 3 H. K. Daima and V. Bansal, Influence of Physicochemical Properties of Nanomaterials on Their Antibacterial Applications, Elsevier Inc., 2015, **20**, 1-13.
- 4 C. Buzea, I. I. Pacheco and K. Robbie, Nanomaterials and nanoparticles: Sources and toxicity, *Biointerphases*, 2007, **2**, 17–71.
- 5 K. Yamamoto, *Nanomaterials*, 2001, **13**, 34–37.
- 6 D. Yao, Y. Liu, J. Li and H. Zhang, Advances in green colloidal synthesis of metal selenide and telluride quantum dots, *Chinese Chem. Lett.*, 2019, **30**, 277–284.
- 7 S. Wu, L. Cheng and Q. Wang, Excitonic effects and related properties in semiconductor nanostructures: Roles of size and dimensionality, *Mater. Res. Express*, 2017, **4**, 1-13.
- 8 T. R. Sandin, Reduced mass and the Bohr radius, *Am. J. Phys.*, 1986, **54**, 393–394.
- 9 Y. H. Kuo, Y. K. Lee, Y. Ge, S. Ren, J. E. Roth, T. I. Kamins, D. A. B. Miller and J. S. Harris, Strong quantum-confined Stark effect in germanium quantum-well structures on silicon, *Nature*, 2005, **437**, 1334–1336.
- 10 M. A. Olshavsky, A. N. Goldstein and A. P. Alivisatos, Organometallic Synthesis of GaAs Crystallites Exhibiting Quantum Confinement, *J. Am. Chem. Soc.*, 1990, **112**, 9438–9439.
- 11 V. G. Reshma and P. V Mohanan, Quantum dots : Applications and safety consequences, 2019, **205**, 287–298.

- 12 R. E. Galian and M. de la Guardia, The use of quantum dots in organic chemistry, *TrAC - Trends Anal. Chem.*, 2009, **28**, 279–291.
- 13 A. G. Kolchinski, D. H. Busch and N. W. Alcock, Gaining control over molecular threading: Benefits of second coordination sites and aqueous-organic interfaces in rotaxane synthesis, *J. Chem. Soc. Chem. Commun.*, 1995, 1289–1291.
- 14 S. K. Aditha, A. D. Kurdekar, L. A. A. Chunduri, S. Patnaik, V. Td and I. F. Kamiseti, MethodsX Aqueous based reflux method for green synthesis of nanostructures : Application in CZTS synthesis, *MethodsX*, 2016, **3**, 35–42.
- 15 Z. Durmus, T. Ozkaya, A. Baykal, M. S. Toprak and Y. Koseog, Journal of Magnetism and Magnetic Materials Reflux synthesis of  $\text{Co}_3\text{O}_4$  nanoparticles and its magnetic characterization, 2009, **321**, 2145–2149.
- 16 J. Luo, H. Wei, F. Li, Q. Huang, D. Li and Y. Luo, Microwave assisted aqueous synthesis of core – shell  $\text{CdSe}_x\text{Te}_{1-x}$  –  $\text{CdS}$  quantum dots, 2014, **5**, 3464–3466.
- 17 M. B. Gawande, S. N. Shelke, R. Zboril and R. S. Varma, Microwave-assisted chemistry: Synthetic applications for rapid assembly of nanomaterials and organics, *Acc. Chem. Res.*, 2014, **47**, 1338–1348.
- 18 T. M. Atkins, A. Thibert, D. S. Larsen, S. Dey, N. D. Browning and S. M. Kauzlarich, Femtosecond ligand/core dynamics of microwave-assisted synthesized silicon quantum dots in aqueous solution, *J. Am. Chem. Soc.*, 2011, **133**, 20664–20667.
- 19 D. S. M. Ribeiro, G. C. S. de Souza, A. Melo, J. X. Soares, S. S. M. Rodrigues, A. N. Araújo, M. C. B. S. M. Montenegro and J. L. M. Santos, Synthesis of distinctly thiol-capped CdTe quantum dots under microwave heating: multivariate optimization and characterization, *J. Mater. Sci.*, 2017, **52**, 3208–3224.
- 20 M. Green, The nature of quantum dot capping ligands, 2010, 5797–5809.
- 21 R. K. Shervedani, A. Farahbakhsh and M. Bagherzadeh, Functionalization of gold cysteamine self-assembled monolayer with ethylenediaminetetraacetic acid as a novel nanosensor, 2007, **587**, 254–262.
- 22 Deepika, R. Dhar, S. Singh and A. Kumar, Effect of capping agents on optical and antibacterial properties of cadmium selenide quantum dots, *Bull. Mater. Sci.*, 2015, **38**, 1247–1252.

- 23 F. Mirnajafizadeh, The Effect Of Capping Agent On Formation Of Particles : Synthesis Of Cadmium Selenide Thiol Capped, 2018, 56–58.
- 24 M. Califano, A. Franceschetti and A. Zunger, Temperature dependence of excitonic radiative decay in CdSe quantum dots: The role of surface hole traps, *Nano Lett.*, 2005, **5**, 2360–2364.
- 25 C. Giansante and I. Infante, Surface Traps in Colloidal Quantum Dots: A Combined Experimental and Theoretical Perspective, *J. Phys. Chem. Lett.*, 2017, **8**, 5209–5215.
- 26 C. M. Phan and H. M. Nguyen, Role of Capping Agent in Wet Synthesis of Nanoparticles, *J. Phys. Chem. A*, 2017, **121**, 3213–3219.
- 27 Y. Li and C. W. Peng, Application of quantum dots-based biotechnology in cancer diagnosis: Current status and future perspectives, *J. Nanomater.*, 2010, **19**, 1-11.
- 28 B. Ajitha, Y. A. Kumar Reddy, P. S. Reddy, H. J. Jeon and C. W. Ahn, Role of capping agents in controlling silver nanoparticles size, antibacterial activity and potential application as optical hydrogen peroxide sensor, *RSC Adv.*, 2016, **6**, 36171–36179.
- 29 G. Lin and X. Wang, Passive tumor targeting and imaging by using quantum dots, *Int. J. Nanomedicine*, 2015, **10**, 335–345.
- 30 J. C. L. Sousa, M. G. Vivas, B. R. C. Vale, J. L. Ferrari and M. A. Schiavon, Effect of Mercaptosuccinic Acid Stabilizer Agent on the Optical Properties of Colloidal CdTe Quantum Dots, 2018, **18**, 651–658.
- 31 U. Brandt, A. Deters and A. Steinbüchel, A jack-of-all-trades: 2-mercaptosuccinic acid, *Appl. Microbiol. Biotechnol.*, 2015, **99**, 4545–4557.
- 32 E. Ying, D. Li, S. Guo, S. Dong and J. Wang, Synthesis and bio-imaging application of highly luminescent mercaptosuccinic acid-coated CdTe nanocrystals, *PLoS One*, 2008, **3**, 1–7.
- 33 H. Ito, A. Iio, K. Tokuhara, H. Sakaue, Y. Kadoya and H. Suzuki, Estimation of the Number of Quantum Dots Immobilized on an Ultra-flat Au Surface, *Nanoscale Res. Lett.*, 2017, **12**, 0–5.

- 34 P. J. Cameron, X. Zhong and W. Knoll, Electrochemically controlled surface plasmon enhanced fluorescence response of surface immobilized CdZnSe quantum dots, *J. Phys. Chem. C*, 2009, **113**, 6003–6008.
- 35 A. Ulman, Formation and structure of self-assembled monolayers, *Chem. Rev.*, 1996, **96**, 1533–1554.
- 36 P. Pentayya, R. Anumasula, S. Patil, V. Pandey, C. Kumar and S. Chitturi, Spontaneous oscillations and modal resonance in Indian grid: A case study, 2014 18th Natl. Power Syst. Conf. NPSC 2014, 2015, **7463**, 6485–6490.
- 37 P. Yáñez-Sedeño, S. Campuzano and J. M. Pingarrón, Integrated affinity biosensing platforms on screen-printed electrodes electrografted with diazonium salts, *Sensors (Switzerland)*, 2018, **8**, 12-19.
- 38 N. L. Henry and D. F. Hayes, Cancer biomarkers 5, *Mol. Oncol.*, 2012, **6**, 140–146.
- 39 K. Strimbu and J. A. Tavel, What are biomarkers?, *Curr. Opin. HIV AIDS*, 2010, **5**, 463–466.
- 40 M. R. Cowie, P. Jourdain, A. Maisel, U. Dahlstrom, F. Follath, R. Isnard, A. Luchner, T. McDonagh, J. Mair, M. Nieminen and G. Francis, Clinical applications of B-type natriuretic peptide (BNP) testing, *Eur. Heart J.*, 2003, **24**, 1710–1718.
- 41 P. Garg, P. Morris, A. L. Fazlanie, S. Vijayan, B. Dancso, A. G. Dastidar, S. Plein, C. Mueller and P. Haaf, Cardiac biomarkers of acute coronary syndrome: from history to high-sensitivity cardiac troponin, *Intern. Emerg. Med.*, 2017, **12**, 147–155.
- 42 S. Anwaruddin, J. L. Januzzi, A. L. Baggish, E. L. Lewandrowski and K. B. Lewandrowski, Ischemia-modified albumin improves the usefulness of standard cardiac biomarkers for the diagnosis of myocardial ischemia in the emergency department setting, *Am. J. Clin. Pathol.*, 2005, **123**, 140–145.
- 43 W. Hochholzer, D. A. Morrow and R. P. Giugliano, Novel biomarkers in cardiovascular disease: Update 2010, *Am. Heart J.*, 2010, **160**, 583–594.
- 44 P. Glasziou, D. Ph and U. Kingdom, The Role of BNP Testing in Heart Failure.
- 45 M. Weber and C. Hamm, Role of B-type natriuretic peptide (BNP) and NT-PROBNP in clinical routine, *Heart*, 2006, **92**, 843–849.

- 46 M. Horii, T. Matsumoto, S. Uemura, Y. Sugawara, A. Takitsume, T. Ueda, H. Nakagawa, T. Nishida, T. Soeda, S. Okayama, S. Somekawa, K. Ishigami, Y. Takeda, H. Kawata, R. Kawakami and Y. Saito, Prognostic value of B-type natriuretic peptide and its amino-terminal proBNP fragment for cardiovascular events with stratification by renal function, *J. Cardiol.*, 2013, **61**, 410–416.
- 47 H. Matsuura, Y. Sato, O. Niwa and F. Mizutani, Electrochemical Enzyme Immunoassay of a Peptide Hormone at Picomolar Levels with a 10 ng L<sup>-1</sup> level detection limit was developed for important marker for the diagnosis of heart failure ., 2005, **77**, 4235–4240.
- 48 Y. Wahyuni, R. Nurmalasari, S. Gaffar and T. Subroto, B-Type Natriuretic Peptide ( BNP ) Detection Using Electrochemical Immunosensor Based On Sandwich ELISA With Horseradish Peroxidase-Tetramethylbenzidine System, *Procedia Technol.*, 2017, **27**, 149–150.
- 49 C. Y. Lin and D. F. Tai, Detection of oxytocin , atrial natriuretic peptide , and brain natriuretic peptide using novel imprinted polymers produced with amphiphilic monomers, 2019,**12**, 1–8.
- 50 B. E. Winkler, W. Schuetz, G. Froeba and C. Muth, N-terminal prohormone of brain natriuretic peptide : a useful tool for the detection of acute pulmonary artery embolism in post-surgical patients, *Br. J. Anaesth.*, 2012, **109**, 907–910.
- 51 S. Mariotti, C. Cupini, C. Giani, R. Lari, E. Rolled, A. Falco, M. Marchisio and A. Pinchera, Evaluation of a solid-phase immunoradiometric assay (IRMA) for serum thyroglobulin: effect of anti-thyroglobulin autoantibody, *Clin. Chim. Acta*, 1982, **123**, 347–355.
- 52 A. Fallis, *The Immunoradiometric Assay and related Techniques* , *J. Chem. Inf. Model.*, 2013, **53**, 1689–1699.
- 53 W. Al-sheikh, A. V. Heal, K. C. Pefkaros, I. L. Pina, A. N. Serafini, I. H. Ihmedian and F. S. Ashkar, Evaluation of an immunoradiometric assay specific for the CK-MB isoenzyme for detection of acute myocardial infarction, *Am. J. Cardiol.*, 1984, **54**, 269–273.
- 54 A. Breitbart, G. M. Scharf, D. Duncker, C. Widera, J. Gottlieb, A. Vogel, S. Schmidt, G. Brandes, H. G. Heuft, R. Lichtinghagen, T. Kempf, K. C. Wollert, J. Bauersachs and J. Heineke, Highly specific detection of myostatin prodomain by an immunoradiometric sandwich assay in serum of healthy individuals and patients, *PLoS One*, 2013, **8**, 1–10.

- 55 W. L. Hutchinson, W. Koenig, M. Fröhlich, M. Sund, G. D. O. Lowe and M. B. Pepys, Immunoradiometric assay of circulating C-reactive protein: Age-related values in the adult general population, *Clin. Chem.*, 2000, **46**, 934–938.
- 56 J. Wang, Electrochemical biosensors: Towards point-of-care cancer diagnostics, *Biosens. Bioelectron.*, 2006, **21**, 1887–1892.
- 57 N. Bhalla, P. Jolly, N. Formisano and P. Estrela, Introduction to biosensors, 2016, 1–8.
- 58 V. Fragkou, Improvements in electrochemical glucose biosensors, *Chem. Rev.*, 2010, **108**, 814–825.
- 59 D. Thevenot, K. Toth, R. Durst, G. Wilson, D. Thevenot, K. Toth, R. Durst and G. Wilson, Electrochemical biosensors : Recommended definitions and classification ( Technical Report), 2001, **16**, 121-131.
- 60 K. Michael, Biosensors : New approaches in drug discovery Biosensors : new approaches in drug discovery, 2002, **89**, 433-44.
- 61 M. S. Cosio, M. Scampicchio and S. Benedetti, Electronic Noses and Tongues, *Chem. Anal. Food Tech. Appl.*, 2012, 219–247.
- 62 N. Jaffrezic-Renault and S. V. Dzyadevych, Conductometric microbiosensors for environmental monitoring, *Sensors*, 2008, **8**, 2569–2588.
- 63 J. X. J. Zhang and K. Hoshino, Electrical Transducers, *Mol. Sensors Nanodevices*, 2014, **8**, 169–232.
- 64 K. R. Rogers, Biosensors for environmental applications, *Biosens. Bioelectron.*, 1995, **10**, 533–541.
- 65 O. Domínguez-Renedo, M. A. Alonso-Lomillo, L. Ferreira-Gonçalves and M. J. Arcos-Martínez, Development of urease based amperometric biosensors for the inhibitive determination of Hg (II), *Talanta*, 2009, **79**, 1306–1310.
- 66 B. Pérez-López and A. Merkoçi, Nanomaterials based biosensors for food analysis applications, *Trends Food Sci. Technol.*, 2011, **22**, 625–639.
- 67 R. Antiochia, I. Lavagnini and F. Magno, Amperometric mediated carbon nanotube paste biosensor for fructose determination, *Anal. Lett.*, 2004, **37**, 1657–1669.

- 68 S. Myung, A. Solanki, C. Kim, J. Park, K. S. Kim and K. B. Lee, Graphene-encapsulated nanoparticle-based biosensor for the selective detection of cancer biomarkers, *Adv. Mater.*, 2011, **23**, 2221–2225.
- 69 C. Reinemann and B. Strehlitz, Aptamer-modified nanoparticles and their use in cancer diagnostics and treatment, 2014, 1–12.
- 70 S. Tombelli, M. Minunni and M. Mascini, Analytical applications of aptamers, 2005, **20**, 2424–2434.
- 71 A. Chen and S. Yang, Author 's Accepted Manuscript Replacing Antibodies With Aptamers In Lateral Flow Immunoassay Reference :, *Biosens. Bioelectron.*, 2017, **10**,1-50.
- 72 L. Zhao, Y. Huang, Y. Dong, X. Han, S. Wang and X. Liang, Aptamers and Aptasensors for Highly Specific Recognition and Sensitive Detection of Marine Biotoxins: Recent Advances and Perspectives, *Toxins (Basel)*., DOI:10.3390/toxins10110427.
- 73 S. G. Meirinho, L. G. Dias, A. M. Peres and L. R. Rodrigues, Development of an Electrochemical Aptasensor for the Detection of Human Osteopontin, *Procedia Eng.*, 2014, **87**, 316–319.
- 74 S. Ranjbar and S. Shahrokhian, PT CR, *Bioelectrochemistry*, 2018, **5**,12-15.
- 75 B. Applications, L. Wen, L. Qiu, Y. Wu, X. Hu and X. Zhang, Aptamer-Modified Semiconductor Quantum Dots for,2017, **17**,1-14.
- 76 J. G. Bruno, A. M. Richarte and T. Phillips, Preliminary development of a DNA aptamer-magnetic bead capture electrochemiluminescence sandwich assay for brain natriuretic peptide, *Microchem. J.*, 2014, **115**, 32–38.
- 77 M. Negahdary, M. Behjati-ardakani, N. Sattarahmady, H. Yadegari and H. Heli, Sensors and Actuators B: Chemical Electrochemical aptasensing of human cardiac troponin I based on an array of gold nanodumbbells-Applied to early detection of myocardial infarction, *Sensors Actuators B. Chem.*, 2017, **252**, 62–71.
- 78 M. Patil, F. Umanzor, R. Kormos and P. N. Kumta, Platinum aptasensor wire arrays for cardiac biomarker detection, *Mater. Today Commun.*, 2018, **15**, 55–60.
- 79 B. A. Groenning, J. C. Nilsson, L. Sondergaard, F. Pedersen, M. Baumann, H. B. W. Larsson, P. R. Hildebrandt and D. Frederiksberg, Detection of left ventricular

enlargement and impaired systolic function with plasma N-terminal pro brain natriuretic peptide concentrations, DOI:10.1067/mhj.2002.122168.

80 S. Narioka, H. Ishii, D. Yoshimura, M. Sei, Y. Ouchi and K. Seki, The electronic structure and energy level alignment of porphyrin / metal interfaces studied by ultraviolet photoelectron spectroscopy The electronic structure and energy level alignment of porphyrin / metal interfaces studied by ultraviolet photoelectron, 2012, **1899**, 1–4.

81 R. Wegh, H. Donker, A. Meijerink, R. Lamminmäki and J. Hölsä, Vacuum-ultraviolet spectroscopy and quantum cutting for, *Phys. Rev. B - Condens. Matter Mater. Phys.*, 1997, **56**, 13841–13848.

82 B. Roig, C. Gonzalez and O. Thomas, Monitoring of phenol photodegradation by ultraviolet spectroscopy, *Spectrochim. Acta - Part A Mol. Biomol. Spectrosc.*, 2003, **59**, 303–307.

83 B. DanekM, Jensen KF, Murray CB, DanekM, Jensen KF, Murray CB, BawendiMG Synthesis of luminescent thin-film CdSe/ ZnSe quantum dot composites using CdSe quantum dots passivated with an overlayer of ZnSe., *Chem. Mater.*, 1996, **8**, 173–180.

84 K. J. Hamam and M. I. Alomari, A study of the optical band gap of zinc phthalocyanine nanoparticles using UV–Vis spectroscopy and DFT function, *Appl. Nanosci.*, 2017, **7**, 261–268.

85 F. Huang, B. Schulkin, H. Altan, J. F. Federici, D. Gary, R. Barat, D. Zimdars, M. Chen and D. B. Tanner, Terahertz study of 1,3,5-trinitro-s-triazine by time-domain and Fourier transform infrared spectroscopy, *Appl. Phys. Lett.*, 2004, **85**, 5535–5537.

86 D. Ami, R. Posterl, P. Mereghetti, D. Porro, S. M. Doglia and P. Branduardi, Fourier transform infrared spectroscopy as a method to study lipid accumulation in oleaginous yeasts, *Biotechnol. Biofuels*, 2014, **7**, 1–14.

87 T. Nicolet and C. All, *Introduction to Fourier Transform Infrared Spectrometry*, 2001, **199**, 1–8.

88 I. M. A. Viegas, B. S. Santos, A. Fontes, G. A. De Lima Pereira and C. F. Pereira, Multivariate optimization of optical properties of CdSe quantum dots obtained by a facile one-pot aqueous synthesis, *Inorg. Chem. Front.*, 2019, **6**, 1350–1360.

- 89 P. S. Kapatkar, R. B. Shettar, S. B. Kapatkar and N. R. Patil, Synthesis, Structural and Optical Investigation of CdSe semiconductor Quantum Dots, IOP Conf. Ser. Mater. Sci. Eng., 2018, **360**, 1-7.
- 90 A. A. Bunaciu, E. gabriela Udriștioiu and H. Y. Aboul-Enein, X-Ray Diffraction: Instrumentation and Applications, Crit. Rev. Anal. Chem., 2015, **45**, 289–299.
- 91 A. Pradeep, P. Priyadharsini and G. Chandrasekaran, Sol- gel route of synthesis of nanoparticles of  $\text{MgFe}_2\text{O}_4$  and XRD, FTIR and VSM study, J. Magn. Mater., 2008, **320**, 2774–2779.
- 92 A. V. Vorontsov and S. V. Tsybulya, Influence of Nanoparticles Size on XRD Patterns for Small Monodisperse Nanoparticles of CuO and  $\text{TiO}_2$  Anatase, Ind. Eng. Chem. Res., 2018, **57**, 2526–2536.
- 93 H. Toraya, Introduction to X-ray analysis using the diffraction method, Rigaku J., 2016, **32**, 35–43.
- 94 H. Jiang, X. Yao, J. Che, M. Wang and F. Kong, Preparation of ZnSe quantum dots embedded in  $\text{SiO}_2$  thin films by sol-gel process, Ceram. Int., 2004, **30**, 1685–1689.
- 95 H. D. T. Mertens and D. I. Svergun, Structural characterization of proteins and complexes using small-angle X-ray solution scattering, J. Struct. Biol., 2010, **172**, 128–141.
- 96 E. Mylonas and M. V Petoukhov, Structural characterization of flexible proteins using SAXS, J. Am. Chem. Soc., 2007, 5656–5664.
- 97 B. Champagnon, B. Andrianasolo, A. Ramos, M. Gandais, M. Allais and J. P. Benoit, Size of Cd(S,Se) quantum dots in glasses: Correlation between measurements by high-resolution transmission electron microscopy, small-angle x-ray scattering, and low-frequency inelastic Raman scattering, J. Appl. Phys., 1993, **73**, 2775–2780.
- 98 G. C. Capitani and M. Mellini, High-resolution transmission electron microscopy (HRTEM) investigation of antigorite polysomes ( $m = 15$  to 18), Am. Mineral., 2007, **92**, 64–71.
- 99 P. B. Malla and S. Komameni, High-Resolution Transmission Electron Microscopy (HRTEM) in the Study of Clays and Soils, 1990, 159–186.

- 100 J. Lim, S. Jun, E. Jang, H. Baik, H. Kim and J. Cho, Preparation of highly luminescent nanocrystals and their application to light-emitting diodes, *Adv. Mater.*, 2007, **19**, 1927–1932.
- 101 X. Li, H. Wang, Y. Shimizu, A. Pyatenko and K. Kawaguchi, Preparation of carbon quantum dots with tunable photoluminescence by rapid laser passivation in ordinary organic solvents Preparation of carbon quantum dots with tunable photoluminescence by rapid laser passivation in ordinary organic solvents, 2010,**9**, 1–3.
- 102 M. Nocuń and S. Kwaśny, Preparation and characterization of V<sub>2</sub>O<sub>5</sub> doped SiO<sub>2</sub>-TiO<sub>2</sub> thin films, *Cent. Eur. J. Eng.*, 2012, **2**, 123–128.
- 103 A. H. Memon and I. A. Rahman, SEM-PLS analysis of inhibiting factors of cost performance for large construction projects in malaysia: Perspective of clients and consultants, *Sci. World J.*,2014,**6**,1-10.
- 104 S. K. Sharma, D. S. Verma, L. U. Khan, S. Kumar and S. B. Khan, *Handbook of Materials Characterization*, 2018, vol. 2.
- 105 V. A. Ermakov, J. Maria, S. Filho, L. G. Bonato, N. Vishnu, V. Mogili, F. E. Montoro, F. Iikawa, A. F. Nogueira, C. L. Cesar, E. Jime and F. C. Marques, Three-Dimensional Superlattice of PbS Quantum Dots in Flakes,2018, **3**, 2027-2032.
- 106 D. V. Heyd and D. A. Harrington, Platinum oxide growth kinetics for cyclic voltammetry, *J. Electroanal. Chem.*, 1992, **335**, 19–31.
- 107 R. S. Nicholson, Theory and Application of Cyclic Voltammetry for Measurement of Electrode Reaction Kinetics, *Anal. Chem.*, 1965, **37**, 1351–1355.
- 108 D. E. Richardson and H. Taube, Determination of E<sub>2</sub>' - E<sub>1</sub>' in Multistep Charge Transfer by Stationary-Electrode Pulse and Cyclic Voltammetry: Application to Binuclear Ruthenium Ammines, *Inorg. Chem. Front.*, 1981, **20**, 1278–1285.
- 109 J. F. Rusling and S. L. Suib, Characterizing Materials with Cyclic Voltammetry, *Adv. Mater.*, 1994, **6**, 922–930.
- 110 H. Freund and V. B. B. Bergbau-, Homogenous Redox Catalysis Of Electrochemical Reactions, *J. Electroanal. Chem.*, 1980, **45**, 721–737.
- 111 A. Manuscript, Nanoscale, DOI:10.1039/C8NR02278J.

- 112 A. S. Afonso, B. Pérez-López, R. C. Faria, L. H. C. Mattoso, M. Hernández-Herrero, A. X. Roig-Sagués, M. Maltez-da Costa and A. Merkoçi, Electrochemical detection of Salmonella using gold nanoparticles, *Biosens. Bioelectron.*, 2013, **40**, 121–126.
- 113 K. Scott, *Electrochemical Principles and Characterization of Bioelectrochemical Systems*, Elsevier Ltd., 2016.
- 114 R. S. Rodgers, An introduction to electrochemical impedance spectroscopy (EIS), 2009, **8**, 1–46.
- 115 J. Halliwell, A. C. Savage, N. Buckley and C. Gwenin, Electrochemical impedance spectroscopy biosensor for detection of active botulinum neurotoxin, *Sens. Bio-Sensing Res.*, 2014, **2**, 12–15.
- 116 T. Tsai, S. Wang and S. Chen, Electrodeposited indigotetrasulfonate film onto glutaraldehyde-cross-linked poly- L -lysine modified glassy carbon electrode for detection of dissolved oxygen, *J. Electroanal. Chem.*, 2011, **659**, 69–75.
- 117 W. J. Van Ooij and D. Zhu, Electrochemical impedance spectroscopy of bis-[triethoxysilypropyl] tetrasulfide on Al 2024-T3 substrates, *Corrosion*, 2001, **57**, 413–427.
- 118 F. Shahdost-fard and M. Roushani, An impedimetric aptasensor based on water soluble cadmium telluride (CdTe) quantum dots (QDs) for detection of ibuprofen, *JEAC*, 2016, **763**, 18–24.

## 3 CHAPTER 3: Experimental

### Summary

*This chapter describes the synthesis procedure for the mercaptosuccinic acid capped nickel selenide quantum dots. Included as well are the aptasensor fabrication and the sample preparation for all characterization techniques. In addition, all the chemicals used and the instrumentation models employed throughout this study are outlined.*

### 3.1 Reagents

Analytical grade nickel chloride hexahydrate (99%), selenium powder (99%), mercaptosuccinic acid (MSA) (98%), sodium borohydride (98%), sodium hydroxide (98%), 1-ethyl-3-(3-dimethylaminopropyl) carbodiimide hydrochloride (EDC), N-hydroxysuccinimide (NHS) (98%), cysteamine (98%), 10 mM phosphate buffered saline (PBS) pH 7.4, human brain natriuretic peptide (BNP), 98% mercaptohexanol (MCH), tris-EDTA buffer pH 8.0, 37 % hydrochloric acid (HCl), ferricyanide ( $[\text{Fe}(\text{CN})_6]^{3-}$ ), sodium nitrate ( $\text{NaNO}_2$ ), 4-nitroaniline and potassium chloride (KCl) were all purchased from Sigma Aldrich. Amino modified aptamer  $\text{NH}_2$ -TTTTTTGGCGATTCGTGATCTCTGCTCTCGGTTTCGTTCG was purchased from Ingaba Biotech, South Africa. The distilled water used for preparing solutions and cleaning electrodes was purified using a Milli-Q water system that was purchased from (Millipore Corp, Bedford, MA, USA).

### 3.2 Instrumentation

All alumina powders (0.05, 0.3 and 1.0  $\mu\text{m}$ ) and polishing pads used to clean electrodes were purchased from Buehler (Illinois, USA). All electrochemical measurements were carried out using a CHI electrochemical workstation from Bioanalytical systems (Lafayette, USA) and palm sense 3 from Metrohm SA (Pty) Ltd (Firgrove, Cape-Town, South Africa). Ultraviolet-Visible spectroscopy measurements were carried out using a GBC UV-Vis 920 instrument from Thermo Electron Corporation (Warwickshire, United Kingdom). Fourier Transform Infrared Spectroscopy measurements were carried out using PERKIN ELEM SPECTRUM TWO FTIR spectrometer from PerkinElmer

(Midrand, South Africa). All X-ray Diffraction measurements were carried out using a BRUKER AXS DS ADVANCE diffractometer with  $2\theta$  values ranging from 20-90° with a step size of 0.0028° operating at 45 kV and 40 mA from Bruker AXS (Germany). High resolution transmission electron microscopy measurements were carried out using a TECNAI G2 F20 X-TWIN MAT 200 kV field emission from FEI (Eindhoven, Netherlands). High Resolution Scanning Microscopy measurements were carried out using ZEISS ULTRA scanning microscope with an acceleration voltage of 5.0 kV from FEI (Eindhoven, Netherlands). All Small Angle X-ray Scattering measurements were carried out using a SAXSpace Anton Paar instrument from Anton Paar (North Ryde, Australia).

### **3.3 Procedure**

#### **3.3.1 Synthesis of MSA capped NiSe-QDs**

The synthesis of mercaptosuccinic acid capped nickel selenide quantum dots (MSA-NiSe<sub>2</sub> QDs) was prepared by methods described by Wang and Co-workers, with some modifications.

##### **3.3.1.1 Preparation of the sodium hydrogen selenide solution**

60 mg of Selenium powder (Se) and 58 mg of sodium borohydride (NaBH<sub>4</sub>) were combined in the ratio 1:2 in a 100 mL centrifuge tube. The centrifuge was then shaken to mix the powders. 10 mL of distilled was then added to the tube to allow the powders to mix. The mixture then became black in color and bubbles started forming. The lid of the tube was removed and covered with parafilm with small holes inserted to allow the hydrogen gas to escape. The formation of the hydrogen gas is due to the following reaction:



The mixture was then placed in the fridge for 24 hours until a dark orange color was obtained.

### **3.3.1.2 Preparation of the MSA-NiCl<sub>2</sub> ion solution**

200 mg of nickel chloride hexahydrate (NiCl<sub>2</sub>·6H<sub>2</sub>O) and 347 mg of mercaptosuccinic (MSA) was dissolved in 10 mL distilled water. The mixture was allowed to stir for 10 min and after 10 min the solution was green in color. The pH of the solution was then adjusted using sodium hydroxide (NaOH) to pH 9.01. The solution then became dark purple in color. The dark purple solution was then stirred for 30 min under N<sub>2</sub> gas. The ratio of NiCl<sub>2</sub>: Se: MSA was 2:1:3, respectively.

Then 5 mL of the previously prepared NaHSe solution was added to the saturated MSA-NiCl<sub>2</sub> at room temperature. The mixture was then allowed to react for 5 min. Upon the addition of the NaHSe the solution became black in color. After reacting for 5 min the mixture was then placed in the microwave for 45 min at 90°C. After microwave heating the reaction was quenched in the freezer at -20°C.

The MSA-NiSe<sub>2</sub> QDs was then purified in ethanol by adding QDs to ethanol in a ratio of 1:3 and centrifuged for 10 min three times. The supernatant was then discarded and a pellet was obtained. The pellet was then redispersed in distilled water to obtain the purified MSA-NiSe<sub>2</sub> QDs.

## **3.4 Sample preparation**

### **3.4.1 Ultraviolet-visible spectroscopy**

For Ultraviolet-visible spectroscopy (UV-VIS spectroscopy) measurements, two quartz cuvettes known as the reference cell and sample cell were used. The reference cell and the sample cell was cleaned with ethanol and dried with nitrogen gas before use. 2 mL of distilled water which was the solvent in which the quantum dots was dispersed in, was added in both the reference cell and sample cell and scanned as a blank from 200-800 nm. The sample cell was then cleaned with ethanol and dried with nitrogen gas

before use. A certain amount of MSA-NiSe<sub>2</sub> QDs is then diluted with distilled and scanned at a wavelength of 200-800 nm.

### **3.4.2 Fourier Transform Infra-Red Spectroscopy**

A flow cell was used for Fourier transform infra-red spectroscopy (FTIR) measurements. The flow cell was cleaned with ethanol before use. The solvent used to redisperse the MSA-NiSe<sub>2</sub> QDs was distilled water and this solvent was injected into the flow cell and measured as background from 400-4000 cm<sup>-1</sup>. The solvent was then discarded and a small volume of the MSA-NiSe<sub>2</sub> QDs was injected into the flow cell. The flow cell was then scanned from 400-4000 cm<sup>-1</sup> for FTIR measurements.

### **3.4.3 X-Ray Diffraction**

For X-ray diffraction (XRD) measurements the MSA-NiSe<sub>2</sub> QDs was drop coated on a glass substrate to form a thick uniform layer. The thin film is then packed on the sample stage at a random mount and scanned in the 2θ range from 20° to 80° for the identification of the different phases of the sample. A random mount was chosen because it allows the sample on the sample stage to assume different orientations and ensure reflections from various hkl planes.

### **3.4.4 Small Angle X-ray Scattering**

For small angle X-ray scattering (SAXSpace) measurements an aliquot of MSA-NiSe<sub>2</sub> QDs was loaded in a 1mm thin walled quartz capillary and was exposed to the beam at a distance of 305 mm from the detector and temperature controlled at 21°C.

### **3.4.5 High Resolution Transmission Electron Microscopy**

For high resolution transmission electron microscopy, 10 uL of MSA-NiSe<sub>2</sub> QDs was dropped on a copper grid and left to dry under an infra-red bulb for 20 min before HR-TEM measurements.

### 3.4.6 High Resolution Scanning Electron Microscopy

For high resolution scanning electron microscopy measurements, MSA-NiSe<sub>2</sub> QDs were immobilized on a SPCE and left to dry before analyses. An extra SPCE consisting of MSA-NiSe<sub>2</sub> QDs immobilized with an amine aptamer was analyzed as well. The MSA-NiSe<sub>2</sub> QDs modified SPCE was stored in the dark at room temperature, while the aptamer-MSA-NiSe<sub>2</sub> QDs modified SPCE was stored at 4°C.

### 3.4.7 Cyclic voltammetry

#### 3.4.7.1 Preparation of MSA-NiSe<sub>2</sub> QDs on conventional gold electrodes

The gold electrode (AuE) was thoroughly polished and cleaned using 1.00, 0.30 and 0.05 μM alumina slurries on separate polishing pads for 10 min each. It was then ultrasonicated for 10 min with ethanol and then with water to remove any adsorbed alumina crystals on the AuE surface. After ultrasonication the AuE electrode was rinsed with distilled water and ready for use. First the electrode was cleaned electrochemically with sulphuric acid to determine the surface roughness factor (Rf) of the AuE given by Equation [3.2]:

$$Rf = \frac{\text{Charge passed (Ah)}}{\text{Charge associated with Au } (\mu\text{Cm}^{-2}) \times \text{Geometric area of electrode (cm}^2\text{)}} \quad 3.1$$

Then 20 uL of cysteamine was drop coated on the AuE surface and left to dry in a dark space for 12 hrs. The AuE was then rinsed carefully with distilled water to remove unbound cysteamine. Then 10 uL of 1-ethyl-3-(3-dimethylaminopropyl) carbodiimide hydrochloride and N-hydroxysuccinimide (EDC/NHS) with a ratio of 1:3 was drop coated on the AuE surface and left on the surface for 30 min. The EDC/NHS served to activate the carboxyl groups on the MSA-NiSe<sub>2</sub> QDs. Then 5 uL of the MSA-NiSe<sub>2</sub> QDs was drop coated on the AuE surface and left to dry for 24 hrs before electrochemical characterization.

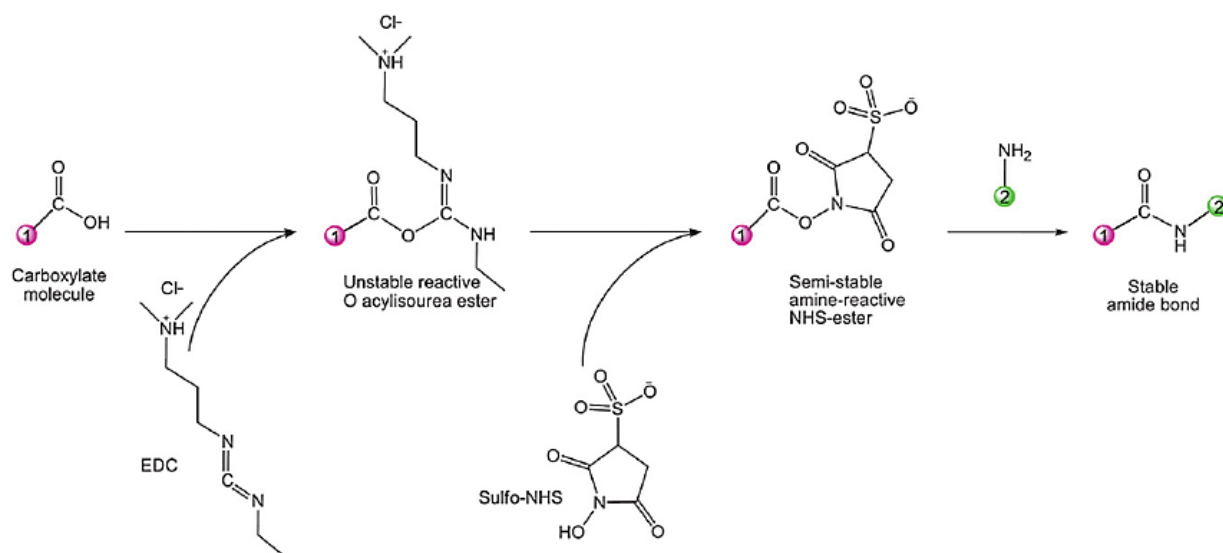


**Figure 3.1:** EDC/NHS chemistry. Reprinted from J. Bart, R. Tiggelaar, M. Yang, S. Schlautmann, H. Zuilhof and H. Gardeniers, Room-temperature intermediate layer bonding for microfluidic devices, *Lab Chip*, 2009, **9**, 3481–3488.

### 3.4.7.2 Preparation of MSA-NiSe<sub>2</sub> QDs on screen printed gold electrodes

The immobilization of MSA-NiSe<sub>2</sub> QDs was on screen printed gold electrodes (SPGE) followed a similar procedure to the conventional AuE.

### 3.4.7.3 Preparation of MSA-NiSe<sub>2</sub> QDs on conventional glassy carbon electrodes

The glassy carbon electrode (GCE) was thoroughly polished and cleaned using 1.00, 0.30 and 0.05  $\mu\text{M}$  alumina slurries on separate polishing pads for 10 min each. It was then ultrasonicated for 10 min with ethanol and then with water to remove any adsorbed alumina crystals on the GCE surface. After ultrasonication the GCE electrode was rinsed with distilled water and ready for use.

For immobilization of the MSA-NiSe<sub>2</sub> QDs on the GCE, electrografting of 4-nitrophenyl to 4-aminophenyl was done in the following way.

For electrografting of 4-nitrophenyl layers, 400  $\mu\text{L}$  of 0.1 M  $\text{NaNO}_2$  is added to 20 mL of a solution containing 1 mM 4-nitroaniline and 0.5 M HCl under stirring at room temperature. The mixture was allowed to react for 5 min before dropping 10  $\mu\text{L}$  on GCE that is connected to a palm sense electrochemical work station. Electrochemical modification of the GCE surface is performed by 2 cycles of CV scanned from +0.7 V to -0.4 V, at a scan rate of 0.05 V/s and rinsed with distilled water.

For electrochemical reduction of 4-nitrophenyl to 4-aminophenyl, still connected to the palm sense, 10  $\mu\text{L}$  of 1.0 M KCl was dropped on the GCE surface. Electrochemical reduction was then performed by 5 cycles of CV scanned from 0.4 V to -1.2 V, at a scan rate of 0.05 V/s and rinsed with distilled water in readiness for electro-analytical characterization. Then 10  $\mu\text{L}$  of MSA-NiSe<sub>2</sub> QDs in a solution of EDC/NHS in a ratio of 1:3 was drop coated on the GCE, and left for 24 hrs before use. The electrografting process was repeated for screen printed carbon electrodes (SPCE)

#### **3.4.7.4 Preparation of MSA-NiSe<sub>2</sub> QDs on screen printed carbon electrodes.**

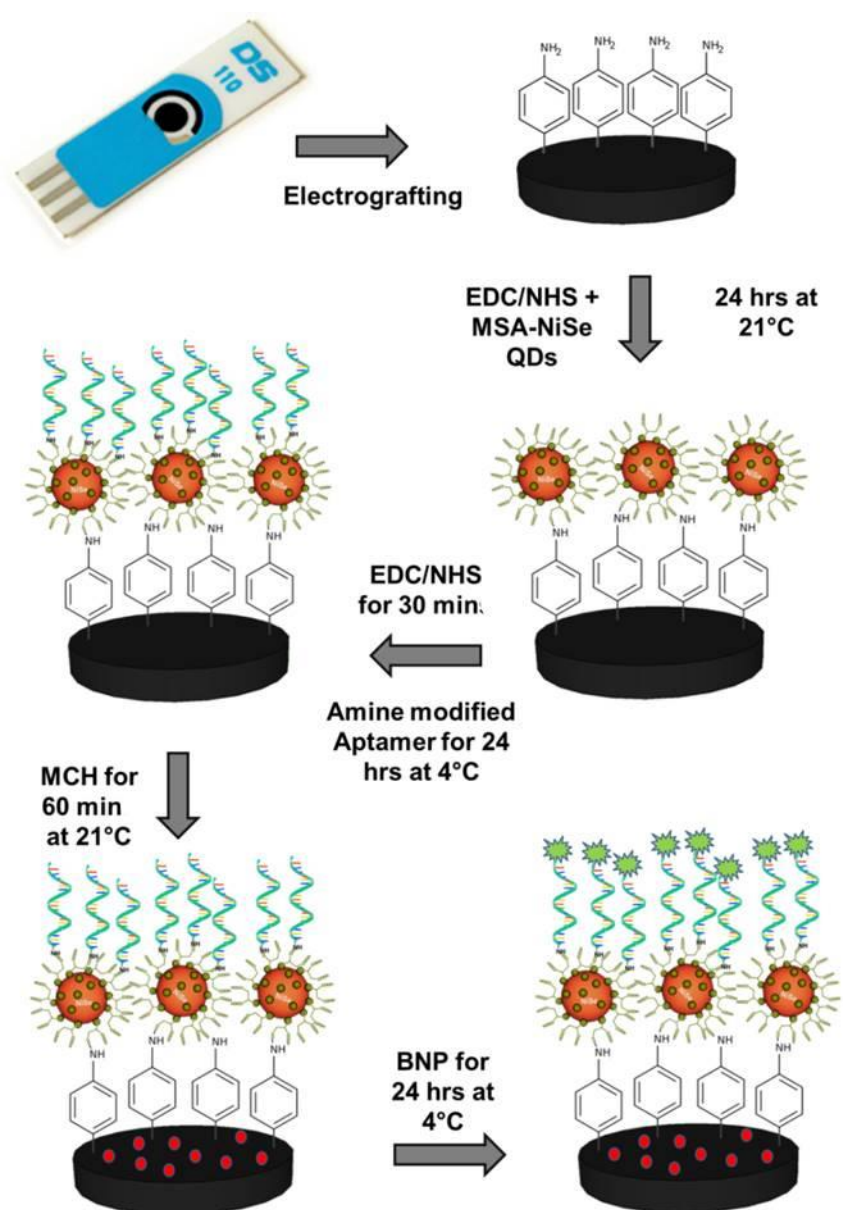
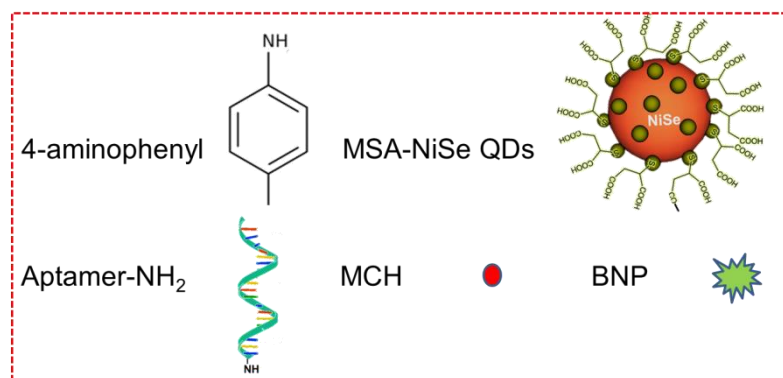
The immobilization of the MSA-NiSe<sub>2</sub> QDs on screen printed carbon electrodes (SPCE) followed the same electrografting procedure as conventional glassy carbon electrodes.

### **3.5 Fabrication of the MSA-NiSe<sub>2</sub> QDs dots aptasensor**

For fabrication of the MSA-NiSe<sub>2</sub> QDs aptasensor, bare screen printed carbon electrodes (SPCE) were screened in ferricyanide from -0.4 V to 0.5 V, at a scan rate of 50 mV/s for 1 cycle. Electrografting of the MSA-NiSe<sub>2</sub> QDs on the SPCE electrode then took place.

After electrografting, 50  $\mu\text{L}$  of MSA-NiSe<sub>2</sub> QDs was added to a 1:3 ratio of ethyl-3-(3-dimethylaminopropyl) carbodiimide hydrochloride and N-hydroxysuccinimide (EDC/NHS) solution. The mixture was allowed to react for 30 min before being drop coated on the SPCE and left to dry for 24 hrs at 21°C; this was to activate the carboxyl

groups of the MSA-NiSe<sub>2</sub> QDs enabling it to bind with the amine groups from the electrographing process on the SPCE. The MSA-NiSe<sub>2</sub> QDs SPCE was then rinsed with 10 mM PBS and left to dry for 5 min. Then 50 uL of EDC/NHS was drop coated on the SPCE surface again for 30 min to activate the carboxyl groups of the MSA-NiSe<sub>2</sub> QDs for binding with amine modified aptamer. Thereafter, the SPCE-MSA-NiSe<sub>2</sub> QDs surface was rinsed with 10 mM PBS and 50 uL of 3 μM aptamer was drop coated on the activated SPCE-MSA-NiSe<sub>2</sub> QDs surface and incubated for 24 hrs, at 4°C. The APT/MSA-NiSe<sub>2</sub>QDs/SPCE was then rinsed with 10 mM PBS, and thereafter 50 uL of 1 mM mercaptohexanol (MCH) was drop coated on the APT/MSA-NiSe<sub>2</sub>QDs/SPCE surface and left for 60 min to prevent non-specific binding. The fabricated aptasensor (MCH/APT/MSA-NiSe<sub>2</sub>QDs/SPCE) was then incubated with different concentrations of brain natriuretic peptide (BNP) for 24 hrs, at 4°C. Thereafter it was ready for detection of BNP. The fabrication process of the aptasensor is illustrated below.



**Scheme 3.1:** Brain natriuretic peptide (BNP) aptasensor fabrication.

### **3.6 Conclusion**

Water soluble mercaptosuccinic acid capped nickel selenide quantum dots was successfully synthesized through an aqueous route assisted by microwave irradiation. Within this chapter the materials used for the synthesis of the MSA-NiSe<sub>2</sub> QDs including the instrumentation used to characterize the MSA-NiSe<sub>2</sub> QDs was outlined. In addition, sample preparations for the different characterization techniques are discussed, as well as the method of fabrication for aptasensor.

## References

- 1 Y. Wang, K. Yang, H. Pan, S. Liu and L. Zhou, Synthesis of high-quality CdSe quantum dots in aqueous solution, *Micro Nano Lett.*, 2012, **7**, 889–891.
- 2 1 S. Bouden, J. Pinson and C. Vautrin-UI, Electrografting of diazonium salts: A kinetics study, *Electrochem. commun.*, 2017, **81**, 120–123.
- 3 1 J. Ghilane, G. Trippe-Allard and J. C. Lacroix, Grafting of imidazolium ion-terminated layer using electrochemical reduction of diazonium: Redox active counter anion exchange within the layer, *Electrochem. commun.*, 2013, **27**, 73–76.
- 4 1 E. Gervais, Y. Aceta, P. Gros and D. Evrard, Study of an AuNPs functionalized electrode using different diazonium salts for the ultra-fast detection of Hg(II) traces in water, *Electrochim. Acta*, 2018, **261**, 346–355.
- 5 1 A. M. Nowicka, M. Fau, A. Kowalczyk, M. Strawski and Z. Stojek, Electrografting of carboxyphenyl thin layer onto gold for DNA and enzyme immobilization, *Electrochim. Acta*, 2014, **126**, 11–18.

## 4 Chapter 4: Results and Discussion

### Summary

*This chapter deals with the characterization of the novel synthesized mercaptosuccinic acid capped nickel selenide quantum dots using spectroscopic and microscopic techniques. In addition, electrochemical analysis of the QDs was also investigated. Furthermore, this chapter discusses the analytical performance of the QDs based aptasensor towards different concentrations of BNP analyte*

### 4.1 Results and discussion

#### 4.1.1 Spectroscopic Techniques

##### 4.1.1.1 Ultraviolet-visible spectroscopy (UV-Vis)

UV-Vis spectroscopy was used to study the optical properties of the mercaptosuccinic acid capped nickel selenide quantum dots (MSA-NiSe<sub>2</sub> QDs) and its precursors namely, mercaptosuccinic acid capped nickel chloride (MSA-NiCl<sub>2</sub>), sodium hydrogen selenide (NaHSe) and mercaptosuccinic acid (MSA). Furthermore, this technique provided information about the excitation peak, direct and indirect bandgap energy and particle size distribution of the MSA-NiSe<sub>2</sub> QDs. The direct and indirect bandgap energy was determined from the absorption spectra of the MSA-NiSe<sub>2</sub> QDs by the Tauc-relation.<sup>1</sup>

$$\alpha h\nu = A(h\nu - E_g)^n \quad 4.1$$

where  $\alpha$  is the absorption coefficient,  $h$  is planks constant,  $\nu$  is the frequency,  $A$  is a constant,  $E_g$  is the bandgap energy where  $n = \frac{1}{2}$  for indirect bandgap energy and  $n=2$  for direct bandgap energy. By plotting  $(\alpha h\nu)^{\frac{1}{2}}$  versus  $h\nu$  and extrapolating the linear region a value for the direct bandgap energy for quantum dots was obtained and by plotting  $(\alpha h\nu)^2$  v.s  $h\nu$  a value for the indirect bandgap energy for the QDs was obtained.<sup>2</sup>

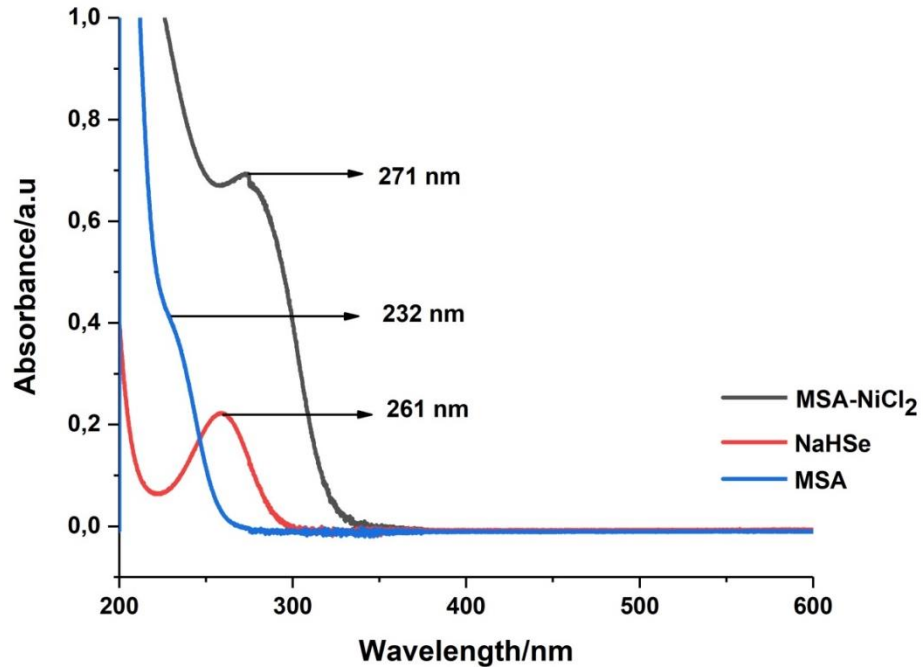


**Figure 4.1:** UV-Vis spectrum of MSA-NiCl<sub>2</sub> (black line), NaHSe (red line) and MSA (blue line).

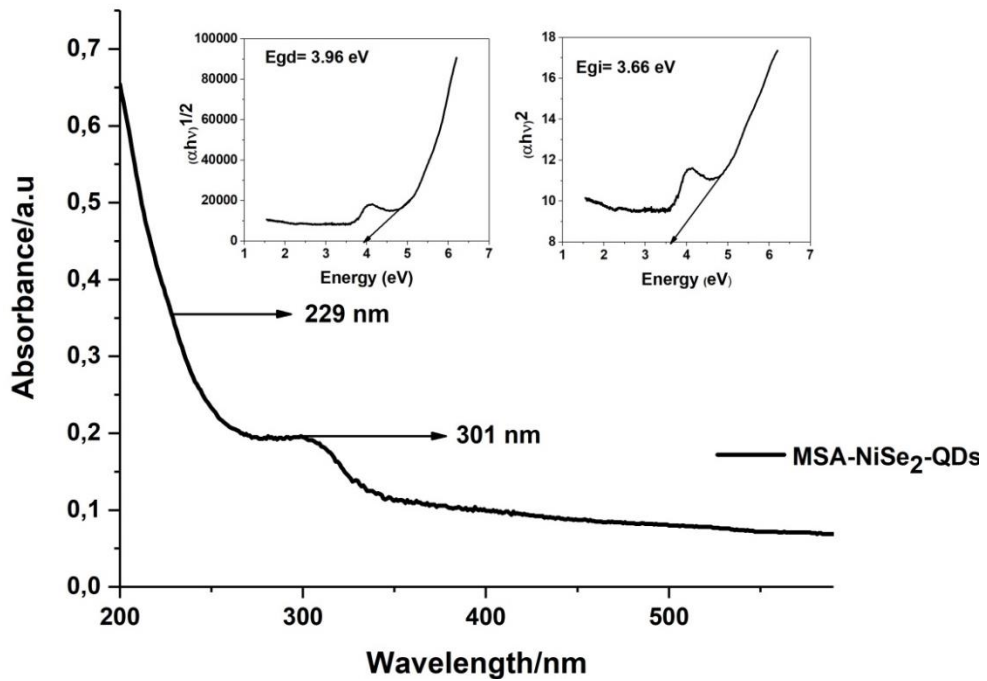


**Figure 4.2:** UV-Vis spectrum of MSA-NiSe<sub>2</sub> QDs. The left inset shows the direct bandgap energy plot, while the right inset shows the indirect bandgap energy plot.

From Figure 4.1, the absorbance spectrum shows one peak for each of the precursors. These peaks are located at 271 nm, 261 nm and 232 nm for MSA-NiCl<sub>2</sub>, NaHSe and MSA, respectively. By studying the absorbance peaks in both Figure 4.1 and Figure 4.2, it can be deduced that the absorbance peak at 229 nm observed in Figure 4.2, could be due to n-σ\* transitions of the sulphur groups of the MSA capping agent as a result of the shifting of the MSA peak from 232 nm in figure 4.1 to 229 nm in figure 4.2. These transitions are an indication that the MSA capping agent successfully capped the NiSe<sub>2</sub>-QDs.<sup>3</sup> The peak at 301 nm in Figure 4.2 is attributed to the absorbance of the QDs. This peak is weak and is an indication that the QDs has a broad size distribution and are polydispersed.<sup>4</sup> The direct and indirect bandgap energy is characteristic to semiconductors. In the direct bandgap energy the transition of electrons and its associated holes from valence band to conduction band has the same momentum value, and in the indirect bandgap energy the transition of electrons and its associated hole from the valence band to the conduction band has a different momentum value.<sup>5</sup> The MSA-NiSe<sub>2</sub> QDs has a direct bandgap energy of 3.96 eV and indirect bandgap energy of 3.66 eV. The direct and indirect bandgap energies are an indication that the MSA-NiSe<sub>2</sub>-QDs are semiconductors due to the fact that the bandgap energies are less than 4 eV, anything greater than 4 eV are considered insulators.<sup>6</sup> The MSA-NiSe<sub>2</sub> QDs appears to be blue shifted from its bulk counterpart (bandgap energy of 2.0 eV and it absorbs at 620 nm), which confirms the nanophase of the MSA-NiSe<sub>2</sub> QDs.<sup>7</sup> The minimum energy associated with the MSA-NiSe<sub>2</sub> QDs as it transitions from the valence band to the conduction band was calculated from Planck's law, given by:

$$\Delta E = h\nu = h\left(\frac{c}{\lambda_{max}}\right) \quad 4.2$$

where E is the bandgap energy, *h* is Planck's constant, *c* is the speed of light and *λ* is the maximum absorbance wavelength.<sup>8</sup> The minimum energy associated with the energy transition from the valence band to the conduction of the MSA-NiSe<sub>2</sub> QDs was estimated to be 6.59 × 10<sup>-19</sup>J. The minimum energy value of 6.59 × 10<sup>-19</sup>J is associated with a bandgap of 3.89 eV which justifies the nanophase of the QDs as explained by Veigas and co-workers which is any value less than 4 eV.<sup>8</sup>

### 4.1.1.2 Fourier transform infrared (FT-IR) Spectroscopy

FT-IR as discussed in chapter 2 was used as an important tool to determine the structure and purity of the QDs. This was done by comparing the FT-IR spectrum of mercaptosuccinic acid (MSA) capping agent and the mercaptosuccinic acid capped nickel selenide quantum dots (MSA-NiSe<sub>2</sub> QDs).

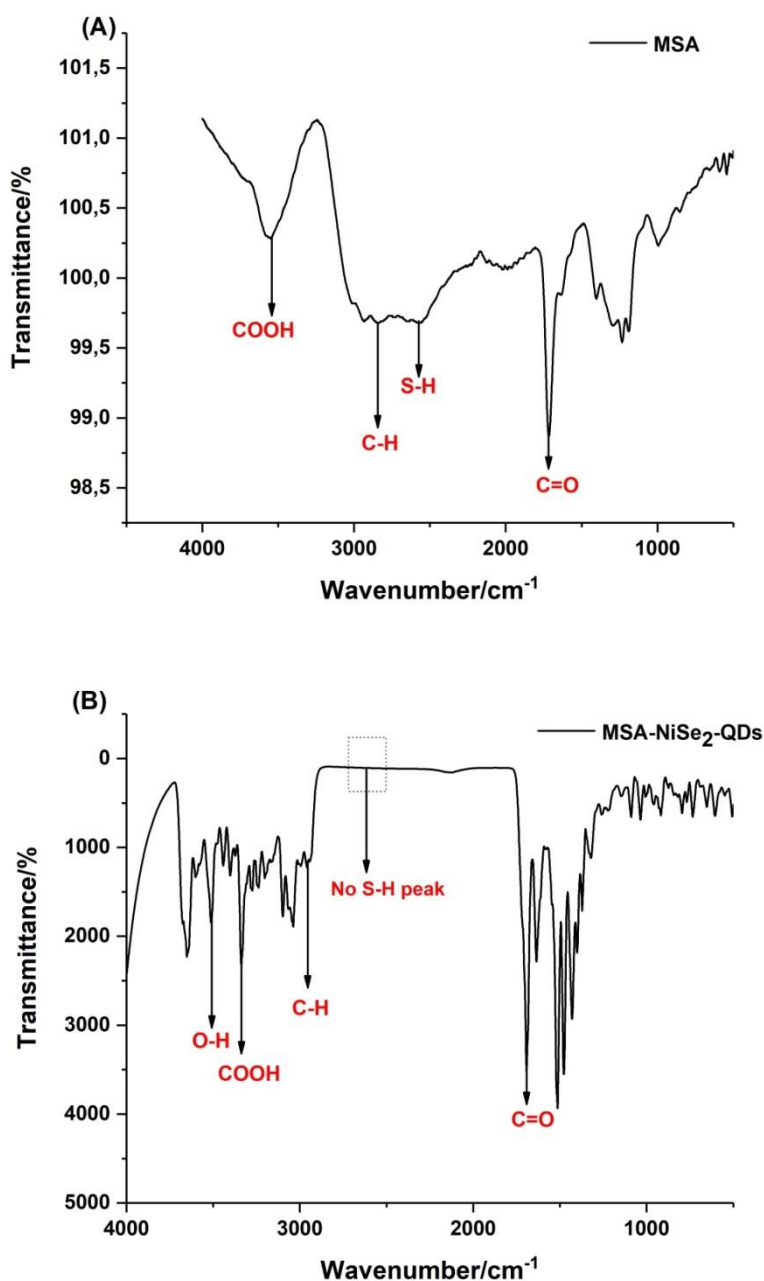
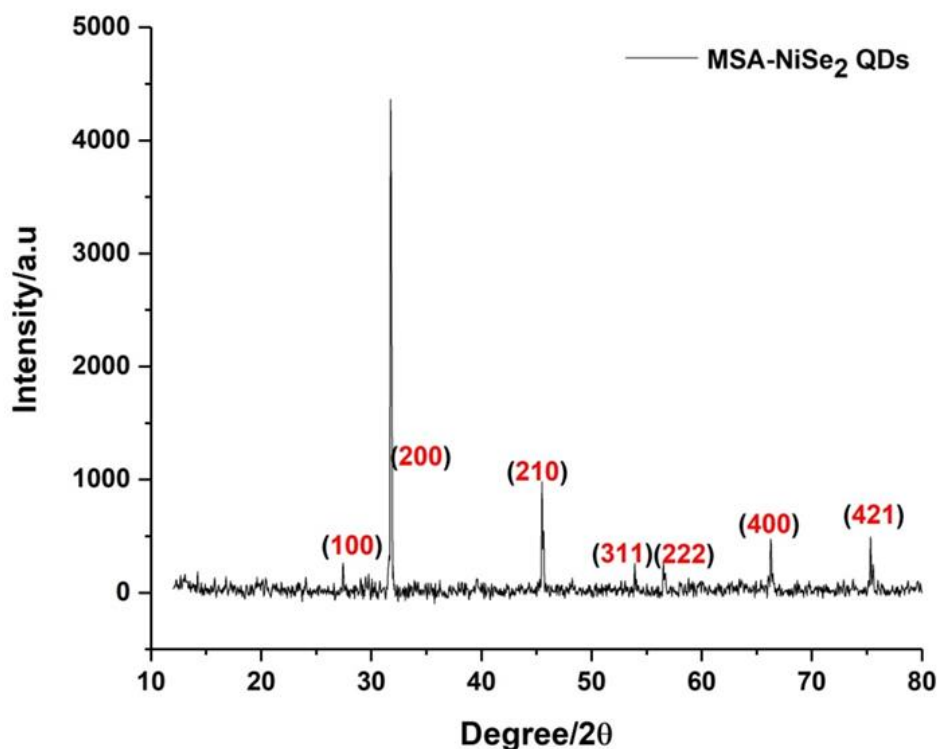


Figure 4.3: FT-IR spectrum of MSA (A) and MSA-NiSe<sub>2</sub> QDs (B).

From Figure 4.3 (A), the spectrum for MSA capping agent shows distinct peaks that are associated with the functional groups present on MSA. A broad peak occurring at  $3485\text{ cm}^{-1}$  is due to the  $-\text{COOH}$  group on the MSA structure. The small peak occurring at  $2852\text{ cm}^{-1}$  is due to the  $-\text{C-H}$  Stretch. The peak occurring at  $2652\text{ cm}^{-1}$  is due to the S-H bond that is characteristic to MSA. There is also a sharp peak at  $1615\text{ cm}^{-1}$  and it is due to the  $\text{C=O}$  stretch of the carboxylic acid group present on MSA.<sup>9</sup> Figure 4.3 (B) shows the FTIR spectrum of MSA-NiSe<sub>2</sub> QDs. Here, a peak at  $3505\text{ cm}^{-1}$  is due to an O-H group that arises from the solvent (in this case H<sub>2</sub>O) used to dissolve the MSA-NiSe<sub>2</sub> QDs, The peak occurring at  $3335\text{ cm}^{-1}$  is due to the COOH group that is characteristic to MSA. The small peak occurring at  $2946\text{ cm}^{-1}$  is due to C-H bend, however, it seems almost non-existent and may be due to hydrogen binding which often overlaps with the C-H bend group.<sup>10</sup> The sharp peak occurring at  $1667\text{ cm}^{-1}$  is due to the  $\text{C=O}$  of the carboxylic acid. The disappearance of the thiol peak at  $2654\text{ cm}^{-1}$  as indicated on the FTIR spectrum confirms that NiSe<sub>2</sub> QDs are in fact capped with MSA.<sup>11</sup>

#### **4.1.1.3 X-ray diffraction (XRD)**

XRD was used to study the phase structure and chemical composition of the mercaptosuccinic capped nickel selenide quantum dots (MSA-NiSe<sub>2</sub> QDs). The scanning angle range,  $2\theta$  of the diffractometer, was from  $10^\circ$  to  $80^\circ$ .



**Figure 4.4:** XRD pattern of MSA-NiSe<sub>2</sub> QDs

Figure 4.4 shows the XRD pattern for the MSA-NiSe<sub>2</sub> QDs which exhibits seven peaks in the  $2\theta$  range = 27.4°, 31.8°, 35.8°, 54.0°, 56.6°, 66.5°, 77.8° which corresponds to the diffractions of the (111), (200), (210), (311), (222), (400), (421) planes, respectively. This is in accordance with the bulk cubic NiSe<sub>2</sub> obtained from the (JCPDS card no: 80-0375). However, traces of unreacted selenium and MSA were also found which could be due to the molar ratios of nickel to selenium to MSA used. This could have led to the polydispersity of the MSA-NiSe<sub>2</sub> QDs.

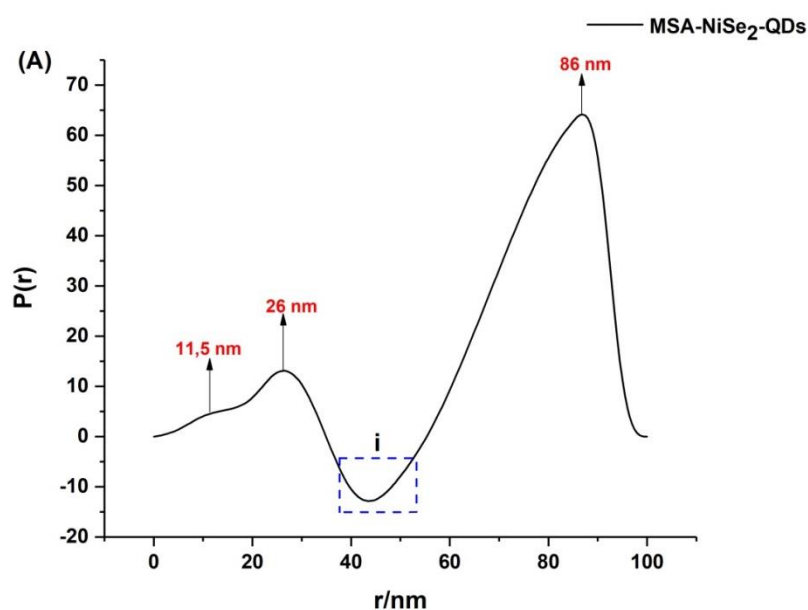
A rough estimate of the quantum dot crystal size can be calculated using the Scherrer formula as seen in Equation 4.3 below. Here, the most intense peak in the XRD spectrum is used, in this case, the (200) plane.<sup>12</sup>

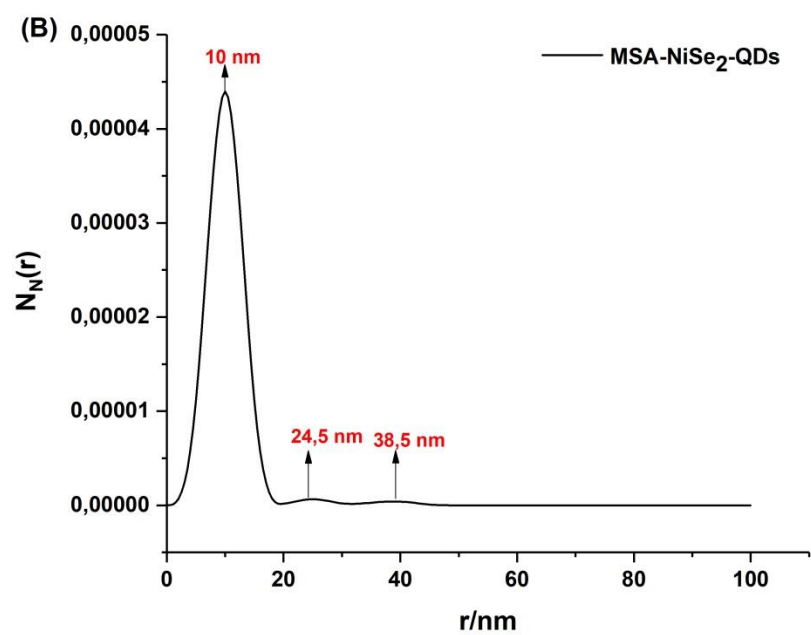
$$D = \frac{K\lambda}{\beta \cos\theta} \quad 4.3$$

where  $D$  corresponds to the average crystal size (nm),  $k$  is the Scherrer constant,  $\beta$  is the full-width-at-halves-maximum (FWHM),  $\lambda$  is the wavelength of the X-ray (nm) and  $\theta$  is the peak position (radians). The estimated size of the MSA-NiSe<sub>2</sub> QDs using the Scherrer formula is estimated to be 3.96 nm. Furthermore, the narrowness of the peaks in Figure 4.4 suggests that the QDs are crystalline.

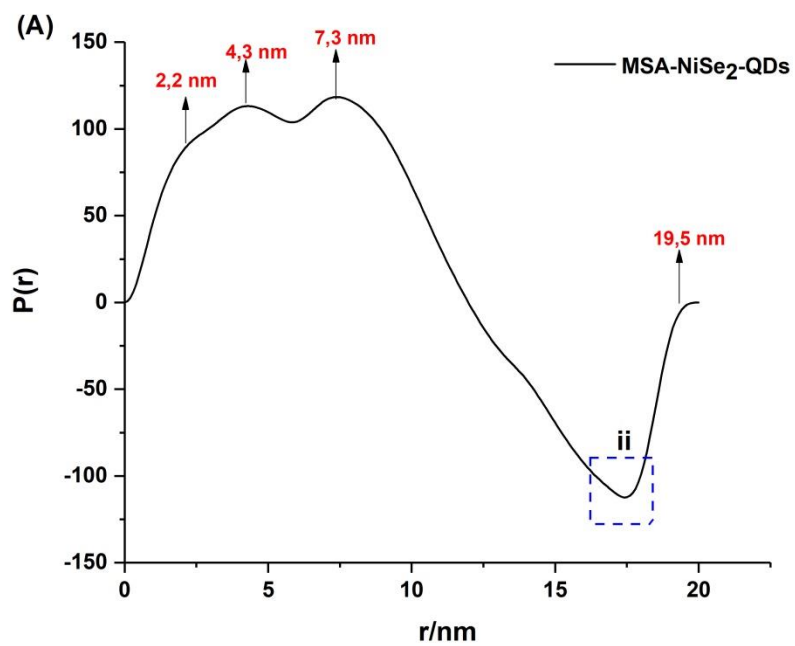
#### 4.1.1.4 Small Angle X-ray Scattering

SAXSpace was used to investigate the shape and size dispersion of water soluble mercaptosuccinic acid capped nickel selenide quantum dots (MSA-NiSe<sub>2</sub> QDs). Here, MSA-NiSe<sub>2</sub> QDs synthesized at different times were investigated, that is, QDs synthesized for 15 min and 45 min, respectively, using the microwave irradiation method. The SAXSpace results were Fourier transformed using the gift software; into pair distance distribution function (PDDF) free model and size distribution by number fraction. The results are shown in Figure 4.5 (A) and (B), and Figure 4.6 (A) and (B), respectively.





**Figure 4.5:** PDDF (A) and Size distributions by number (B) of MSA-NiSe<sub>2</sub> QDs synthesized for 15 min.



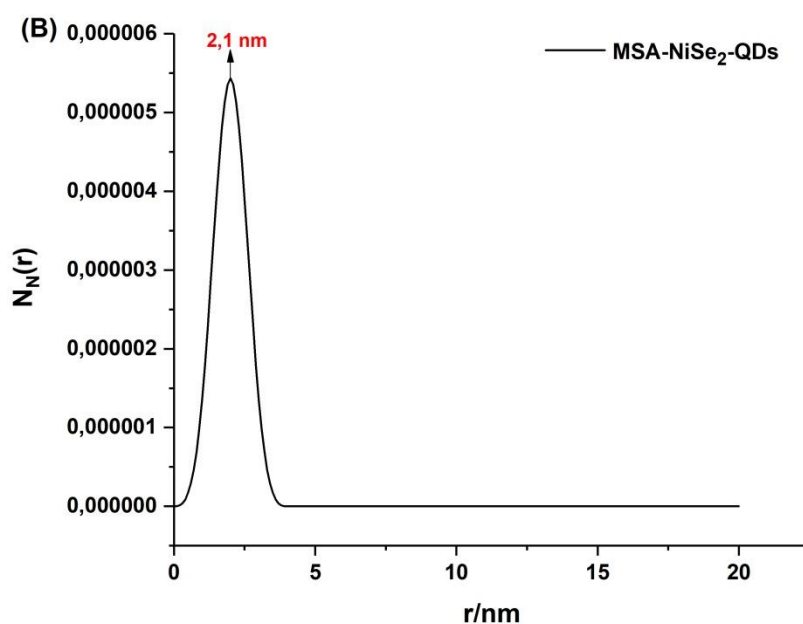


**Figure 4.6:** PDDF (A) and Size distribution by number (B) of the MSA-NiSe<sub>2</sub> QDs synthesized for 45 min.

From Figure 4.5 (A) the PDDF model of the MSA-NiSe<sub>2</sub> QDs synthesized for 15 min indicates three different sized particles with different radii detected at 11.5 nm, 26 nm and 86 nm, respectively. The irregular shape of the PDDF graph indicates that the particles are agglomerated, polydispersed and the extended peak in the negative region as indicated by (i) is due to the shell of the MSA capping agent.<sup>13</sup> The agglomeration of the particles could be due to a phenomenon known as Brownian agglomeration, whereby particles collide and stick together due to their random Brownian motion or it could be due to another phenomenon known as gravitational agglomeration, which is dependent on the size of the particles and their terminal velocity. This means that slowly settling particles are caught by more rapidly settling particles leading to the formation of clusters.<sup>14</sup> From Figure 4.5 (B) the size distribution by number of the MSA-NiSe<sub>2</sub> QDs synthesized for 15 min indicates that a large number of particles are distributed in the 10 nm range due to the intensity of the peak; however, the presence of bigger particles are also detected at 24,5 nm and 38,5 nm, respectively. Figure 4.6 (A) shows the PDDF of the MSA-NiSe<sub>2</sub> QDs synthesized for 45 min. Here, particles of four

different sizes are detected with radii at 2.2 nm, 4.3 nm, 7.3 nm and 19.5 nm, respectively. The irregular shape of the PDDF graph is indicative that agglomeration took place and this could be due to either Brownian agglomeration or gravitational agglomeration. This observation was also observed for the QDs synthesized in just 15 min. It is believed that the capping agent might contribute to agglomeration since a peak associated with MSA in the negative region indicated by (ii) for the 45 min MSA-NiSe<sub>2</sub> QDs was also observed. Figure 4.6 (B) shows the size distribution by number graph of the 45 min MSA-NiSe<sub>2</sub> QDs. From Figure 4.6 (B) it is evident that particles are mainly distributed in the quantum dot region, that is, in the 2.1 nm range. Therefore the QDs synthesized for 45 min are better suited for future applications such as sensor development strategies due to the fact that smaller particles < 20 nm are more favorable as mediating platforms.

## **4.1.2 Microscopic Techniques**

### **4.1.2.1 High resolution transmission electron microscopy (HR-TEM)**

HR-TEM was used to study the shape, size and structure of the mercaptosuccinic acid capped nickel selenide quantum dots (MSA-NiSe<sub>2</sub> QDs). Listed below are the different HR-TEM micrographs of the MSA-NiSe<sub>2</sub> QDs taken at different magnifications

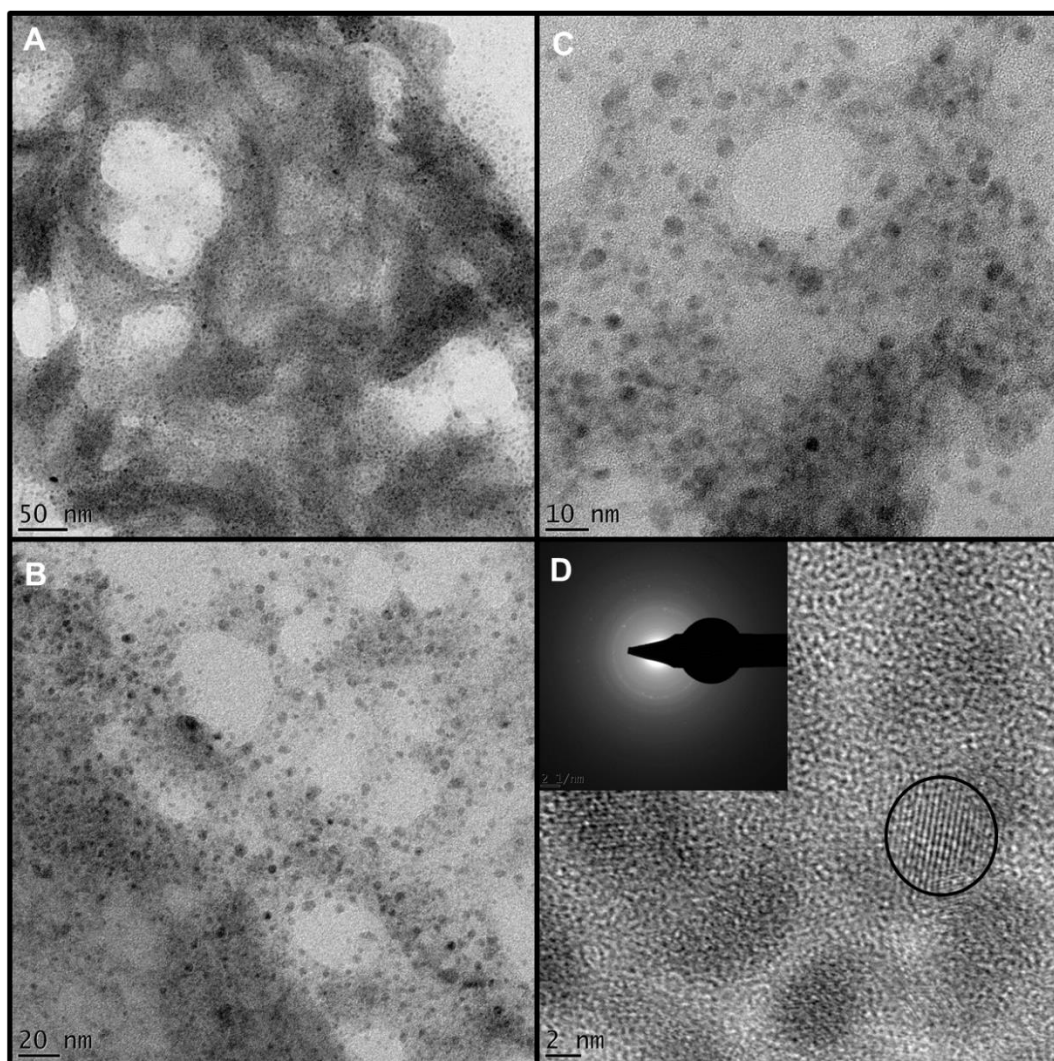


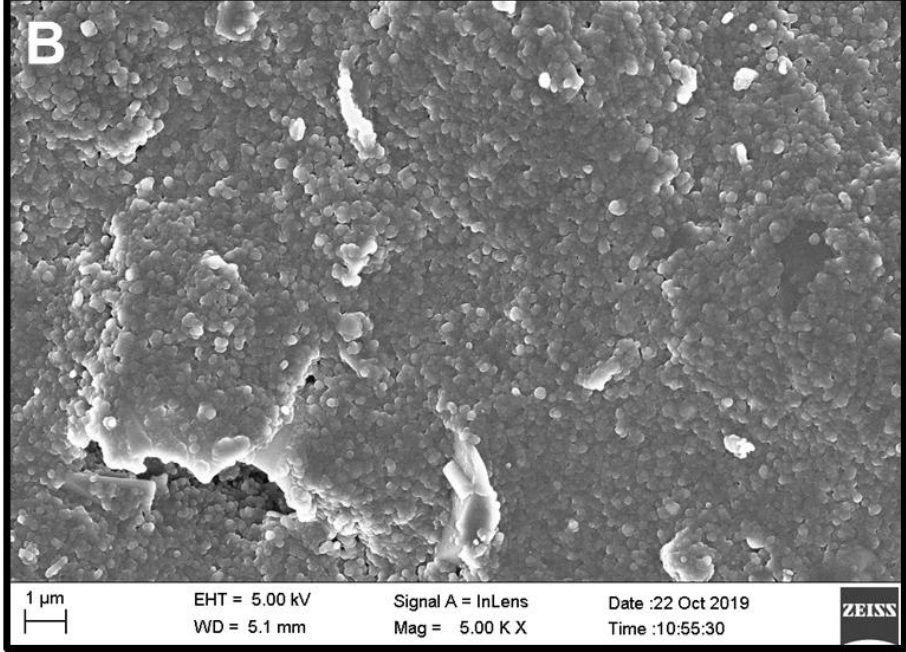
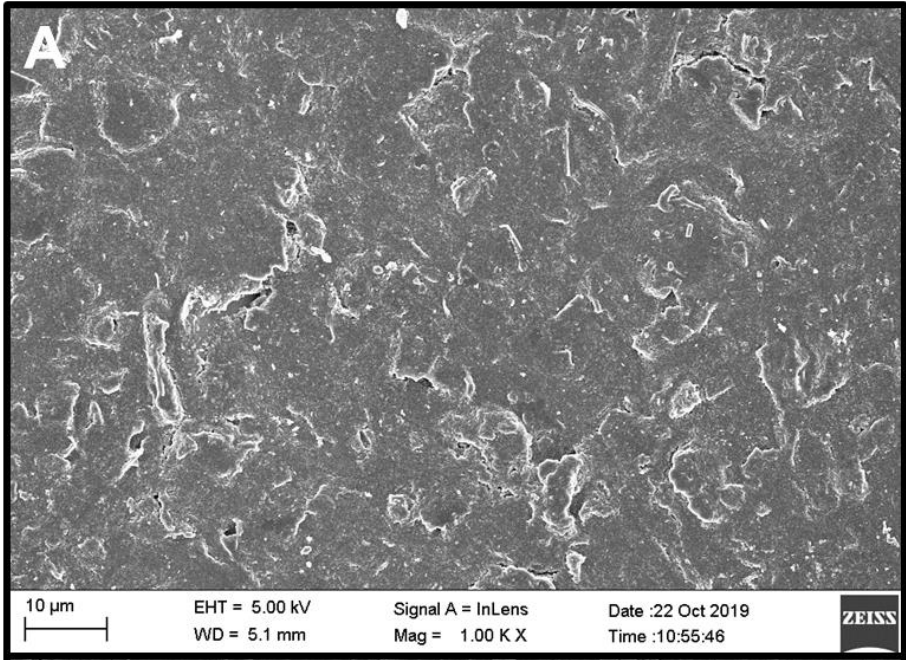
**Figure 4.7:** HR-TEM micrographs of MSA-NiSe<sub>2</sub> QDs taken at 50 nm (A), 20 nm (B), 10 nm (C) and 2 nm (D), respectively.

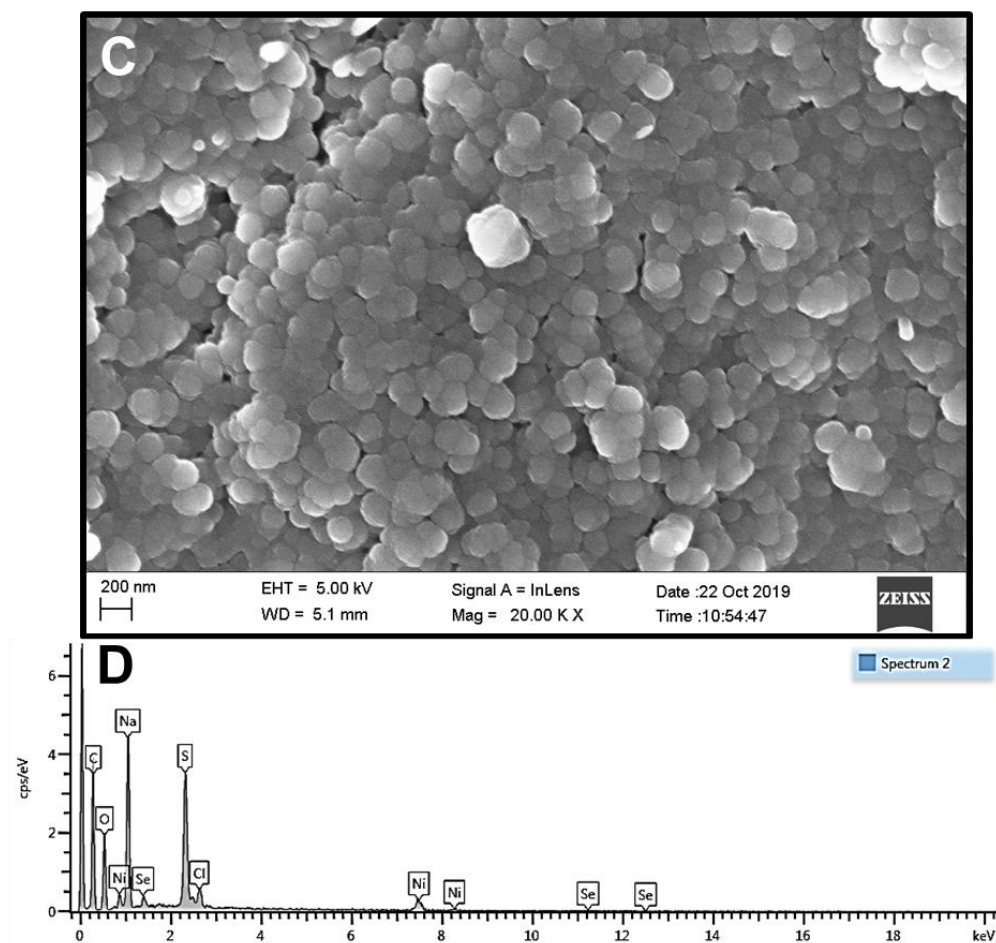
From Figure 4.7 (A), (B), (C) and (D) it can be observed that the MSA-NiSe<sub>2</sub> QDs are polydispersed, spherical in shape with an average diameter of 4 nm. This is in good accordance with the SAXSpace data shown in Figure 4.6 where the average size across the polydispersed QDS were found to be 4 nm. From Figure 4.7 (C) it appears that the MSA-NiSe<sub>2</sub> QDs are agglomerated this can be due to parameters such as surfactant/precursor ratio concentration. Hollingsworth and co-workers showed that low surfactant/precursor ratios can lead to agglomeration.<sup>15</sup> Another factor that can contribute to agglomeration is the interaction strength between the surfactant and the quantum dots. If the interaction between the surfactant and the QDs is weak there can be an overgrowth in particle size, thus resulting in agglomeration.<sup>16</sup> The pH is also

another parameter that can lead to agglomeration due to the fact that if the pH is not adjusted in the correct range, a decrease in the ionic strength of the capping agent can occur, which in turn, will lead to instability of the QDs and thus will cause agglomeration.<sup>17</sup> Other factors such as temperature and microwave power during the synthesis process can also cause agglomeration if not optimized. The selected area electron diffraction (SAED) diagram depicted in the left side corner of Figure 4.7 (D) reveals that the MSA-NiSe<sub>2</sub> QDs are crystalline due to the bright spots that make up the rings. This is in accordance with the XRD pattern of the MSA-NiSe<sub>2</sub> QDs depicted in Figure 4.4, where the peaks appear to be narrow and intense, especially the (200) plane, this suggests presence of crystalline component.<sup>18</sup> The crystallinity of the QDs is further confirmed by the presence of lattice fringes as indicated by the circle in Figure 4.7 (D).

#### **4.1.2.2 High resolution scanning electron microscopy (HR-SEM)**

HR-SEM was used to study the structural and morphological characteristics of the mercaptosuccinic acid capped nickel selenide quantum dots (MSA-NiSe<sub>2</sub> QDs). Provided in Figure 4.8 (A), (B), and (C) are the HR-SEM micrographs of the MSA-NiSe<sub>2</sub> QDs at 10  $\mu$ m, 1  $\mu$ m and 200 nm magnifications, while (D) illustrates the EDS spectra of the MSA-NiSe<sub>2</sub> QDs. Figure 4.9 (A), (B) and (C) shows HR-SEM micrographs of the amine modified aptamer + MSA-NiSe<sub>2</sub> QDs at different magnifications that is, 10  $\mu$ m, 1  $\mu$ m and 200 nm, respectively.

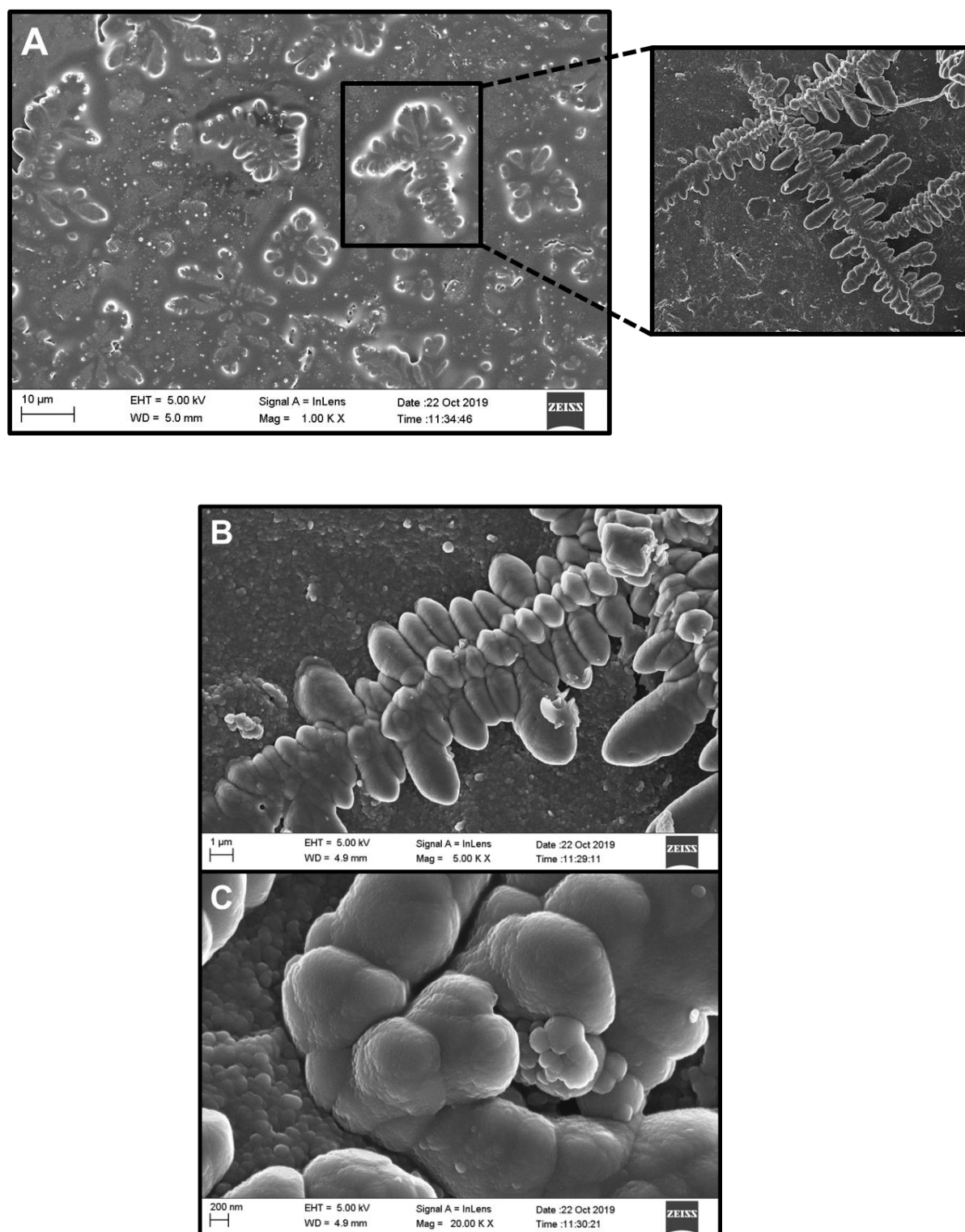




**Figure 4.8:** HR-SEM micrographs of MSA-NiSe<sub>2</sub>-QDs taken at 10 $\mu$ m (A), 1 $\mu$ m (B) and 200 nm (C), respectively, while EDS spectra of the MSA-NiSe-QDs are shown in (D).

From Figure 4.8 (C) it can be seen that the MSA-NiSe<sub>2</sub> QDs are spherical in shape, polydispersed and agglomerated together. The reason for this could be that there was not an efficient amount of capping agent added, this could have led to the QDs having a high surface to volume ratio that increased the attractive forces between the QDs and ultimately lead to agglomeration and polydispersity.<sup>19</sup> From Figure 4.8 (D) the EDS spectra shows that traces of nickel and selenium are present, but in small amounts. The reason for this could be that the molar ratios of the nickel (Ni) precursor to the selenium (Se) were prepared in small amounts, ultimately leading to only small amounts being detected. More Se was detected compared to Ni and this is in accordance with XRD whereby traces of unreacted Se were detected. Sulphur (S) is also present in the EDS spectra and can be attributed to the MSA capping agent. The sodium (Na) detected could be due to the sodium hydroxide (NaOH) solution which was used to adjust the pH

of the Ni precursor. Carbon (C) was also detected and can be attributed to the screen printed carbon electrode on which the MSA-NiSe<sub>2</sub> QDs was immobilized.



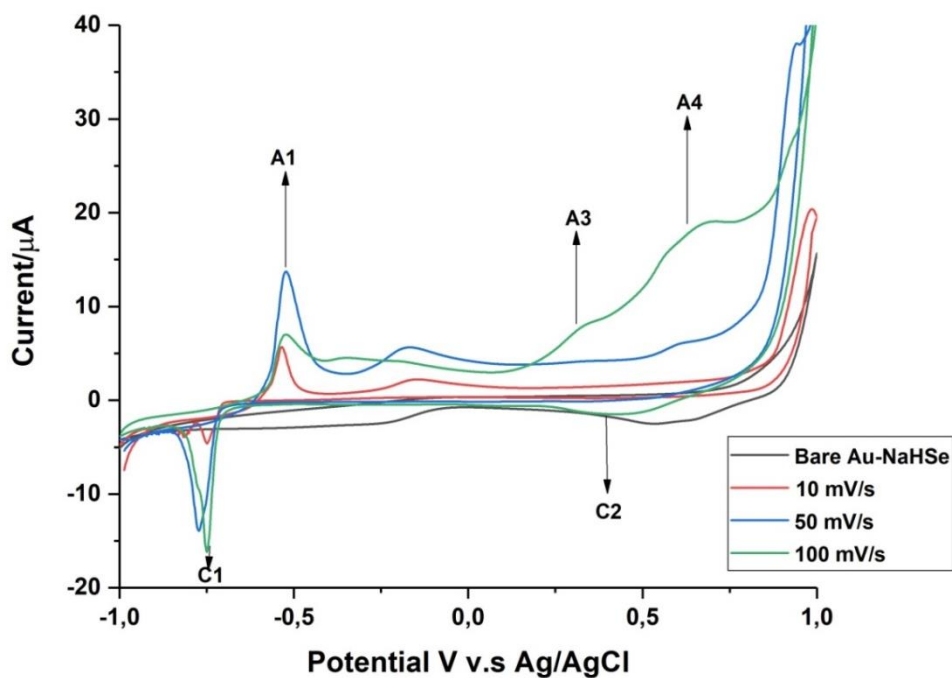
**Figure 4.9:** HR-SEM micrographs of Apt-MSA-NiSe<sub>2</sub> QDs at 10 μm (A), 1 μm (B) and 200 nm (C), respectively.

Figure 4.9 (A), (B) and (C) shows HR-SEM micrographs of the amine modified aptamer + MSA-NiSe<sub>2</sub> QDs at different magnifications, that is, 10 μm, 1 μm and 200 nm, respectively. From Figure 4.9 it is evident that the morphology and topography of the QDs change in the presence of the aptamer. The reason for the change in structure is due to the characteristic properties of aptamers. Aptamers structures are complex and are characterized by internal loops, stems, hairpins or G-quadruplex structures so therefore it could be that when the aptamer bonded with the QDs it formed this internal loop structure that looks leaf-like.<sup>20,21</sup> Another reason could be that since aptamers are single stranded DNA (ssDNA) oligonucleotides the “Velcro effect” could have taken place. The Velcro effect is caused by the sticky ends of the ssDNA, so when the ssDNA comes into contact with the spherical shaped MSA-NiSe<sub>2</sub> QDs it causes structural changes such as the leaf-like structures as depicted in Figure 4.9 (A), (B) and (C).<sup>22</sup>

### **4.1.3 Electrochemical techniques**

#### **4.1.3.1 Cyclic Voltammetry (CV)**

CV was used to investigate the electrochemical properties of the mercaptosuccinic acid nickel selenide quantum dots (MSA-NiSe<sub>2</sub> QDs) on gold conventional and screen printed electrodes as well as on glassy carbon conventional and screen printed electrodes. The pH of the buffer was kept constant at 7.4 as it was an ideal condition for the biological material. The reason for studying the QDs on different electrode substrates was to determine which substrate surface would be suitable and ideal for future sensor development strategies. First, the precursors used to produce the MSA-NiSe<sub>2</sub> QDs was investigated. This was done to determine the peak characteristics of the precursors, and thus eliminate any peaks associated with the precursors when QDs peaks are investigated.



**Figure 4.10:** Cyclic voltammograms of conventional bare AuE and NaHSe precursor in 10 mM PBS, pH 7.4 at a scan rate of 10, 50 and 100 mV/s, respectively.

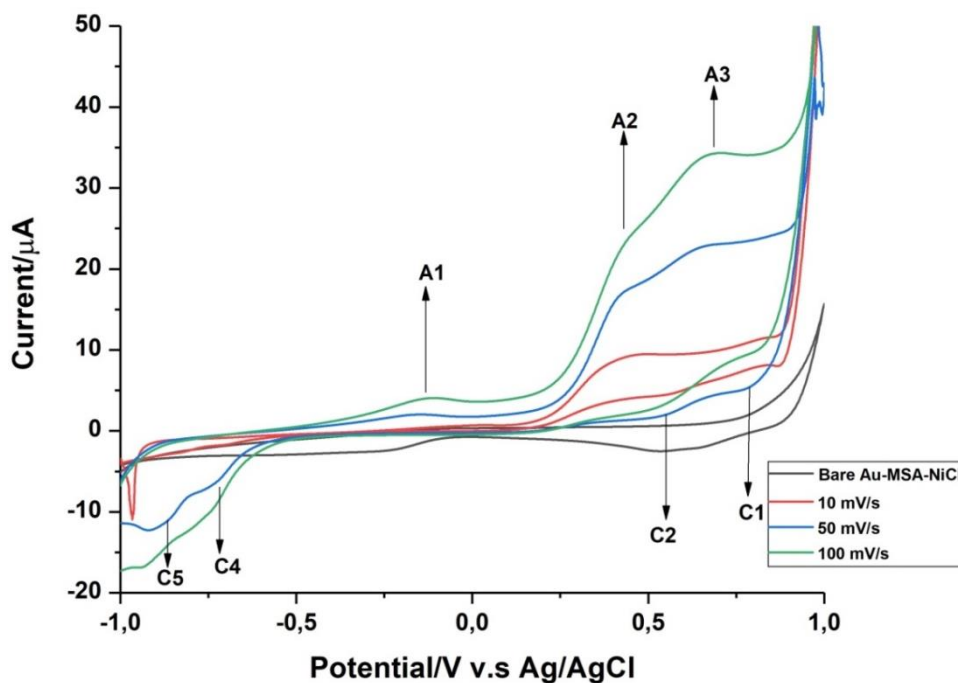
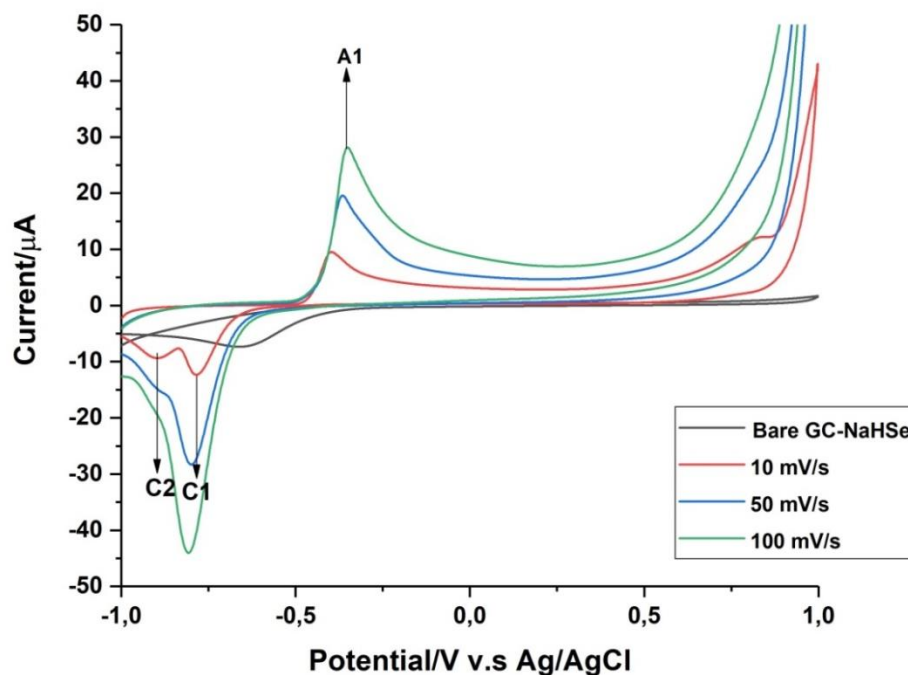


**Figure 4.11:** Cyclic voltammograms of conventional bare AuE and MSA-NiCl<sub>2</sub> precursor in 10 mM PBS, pH 7.4 at a scan rate of 10, 50 and 100 mV/s, respectively.

Figure 4.10 shows overlapping CV curves of NaHSe at different scan rates, that is 10, 50 and 100 mV/s, and a CV curve of a bare conventional gold electrode (AuE) in 10 mM PBS, pH 7.4. Here, two oxidation peaks namely, A1 located at -0.53 V and A3 located at +0.30 V for the NaHSe can be observed. These peaks can be ascribed to the oxidation of  $\text{Se}^{4+}$  to  $\text{Se}^0$ , due to the fact that selenium can engage in self-exchange reactions. A reduction peak C1 located at -0.80 V can also be observed, and may be due to the reduction of  $\text{Se}^0$  to  $\text{Se}^{2-}$ , which is a result of the reaction of selenium in phosphate buffer. This reaction is given by Equation 4.4 below.

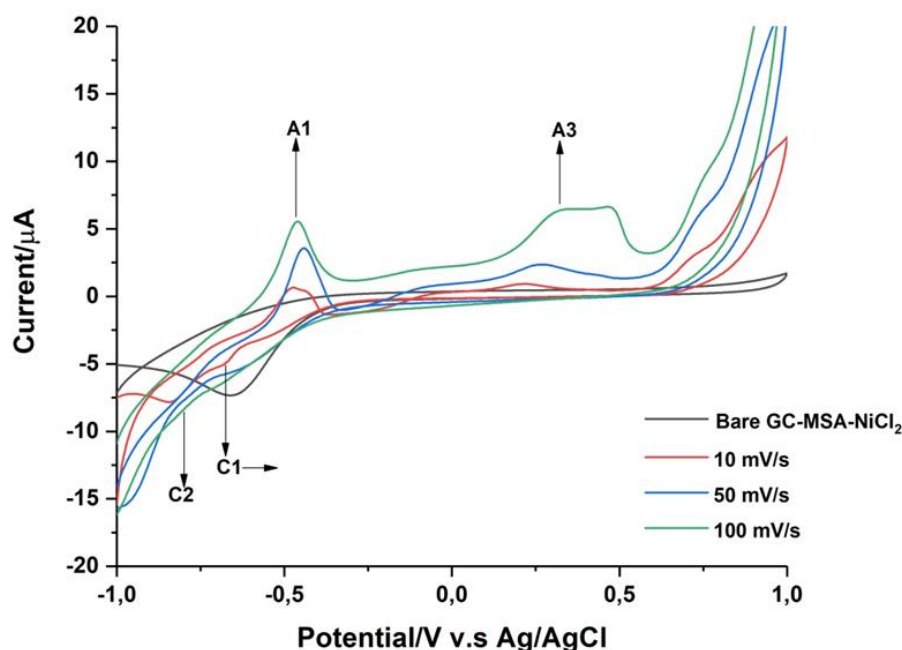


where, NaHSe corresponds to selenium being reduced to the 2- reduction state.<sup>23</sup> The oxidation peak A4 located at +0.65 V could be due to the formation of gold oxide since a conventional AuE is used as the substrate. In addition, another reduction peak C2 located at +0.4 V can be observed, and this can be due to the reduction of gold; however, there is a shift of this peak to more negative potentials.<sup>24</sup> Looking at Figure 4.11, two oxidation peaks for mercaptosuccinic acid-nickel chloride (MSA-NiCl<sub>2</sub>) precursor can be observed, that is, peak A1 located at -0.14 V and peak A2 located at +0.43 V. These peaks are due to the oxidation of  $\text{Ni}^{2+}$  to  $\text{Ni}^{3+}$ .<sup>25</sup> Since this precursor is also studied at the surface of a conventional AuE, gold characteristic peaks will be observed. An oxidation peak A3 located at +0.64 V is due to the formation of gold oxide. It should be noted that there is a broadening of the oxidation peak since the gold oxide peak overlaps with the oxidation peak of the MSA-NiCl<sub>2</sub> precursor. The same was observed for the NaHSe precursor in Figure 4.10. The reduction peak C1 could be due to the reduction of oxygen due to the fact that the solution was not purged long enough and some oxygen molecules were still present in the solution.<sup>26</sup> The reduction peak C2 located at +0.55 V is due to the reduction of gold. Furthermore, extra two reduction peaks can be observed, the first peak C4 located at -0.73 V, can be due to the reduction of  $\text{Ni}^{2+}$  to  $\text{Ni}^0$ ,<sup>27</sup> while peak C5 located at -0.82 V, can be due to hydrogen evolution.<sup>28</sup>



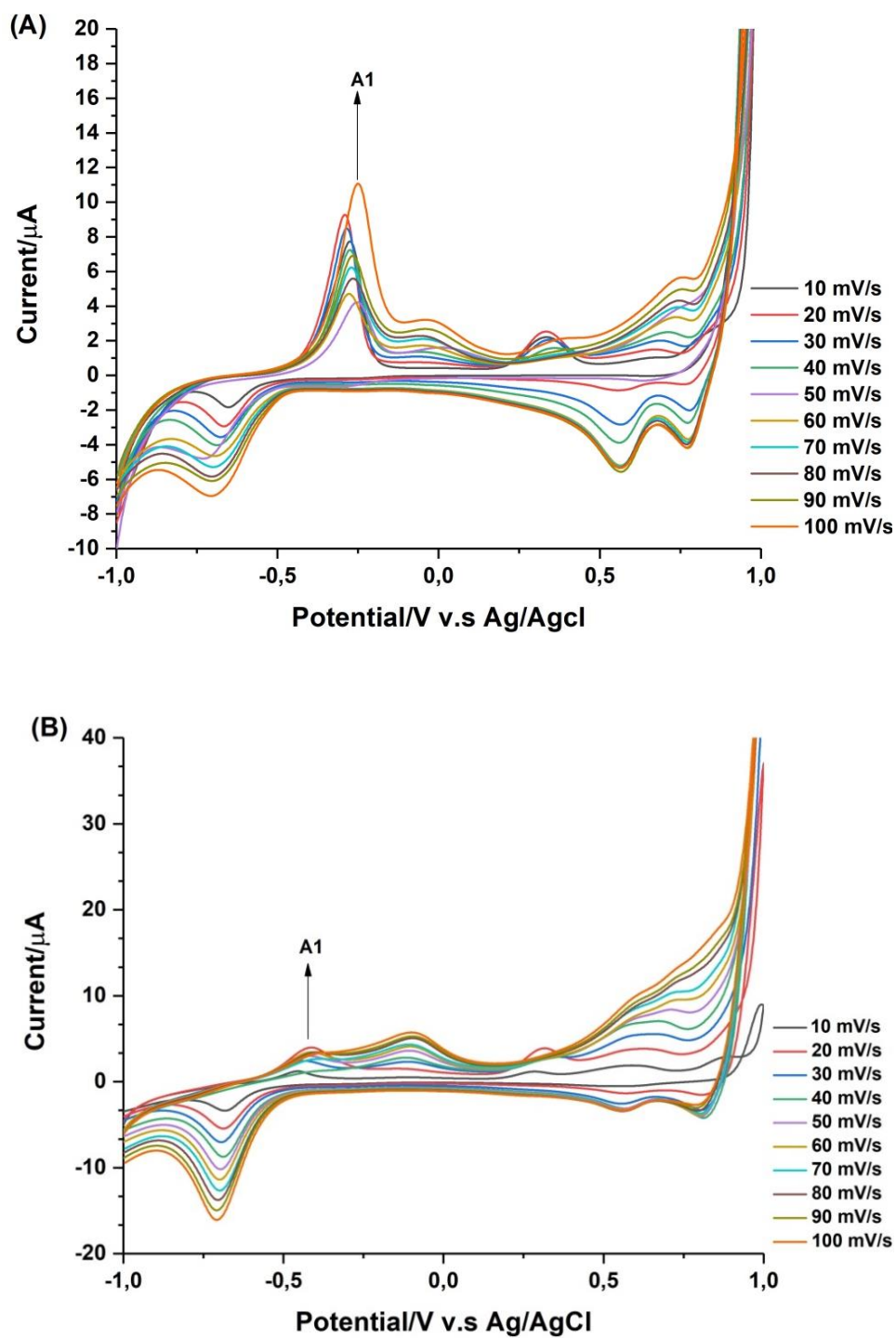
**Figure 4.12:** Cyclic voltammograms of conventional bare GCE and NaHSe precursor in 10 mM PBS, pH 7.4 at a scan rate of 10, 50 and 100 mV/s, respectively.

The precursors NaHSe and MSA-NiCl<sub>2</sub> were also investigated at a conventional glassy carbon electrode (GCE) in 10 mM PBS, 7.4, at different scan rates in the range 10, 50 and 100 mV/s. From Figure 4.12 it is evident that only one oxidation peak is present for NaHSe. The oxidation peak A1 can be due to Se<sup>4+</sup>. The peak for Se<sup>0</sup> cannot be seen and this can be due to the effect of the scan rate and surface substrate causing the interchangeable interactions between Se<sup>4+</sup>/Se<sup>0</sup> not to be depicted on the cyclic voltammogram.<sup>29</sup> The reduction peak C1 located at -0.73 V may be due to the reduction of Se<sup>0</sup> to Se<sup>2-</sup>,<sup>30</sup> while the reduction peak C2 located at -0.81 V can be due to hydrogen evolution



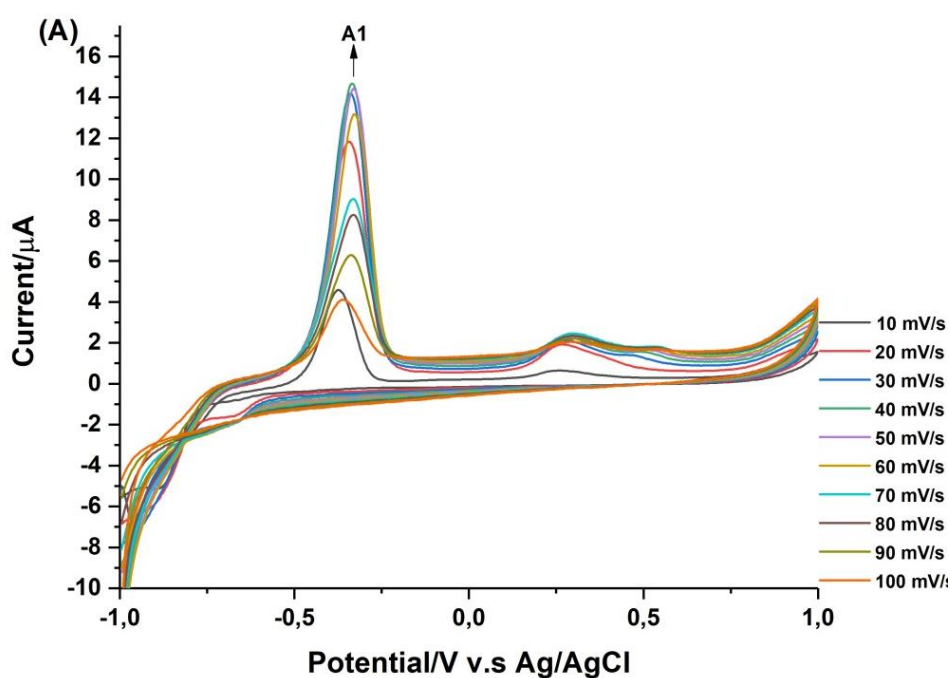
**Figure 4.13:** Cyclic voltammograms of conventional bare GCE and MSA-NiCl<sub>2</sub> precursor in 10 mM PBS, pH 7.4 at a scan rate of 10, 50 and 100 mV/s, respectively.

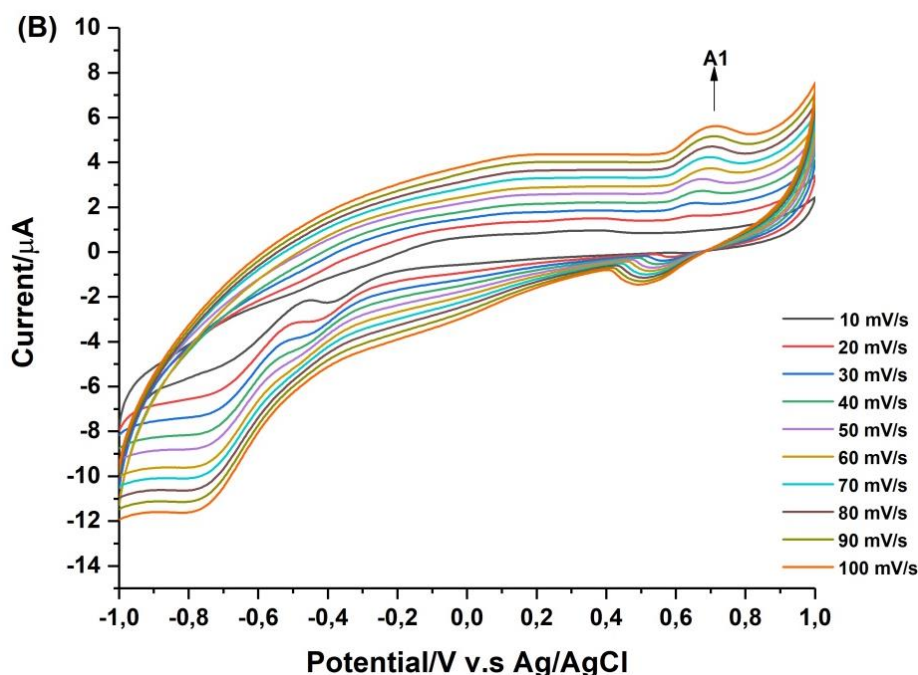
Figure 4.13 shows the electrochemical characteristics of MSA-NiCl<sub>2</sub> at a conventional GCE. Here, the oxidation peaks A1 located at -0.46 V and A3 located at -0.32 V can be attributed to the oxidation of Ni<sup>2+</sup> to Ni<sup>3+</sup>.<sup>31</sup> The oxidation peak at A3 has a shoulder peak which could be related to the dissolution of the electrode at 100 mV/s, which is an indication of the instability of the electrode at that scan rate.<sup>32</sup> The reduction peak C2 located at -0.83 V may be due to hydrogen evolution.<sup>33</sup> It should be noted that characteristic peaks of the precursors were located at more or less the same potentials even if different electrode substrates were employed. However, there was some shift in peak potentials and even disappearance of some peaks. This was observed when the precursors were studied at the GCE surface. It is known that gold has its own characteristic peaks, thus when the precursors were studied at the GCE, the peaks associated with gold was not present, obviously this was expected.



**Figure 4.14:** Cyclic voltammograms of MSA-NiSe<sub>2</sub> QDs in solution at a conventional AuE (A) and immobilized on a conventional AuE (B) in 10 mM PBS, pH 7.4, at multiple scan rates ranging from 10 to 100 mV/s.

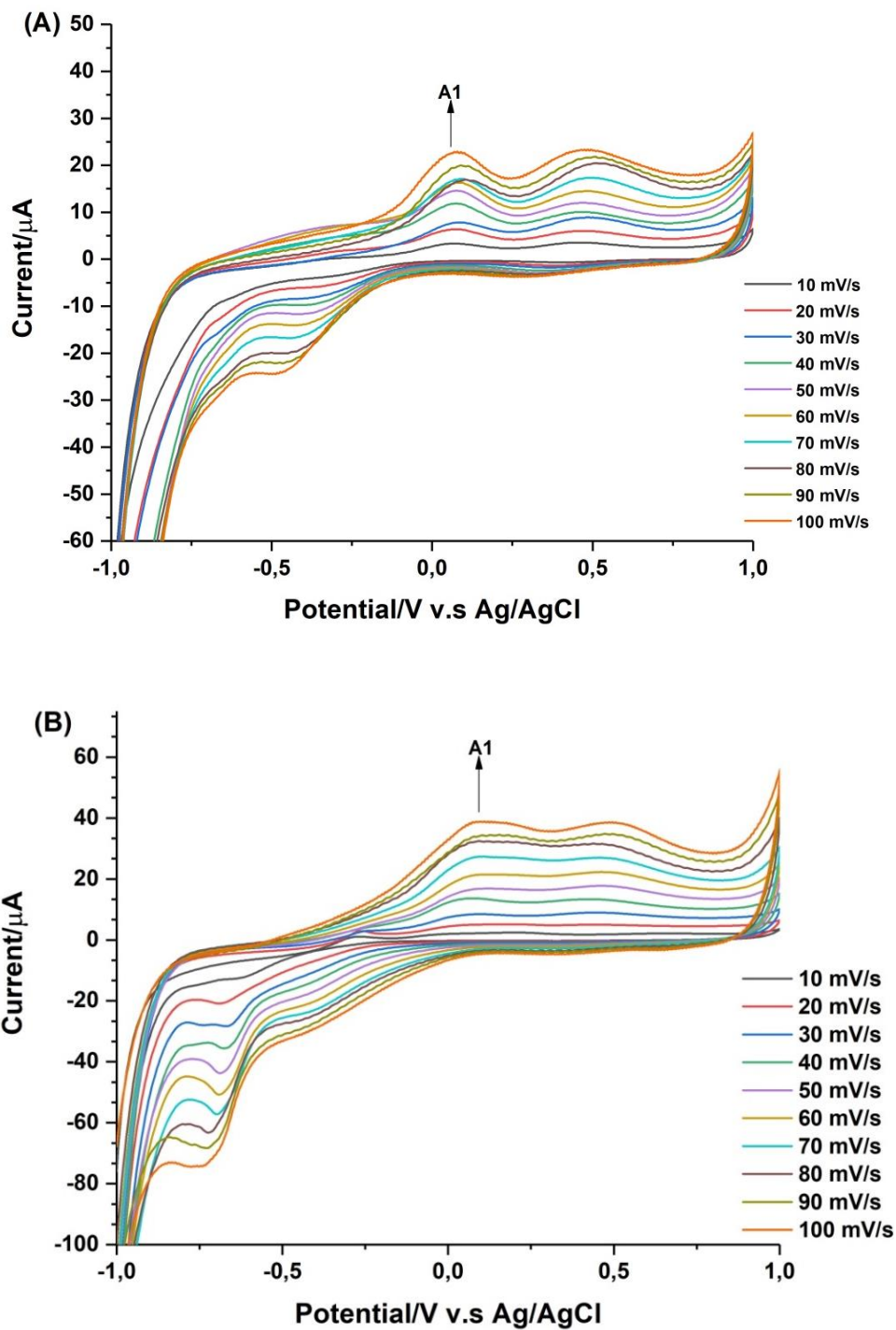
Figure 4.14 (A) and (B) shows the electrochemical characteristics of the MSA-NiSe<sub>2</sub> QDs at a conventional AuE. Here, peak A1 is considered to be the peak characteristics of the MSA-NiSe<sub>2</sub> QDs, due to the fact the NaHSe precursor and the MSA-NiCl<sub>2</sub> precursor overlaps at this point as depicted in Figure 4.12 and Figure 4.13, respectively.<sup>34</sup> Figure 4.14 (A) shows the CV of MSA-NiSe<sub>2</sub> QDs studied in solution, in this case, in 10 mM PBS, pH 7.4, at different scan rates. It can be seen that the peaks associated with the MSA-NiSe<sub>2</sub> QDs are shifting and overlapping as the scan rate is increased. This may be due to the particle size effects of the QDs. Since the QDs are polydispersed as confirmed by HR-TEM, bigger particles will diffuse to the electrode surface slower as compared to the smaller particles, this in turn, will cause some defects at the electrode surface and as such result in the overlapping of peaks, as observed in Figure 4.14 (A).<sup>38</sup> Figure 4.14 (B) shows the CV curves of adsorbed MSA-NiSe<sub>2</sub> QDs on the AuE. It is evident that the peaks observed for the MSA-NiSe<sub>2</sub> QDs studied in solution in Figure 4.14 (A) corresponds to the peaks observed for adsorbed MSA-NiSe<sub>2</sub> QDs depicted in Figure 4.14 (B). The only difference is that the peak currents for the adsorbed MSA-NiSe<sub>2</sub> QDs are smaller than that of the MSA-NiSe<sub>2</sub> QDs studied in solution. This can be due to the presence of cysteamine. Self-assembled monolayers (SAMs) like cysteamine can cause slow diffusion of electrons to the electrode surface due to the stability and the concentration of the SAM on the electrode surface.<sup>39</sup>





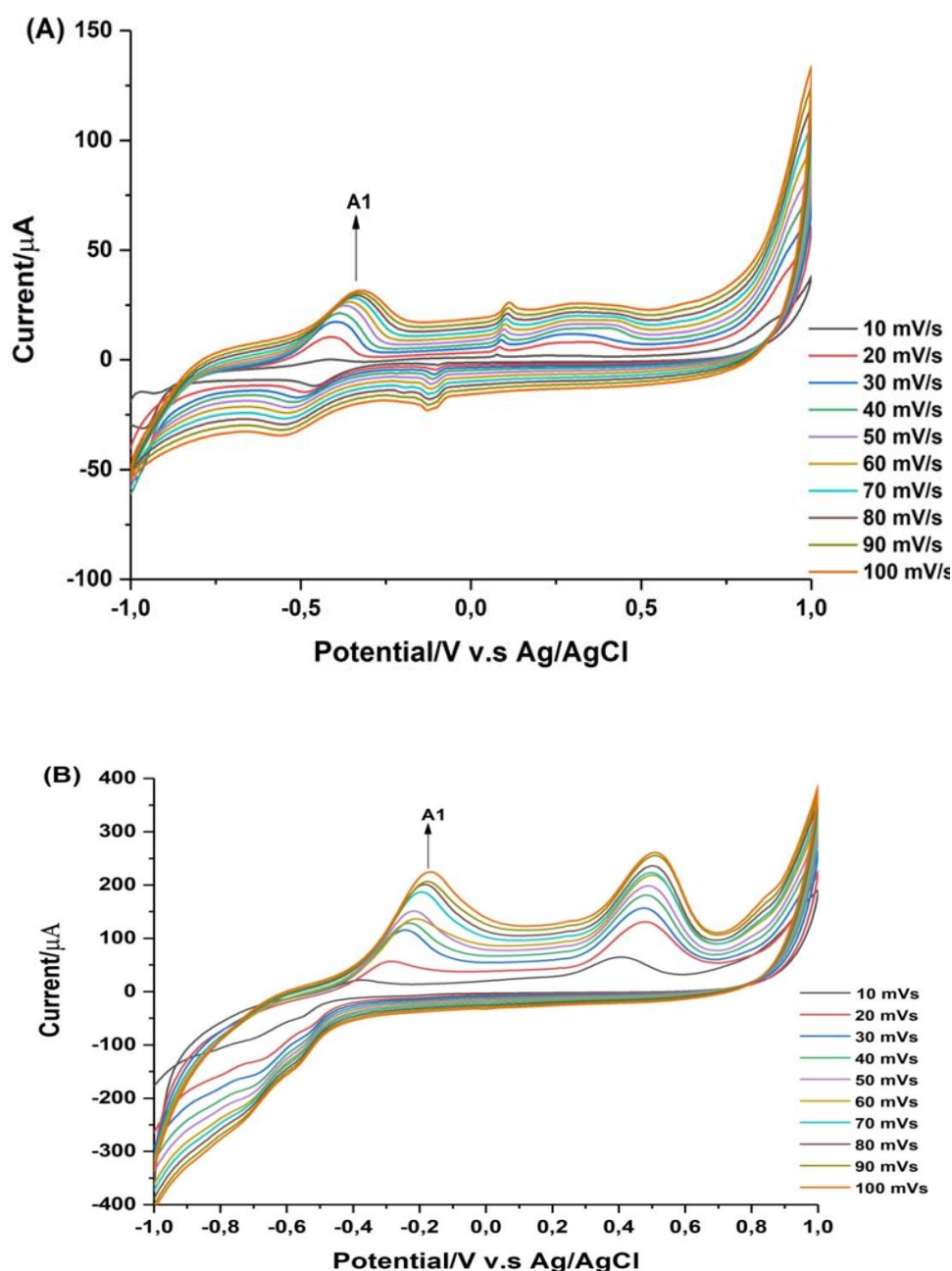
**Figure 4.15:** Cyclic voltammograms of MSA-NiSe<sub>2</sub> QDs in solution at a conventional GCE (A) and immobilized on a conventional GCE (B) in 10 mM PBS, pH 7.4, at multiple scan rates ranging from 10 to 100 mV/s.

Figure 4.15 (A) and (B) shows peak characteristics of solution as well as adsorption phase MSA-NiSe<sub>2</sub> QDs, at a conventional glassy carbon electrode (GCE). Peak A1 in both Figure 4.15 (A) and (B) corresponds to the oxidation of MSA-NiSe<sub>2</sub> QDs. From Figure 4.15 (A) it is evident that the QDs peaks seem to overlap and start to decrease at scans higher than 50 mV/s. This could be due to defects that are common to semiconductor nanocrystals. The defects states are caused by crystal defects or by impurities in the core that causes the overlapping and inconsistent increase of peaks during cyclic voltammetry. In Figure 4.15 (B), the oxidation peak for the MSA-NiSe<sub>2</sub> QDs appears to be very weak and it becomes non-existent as the scan rate increases. This might be due to the non-electro active products of the MSA-NiSe<sub>2</sub> QDs that participate in a chemical reaction as the scan rate is increased.<sup>39</sup>



**Figure 4.16:** Cyclic voltammograms of MSA-NiSe<sub>2</sub> QDs in solution at a SPAuE (A) and immobilized on a SPAuE surface (B) in 10 mM PBS, pH 7.4, at multiple scan rates ranging from 10 to 100 mV/s.

Figure 4.16 (A) and (B) shows voltammograms of MSA-NiSe<sub>2</sub> QDs at a screen printed gold electrode (SPAuE), in 10 mM PBS, pH 7.4. Here, the MSA-NiSe<sub>2</sub> QDs peak A1 appears to increase consistently with an increase in scan rate from 10 mV/s to 100 mV/s. In addition, the peak A1 also seems to shift to more positive potentials for both solution phase QDs as well as QDs adsorbed on the SPAuE surface.



**Figure 4.17:** Cyclic voltammograms of MSA-NiSe<sub>2</sub> QDs in solution at a SPCE (A) and immobilized on a SPCE surface (B) in 10 mM PBS, pH 7.4, at multiple scan rates ranging from 10 to 100 mV/s.

Figure 4.17 (A) and (B) shows scan rate dependent studies of solution phase as well as adsorption phase MSA-NiSe<sub>2</sub> QDs, at a screen printed carbon electrode (SPCE) in 10 mM PBS, pH 7.4. For both solution and adsorption phase QDs it is evident that peak A1 increase as the scan rate increases. Furthermore, by comparing the peak positions of the QDs in both Figure 4.17 (A) and Figure 4.17 (B) it is evident that peak A1 shift to more positive potentials for surface bound MSA-NiSe<sub>2</sub> QDs. The surface bound QDs also shows higher peak currents compared to solution phase QDs at the same electrode. For this reason, the surface coverage of the adsorbed QDs on the SPCE was determined.

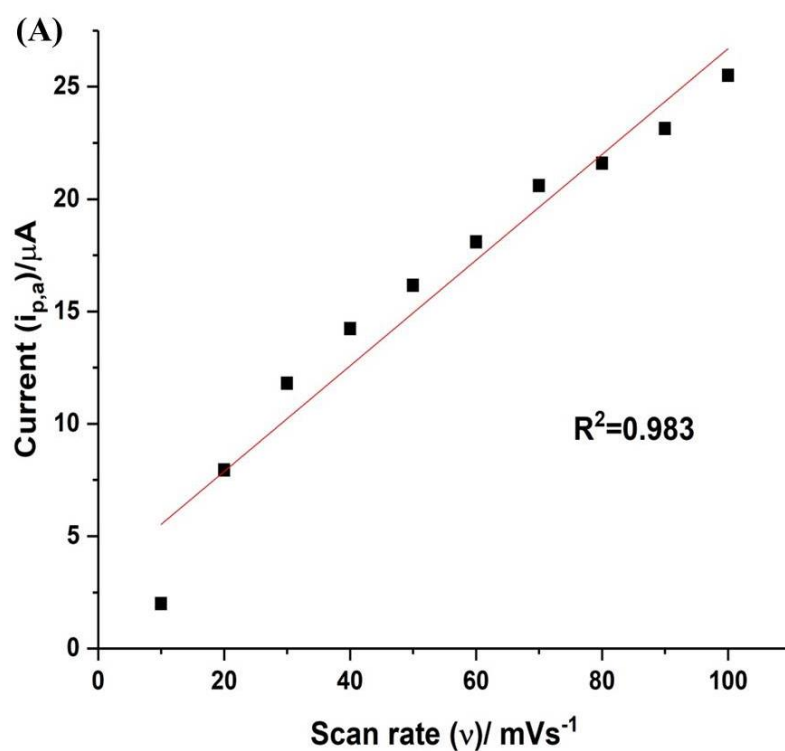
**Table 4.1:** Electrochemical data of MSA-NiSe<sub>2</sub> QDs acquired from cyclic voltammograms ran at different scan rates in the range 10 to 100 mV/s presented in Figure 4.17.

Scan rate/mV/s	Anodic peak potential (E <sub>p,a</sub> )	Anodic peak current (I <sub>p,a</sub> )
10	0.41	63
20	0.47	126
30	0.47	153
40	0.47	177
50	0.47	194
60	0.47	214
70	0.47	220
80	0.48	232
90	0.48	248
100	0.48	254

Since the electrochemical reaction was irreversible and controlled by adsorption the surface concentration of MSA-NiSe<sub>2</sub> QDs adsorbed on the SPCE could be determine by the Brown Anson approximation given by Equation 4.5 below:

$$i_{pa} = \frac{n^2 F^2 A \Gamma}{4RT} \quad 4.5$$

where,  $i_{pa}$  is the peak current in A,  $n= 1$  number of electrons,  $F= 96485 \text{ C mol}^{-1}$  (Faradays constant),  $A= 0.125 \text{ cm}^2$  geometric area of electrode,  $R= 8.314 \text{ Jmol}^{-1}\text{K}^{-1}$  (gas constant),  $T= 298.15 \text{ K}$  absolute temperature and  $v$  is the scan rate  $\text{Vs}^{-1}$  and  $\Gamma$  (surface coverage concentration).<sup>46</sup>



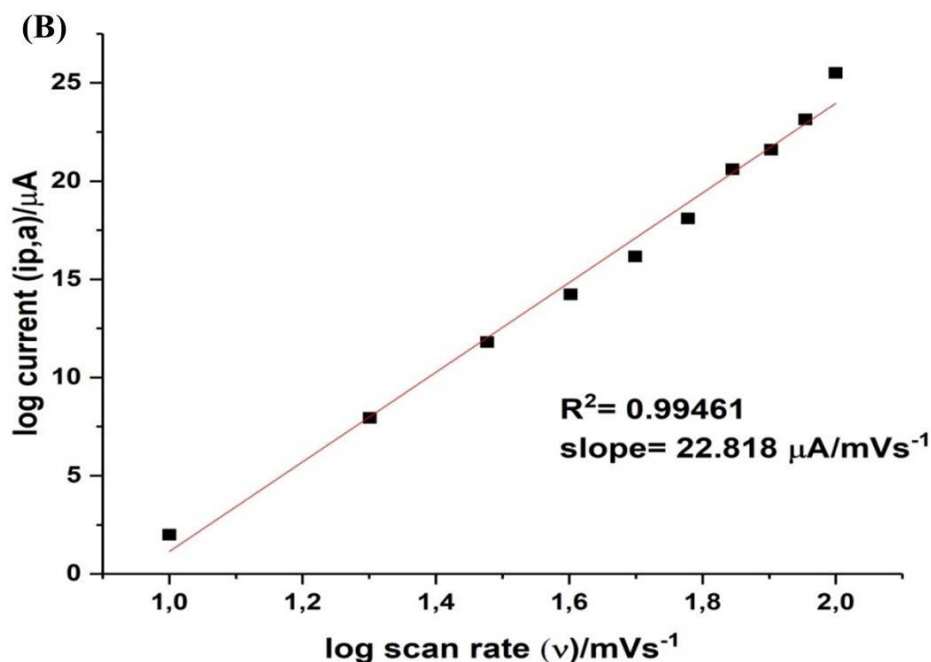


**Figure 4.18:** Shows the anodic plot (peak A1) of peak current ( $I_{p,a}$ ) versus scan rate ( $v$ ) (A) and plot of log peak current ( $I_{p,a}$ ) versus log scan rate ( $v$ ) (B).

The surface concentration of the MSA-NiSe<sub>2</sub> QDs adsorbed on the screen printed glassy carbon electrode was calculated to be  $1.94 \times 10^{-9} \text{ mol/cm}^2$ .

Based on the ideal electrochemical response of surface bound MSA-NiSe<sub>2</sub> QDs on SPCEs it was decided that future analytical applications will be carried out using this electrode platform setup. In addition, since an electrochemical sensor will be developed using MSA-NiSe<sub>2</sub> QDs as a mediator it is also suggested that the SPCE should be used as sensor support due to the fact that it does not have its own electrochemical characteristics peaks which might affect the sensor's response.

#### 4.1.3.2 Electrochemical impedance spectroscopy (EIS)

In this research study EIS was used to investigate the electrocatalytic properties of the mercaptosuccinic acid capped nickel selenide quantum dots (MSA-NiSe<sub>2</sub> QDs) in 10 mM PBS, pH 7.4. Figure 4.19 shows nyquist plot for the bare screen printed carbon electrode (SPCE) and the surface bound MSA-NiSe<sub>2</sub> QDs on SPCE, respectively. While Figure 4.20 shows the corresponding bode plots.

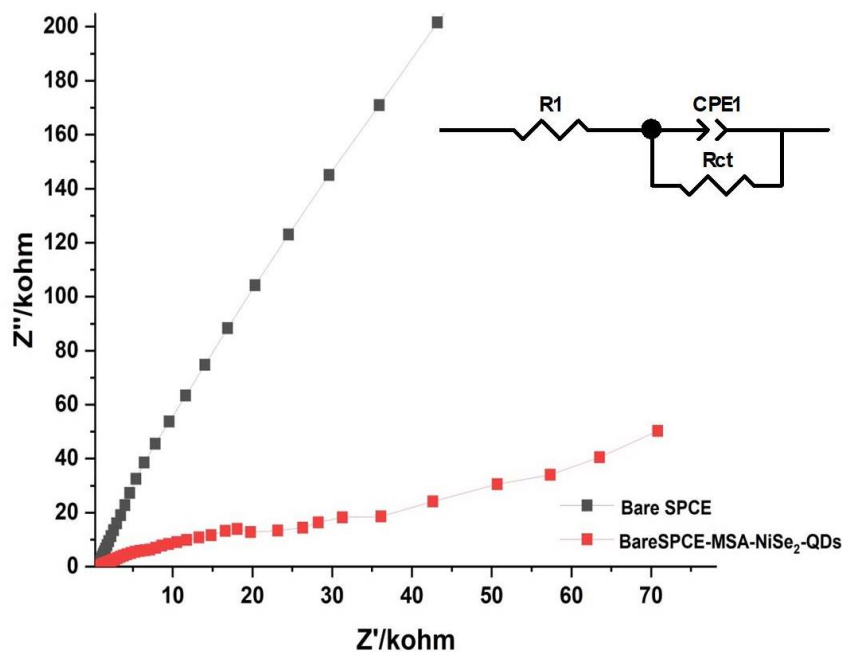


**Figure 4.19:** Nyquist plots of bare SPCE and MSA-NiSe<sub>2</sub>-QDs/SPCE, respectively, in 10 mM PBS, pH 7.4.

The symbols in the Randles equivalent circuit represent the following, that is, R1 is the solution resistance of the electrolyte; CPE1 represents the constant phase element and R<sub>ct</sub> represents the charge transfer resistance. From the Randles equivalent circuit the charge transfer resistance of the bare SPCE was found to be 96.69 kΩ, while the charge transfer resistance of the MSA-NiSe<sub>2</sub> QDs was 17.23 kΩ. Therefore since the MSA-NiSe<sub>2</sub> QDs have a smaller charge transfer resistance it can be concluded that the MSA-NiSe<sub>2</sub> QDs is more conductive than the bare SPCE. It should be noted that a small charge transfer resistance indicates less resistivity of the material.<sup>47</sup> The overpotential of the MSA-NiSe<sub>2</sub> QDs would also be lower than that of the bare SPCE due to the interaction of the QDs with the electrode surface accelerating the rate of electron transfer and lowering the overpotential.<sup>47</sup>

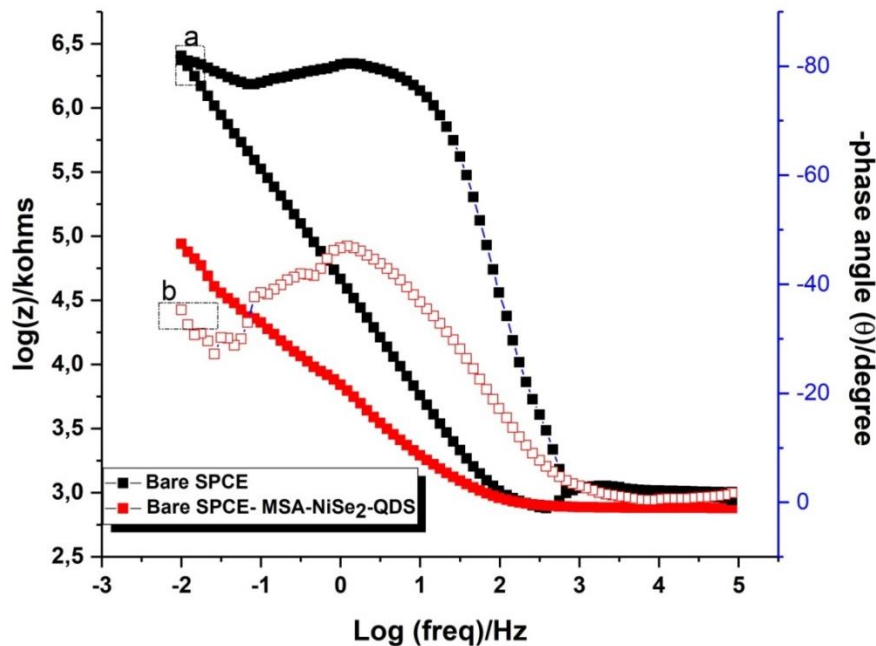


**Figure 4.20:** Bode plots of bare SPCE and MSA-NiSe<sub>2</sub> QDs/SPCE in 10 mM PBS, pH 7.4.

From Figure 4.20 it can be seen that the phase angle decrease with increasing frequency for both the bare SPCE and the MSA-NiSe<sub>2</sub> QDs/SPCE. The bare SPCE has a phase angle of 81° denoted by (a) and the MSA-NiSe<sub>2</sub> QDs/SPCE has a phase angle of 35° denoted by (b). For the phase angle of the bare SPCE and the SPCE-MSA-NiSe<sub>2</sub> QDs the phase angle remained less than 90°. Any surface that has a phase angle less than 90° is viewed as a semi-conductor meaning the modified surface such as the SPCE-MSA-NiSe<sub>2</sub> QDs is permeable to solution ions which means it allows the flow electrons which makes it suitable as a mediating platform.<sup>48</sup> The overpotential of the MSA-NiSe<sub>2</sub> QDs would also lower than that of the bare SPCE due to the interaction of the QDs with the electrode surface accelerating the rate of electron transfer and lowering the overpotential.

## 4.1.4 Characterization of the MSA-NiSe<sub>2</sub>-QDs Aptasensor

### 4.1.4.1 Sensor Fabrication

#### 4.1.4.1.1 Cyclic Voltammetry (CV)

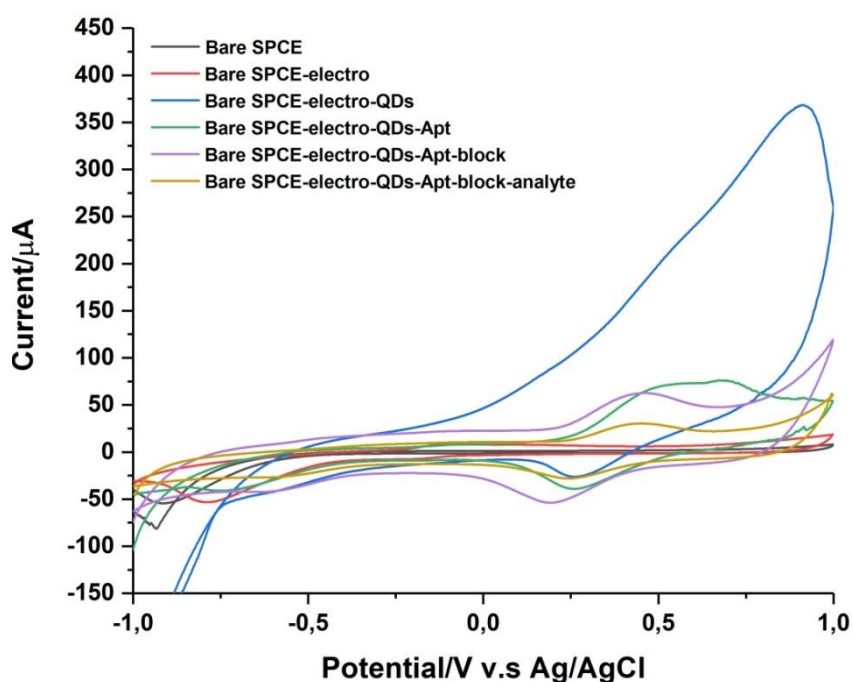


**Figure 4.21:** Overlapping CV curves of bare SPCE, bare SPCE-4-aminophenyl, bare SPCE-4-aminophenyl-QD, bare SPCE-4-aminophenyl-QDs-aptamer, bare SPCE-4-aminophenyl-QDs-aptamer-blocking agent and bare SPCE-4-aminophenyl-QDs-aptamer-blocking agent-analyte in  $[\text{Fe}(\text{CN})_6]^{3-}$ , in 10 mM PBS, pH 7.4

Figure 4.21 shows voltammograms for the different steps in the sensor fabrication process in 100  $\mu\text{M}$  Ferricyanide  $[\text{Fe}(\text{CN})_6]^{3-}$ , in 10 mM PBS, pH, 7.4. The reversible characteristic peaks of the  $[\text{Fe}(\text{CN})_6]^{3-}$  electrochemical probe were monitored to check the change in the electrochemical response for each modification step. After forming the 4-aminophenyl groups on the SPCE via electrographing, the MSA-NiSe<sub>2</sub> QDs was attached to the 4-aminophenyl/SPCE surface via covalent attachment using the EDC/NHS cross linking chemistries. From Figure 4.21 a significant increase in the peak currents for the MSA-NiSe<sub>2</sub> QDs can be observed. This can be due to the QDs good

electronic properties and its ideal conductive behavior. Once the amine modified aptamer is introduced, the peak current decreases which could be due to the interaction of the positively charged amine modified aptamer and the carboxylic group of MSA.<sup>51</sup> Thereafter, the blocking agent MCH was introduced, the peak currents decreased and shifted to more negative potentials. This might be due to the interaction of the blocking agent with the active sites on the electrode, slowing the transfer of electrons to the surface of the electrode. Immobilization of the BNP analyte resulted in further decrease of the peak currents, as seen in Figure 4.21.

#### 4.1.4.1.2 Electrochemical Impedance Spectroscopy (EIS)

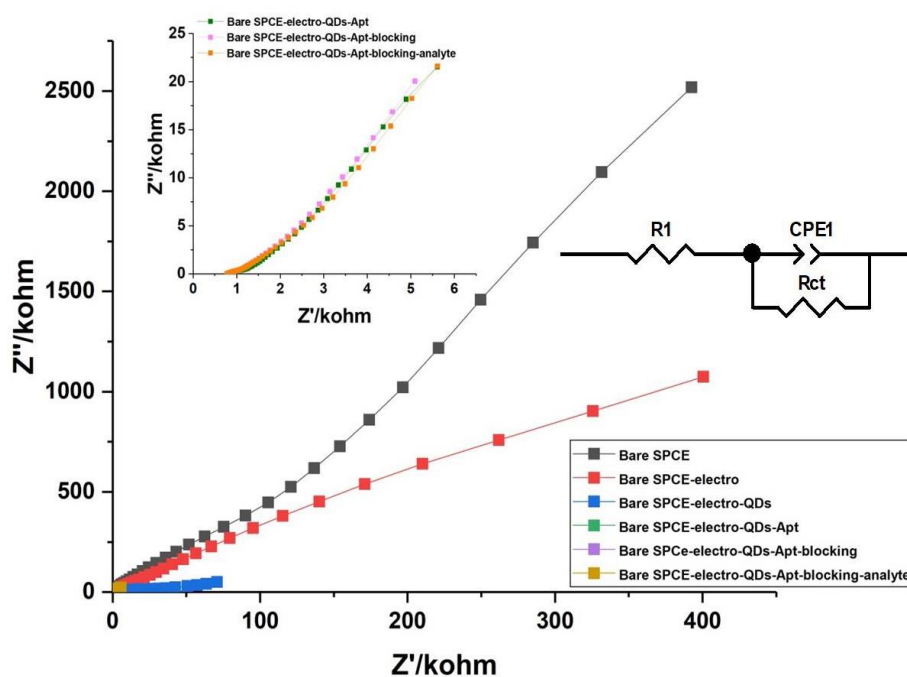


**Figure 4.22:** Nyquist plots of bare SPCE, bare SPCE-4-aminophenyl, bare SPCE-4-aminophenyl-QD, bare SPCE-4-aminophenyl-QDs-aptamer, bare SPCE-4-aminophenyl-QDs-Aptamer-blocking agent and bare SPCE-4-aminophenyl-QDs-aptamer-blocking agent-analyte in  $[\text{Fe}(\text{CN})_6]^{3-}$ , in 10 mM PBS, pH 7.4

Figure 4.22 shows Nyquist plots for the different steps in the sensor fabrication process in 100  $\mu\text{M}$  Ferricyanide  $[\text{Fe}(\text{CN})_6]^{3-}$ , in 10 mM PBS, pH, 7.4. The charge transfer resistance ( $R_{ct}$ ) for each of the different fabrication steps was obtained using a Randles equivalent circuit inserted in the right hand corner of Figure 4.22. The  $R_{ct}$  values for the bare SPCE was 96,79 k $\Omega$ , bare SPCE-4-aminophenyl was 73.68 k $\Omega$ , bare SPCE-4-aminophenyl-QD was 20.29 k $\Omega$ , bare SPCE-4-aminophenyl-QDs-aptamer was 1.96 k $\Omega$ , bare SPCE-4-aminophenyl-QDs-Aptamer-blocking agent was 2.95 k $\Omega$  and bare SPCE-4-aminophenyl-QDs-aptamer-blocking agent-analyte was 1.71 k $\Omega$ . The EIS response for each of the modification steps in the sensor fabrication process exhibited more or less the same trend as observed in the voltammetry analysis. From Figure 4.22 it is evident that as soon as the QDs are introduced on the SPCE surface a drastic decrease in the  $R_{ct}$  value can be observed. This might be due to the repulsion effect of the MSA capped QDs and 4-aminophenyl groups on the SPCE surface, where the negative charge on the carboxylic group of MSA interacts with the positive charge of the amino group of the 4-aminophenyl film, thus resulting in a negative charge density of the QDs, and thus decrease the  $R_{ct}$ .

**Table 4.2:** Charge transfer resistance ( $R_{ct}$ ) values for the different modification steps in the sensor fabrication process.

Sensor fabrication step	Charge transfer resistance ( $R_{ct}/\text{k}\Omega$ )
Bare SPCE	96.79
Bare SPCE-electrodeposit	73.68
Bare SPCE-electrodeposit-QDs	20.29
Bare SPCE-electrodeposit-QDs-aptamer	1.96

Bare SPCE-electrodeposit-QDs- aptamer-blocking agent	2.95
Bare SPCE-electrodeposit-QDs- aptamer-blocking agent-analyte	1.71

#### 4.1.4.2 Detection of brain natriuretic peptide (BNP)

##### 4.1.4.2.1 Differential Pulse Voltammetry (DPV)

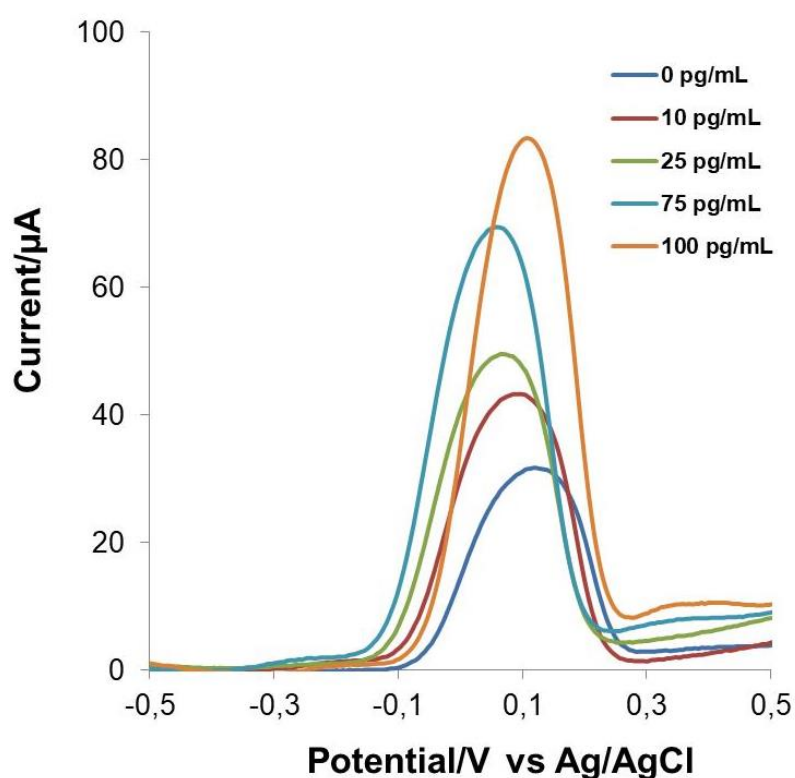


**Figure 4.23:** DPV response of the aptasensor towards different concentrations of BNP in 5 mM  $[\text{Fe}(\text{CN})_6]^{3-}$ , in 10 mM PBS, pH 7.4

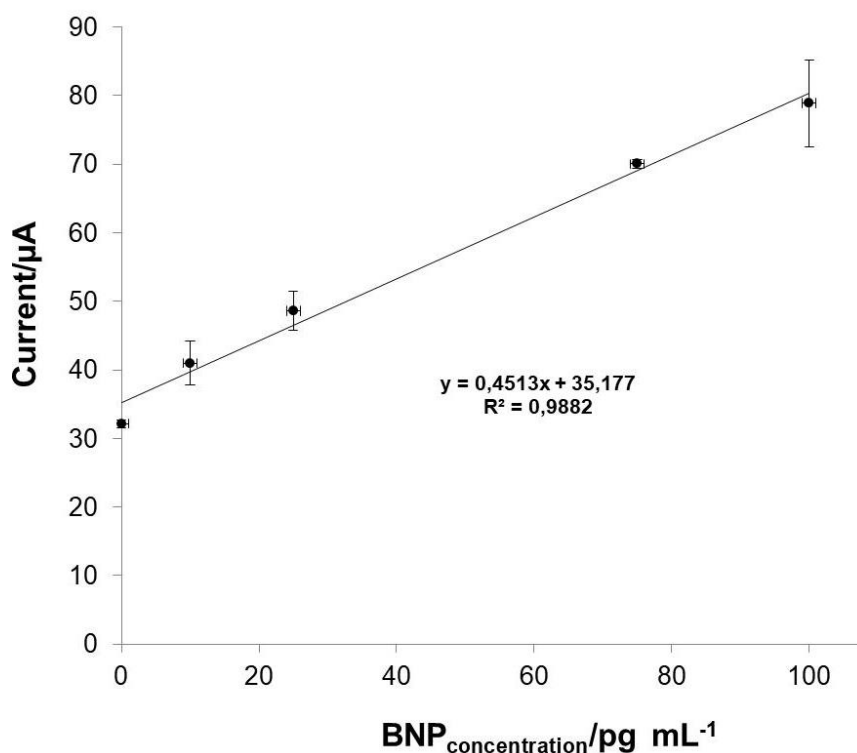


**Figure 4.24:** Calibration plots showing the relationship between the current and the BNP concentration. Each error bar corresponds to the average of no less than three independent replicates (n=3).

Figure 4.23 shows the DPV response signals of the novel MSA-NiSe<sub>2</sub>-QDs based aptasensor towards different concentrations of BNP, while Figure 4.24 shows the corresponding calibrations curves, respectively, in 5 mM Ferricyanide [Fe(CN)<sub>6</sub>]<sup>3-</sup>, in 10 mM PBS, pH 7.4. Here, the change in the characteristics peaks of [Fe(CN)<sub>6</sub>]<sup>3-</sup> was taken as the analytical response of the sensor. From Figure 4.23 it can be seen as the concentrations of BNP increases the peak current increases at a constant rate, indicating a good analytical response of the aptasensor. There is a slight shift in peak potential and this may be due to factors such as the faradaic current and diffusional control reactions, which are influenced by concentration difference.<sup>56</sup> Figure 4.24 shows the corresponding calibration curve of the DPV responses of the aptasensor towards different concentrations of BNP analyte. The calibration curve shows a good linear response with a correlation coefficient  $R^2 = 0.9882$ , which indicates good reproducibility of the sensor.<sup>57</sup> The limit of detection (LOD) was calculated from the calibration curve using 3 times the standard deviation (n=3), and is given by the following Equation 4.6.

$$LOD = \frac{3 \times \text{standard deviation of blank}}{\text{Sensitivity}} \quad 4.6$$

The LOD was determined to be 11.93 pg/mL. The LOD falls within the detection range of BNP levels which ranges from 10-100 pg/mL with a 100 pg/mL being the cut-off for an indication of myocardial infarction. The sensor also indicates good sensitivity due to the fact that it can detect BNP levels under normal conditions in the blood, which is as low as 20 pg/mL.<sup>58</sup> The dynamic range of the sensor is from 0-100 pg/mL, but the calibration curve only refers to the linear part in the calibration curve and the sensor can detect at much lower concentrations or higher concentrations to enable a wide dynamic linear range. The limit of quantification (LOQ) was calculated from Equation 4.7 below.

$$LOQ = \frac{10 \times \text{standard deviation of blank}}{\text{Sensitivity}} \quad 4.7$$

The LOQ was determined to be 36,1 pg/mL, which is the lowest concentration the sensor can detect with a stated accuracy and precision.<sup>59</sup> Listed below is a table for comparison studies of different LODs for BNP detection done by various research groups. Compared to literature the sensor developed for BNP in the present study showed a better LOD than the LOD reported by Maturra and co-workers as well as Gong and co-workers. This can be attributed to the novel MSA-NiSe<sub>2</sub> QDs that was employed as a mediating platform in the aptasensor.

**Table 4.3:** Comparative study for the different detection methods of BNP.

Research group	Detection method	Interface	LOD (pg/ml)	Ref
Grabowska and co-workers	DPV	SPGE modified polyethyleneimine/reduced graphene nanocomposites film-aptasensor	0.9	58
Prasad and co-workers	EIS	Silicon nanowells modified with anti-BNP	0.001	60
Kurita and co-workers	Surface Plasmon Resonance (SPR)	microfluidic device combined with a portable SPR sensor system where sample BNP is introduced into the microchannel after an immunoreaction with acetylcholine esterase-(AChE) labeled antibody	0.015	61
Maturra and co-workers	Linear Sweep Voltammetry (LSV)	Immune reaction using AChE labeled anti-BNP antibodies, detection on silver electrodes by measuring unreacted conjugates from an	20000	62

		enzymatic reaction		
Gong and co-workers	Lateral flow immunoassay (LFIA)	Using an improved LFIA by optimizing gold nanoparticle (GNP)-antibody conjugate conditions	100 pg/ml	63

## 4.2 Conclusion

The characterization of the MSA-NiSe<sub>2</sub> QDs was investigated through spectroscopic, microscopic and electrochemical techniques. The spectroscopic techniques confirmed the successful capping of the capping agent, crystallinity of the QDs and the phase of the QDs. The microscopic techniques confirmed the size of the QDs as well as the successful immobilization of the aptamer with the QDs. The electrochemical techniques confirmed that MSA-NiSe<sub>2</sub> QDs are suitable mediating platforms for detection applications. The detection of the sensor showed a good limit of detection as well as quantification.

## References

- 1 Y. Feng, S. Lin, S. Huang, S. Shrestha and G. Conibeer, Can Tauc plot extrapolation be used for direct-band-gap semiconductor nanocrystals?, *J. Appl. Phys.*, 2015, **117**, 1-9.
- 2 G. Zhang, D. Monllor-Satoca and W. Choi, Band energy levels and compositions of CdS-based solid solution and their relation with photocatalytic activities, *Catal. Sci. Technol.*, 2013, **3**, 1790–1797.
- 3 N. S. Pesika, K. J. Stebe and P. C. Searson, Relationship between Absorbance Spectra and Particle Size Distributions for Quantum-Sized Nanocrystals, *J. Phys. Chem. B*, 2003, **107**, 10412–10415.
- 4 D. K. Seo and R. Hoffmann, Direct and indirect band gap types in one-dimensional conjugated or stacked organic materials, *Theor. Chem. Acc.*, 1999, **102**, 23–32.
- 5 Z. Zhang, Y. Zhu, W. Wang, W. Zheng, R. Lin, X. Li, H. Zhang, D. Zhong and F. Huang, Aqueous Solution Growth of Millimeter-Sized Nongreen-Luminescent Wide Bandgap Cs<sub>4</sub>PbBr<sub>6</sub> Bulk Crystal, *Cryst. Growth Des.*, 2018, **18**, 6393–6398.
- 6 N. Moloto, M. J. Moloto, N. J. Coville and S. Sinha Ray, Synthesis and characterization of nickel selenide nanoparticles: Size and shape determining parameters, *J. Cryst. Growth*, 2018, **324**, 41–52.
- 7 J. C. Cuevas, Thermal radiation from subwavelength objects and the violation of Planck's law, *Nat. Commun.*, 2019, **10**, 1–4.
- 8 I. M. A. Viegas, B. S. Santos, A. Fontes, G. A. De Lima Pereira and C. F. Pereira, Multivariate optimization of optical properties of CdSe quantum dots obtained by a facile one-pot aqueous synthesis, *Inorg. Chem. Front.*, 2019, **6**, 1350–1360.
- 9 P. Krishnamurthi, H. B. Ramalingam and K. Raju, FTIR studies of hydrogen bonding interaction between the hydroxyl and carbonyl liquids, *Adv App Sci.*,

- 2015, **6**, 44–52.
- 10 M. S. Hosseini and A. Pirouz, Study of fluorescence quenching of mercaptosuccinic acid-capped CdS quantum dots in the presence of some heavy metal ions and its application to Hg(II) ion determination, *Luminescence*, 2014, **29**, 798–804.
  - 11 W. Liu, A. Y. Chang, R. D. Schaller and D. V Talapin, Colloidal InSb Nanocrystals.
  - 12 T. A. Grünewald, A. Lassenberger, P. D. J. Van Oostrum, H. Rennhofer, R. Zirbs, B. Capone, I. Vonderhaid, H. Amenitsch, H. C. Lichtenegger and E. Reimhult, Core-Shell Structure of Monodisperse Poly(ethylene glycol)-Grafted Iron Oxide Nanoparticles Studied by Small-Angle X-ray Scattering, *Chem. Mater.*, 2015, **27**, 4763–4771.
  - 13 A. Singer, Z. Barakat, S. Mohapatra and S. S. Mohapatra, Nanoscale Drug-Delivery Systems, *Nanocarriers Drug Deliv.*, 2019, 395–419.
  - 14 J. A. Hollingsworth, Semiconductor Nanocrystal Quantum Dots, *Encycl. Inorg. Bioinorg. Chem.*, DOI:10.1002/9781119951438.eibc0261.
  - 15 I. Fatimah, Green synthesis of silver nanoparticles using extract of *Parkia speciosa* Hassk pods assisted by microwave irradiation, *J. Adv. Res.*, 2016, **7**, 961–969.
  - 16 R. F. Domingos, C. Franco and J. P. Pinheiro, Stability of core/shell quantum dots-role of pH and small organic ligands, *Environ. Sci. Pollut. Res.*, 2013, **20**, 4872–4880.
  - 17 M. Rehan, X. Lai and G. M. Kale, Hydrothermal synthesis of titanium dioxide nanoparticles studied employing in situ energy dispersive X-ray diffraction, *CrystEngComm*, 2011, **13**, 3725–3732.
  - 18 B. Kinkead and T. Hegmann, Effects of size, capping agent, and concentration of CdSe and CdTe quantum dots doped into a nematic liquid crystal on the optical and electro-optic properties of the final colloidal liquid crystal mixture, *J. Mater. Chem.*, 2010, **20**, 448–458.

- 19 J. E. Smith, J. L. Chávez, J. A. Hagen and N. Kelley-Loughnane, Design and development of aptamer–gold nanoparticle based colorimetric assays for in-the-field applications, *J. Vis. Exp.*, 2016, **2016**, 1–10.
- 20 A. Ruscito and M. C. DeRosa, Small-molecule binding aptamers: Selection strategies, characterization, and applications, *Front. Chem.*, 2016, **4**, 1–14.
- 21 S. Balamurugan, A. Obubuafo, S. A. Soper and D. A. Spivak, Surface immobilization methods for aptamer diagnostic applications, *Anal. Bioanal. Chem.*, 2008, **390**, 1009–1021.
- 22 M. R. Jones, R. J. MacFarlane, B. Lee, J. Zhang, K. L. Young, A. J. Senesi and C. A. Mirkin, DNA-nanoparticle superlattices formed from anisotropic building blocks, *Nat. Mater.*, 2010, **9**, 913–917.
- 23 V. S. Saji and C. W. Lee, Selenium electrochemistry, *RSC Adv.*, 2013, **3**, 10058–10077.
- 24 Y. Wang, Y. Sun, H. Liao, S. Sun, S. Li, J. W. Ager and Z. J. Xu, Activation Effect of Electrochemical Cycling on Gold Nanoparticles towards the Hydrogen Evolution Reaction in Sulfuric Acid, *Electrochim. Acta*, 2016, **209**, 440–447.
- 25 D. González-Flores, K. Klingan, P. Chernev, S. Loos, M. R. Mohammadi, C. Pasquini, P. Kubella, I. Zaharieva, R. D. L. Smith and H. Dau, Nickel-iron catalysts for electrochemical water oxidation-redox synergism investigated by: In situ X-ray spectroscopy with millisecond time resolution, *Sustain. Energy Fuels*, 2018, **2**, 1986–1994.
- 26 I. Srejić, M. Smiljanić, Z. Rakočević and S. Štrbac, Oxygen reduction on Au(100)-like polycrystalline gold electrode in alkaline solution, *Int. J. Electrochem. Sci.*, 2016, **11**, 10436–10448.
- 27 M. R. Othman and J. Salimon, Analysis of Ethanol Using Copper and Nickel Sheet, *Malaysian J. Anal. Sci.*, 2007, **11**, 379–387.
- 28 M. S. Martín-González, A. L. Prieto, R. Gronsky, T. Sands and A. M. Stacy, Insights into the electrodeposition of Bi<sub>2</sub>Te<sub>3</sub>, *J. Electrochem. Soc.*, 2002, **149**, 546–554.

- 29 M. C. Das, R. Biswas, H. Akter, M. Haque, P. Bakshi and A. Shaikh, Cyclic Voltammetric Study of the Interaction of Biologically Important Metal Ion with Proton Pump Inhibitors, *Dhaka Univ. J. Sci.*, 2016, **64**, 25–30.
- 30 M. M. Radhi, W. A. G. Al-Dulimy and M. S. Khalaf, Electrochemical study of selenium (IV) mediated by carbon nanotubes modified glassy carbon electrode in blood medium, *Epa. - J. Silic. Based Compos. Mater.*, 2016, **68**, 90–93.
- 31 L. H. Zhang, F. Yu, Y. Shi, F. Li and H. Li, Base-enhanced electrochemical water oxidation by a nickel complex in neutral aqueous solution, *Chem. Commun.*, 2019, **55**, 6122–6125.
- 32 S. D. Giri and A. Sarkar, Electrochemical study of bulk and monolayer copper in alkaline solution, *J. Electrochem. Soc.*, 2016, **163**, H252–H259.
- 33 A. Koca, Hydrogen evolution reaction on glassy carbon electrode modified with titanyle phthalocyanines, *Int. J. Hydrogen Energy*, 2009, **34**, 2107–2112.
- 34 M. Grdeń, Semi-differential analysis of irreversible voltammetric peaks, *J. Solid State Electrochem.*, 2017, **21**, 1045–1058.
- 35 B. Šustrová, K. Štulík, V. Mareček and P. Janda, A study of the modification of the gold electrode surface with a calix[4]arene self-assembled monolayer, *Electroanalysis*, 2010, **22**, 2051–2057.
- 36 H. Pramanik and S. Basu, Cyclic Voltammetry of Oxygen Reduction Reaction Using Pt-based Electrocatalysts on a Nafion-bonded Carbon Electrode for Direct Ethanol Fuel Cell, *Indian Chem. Eng.*, 2011, **53**, 124–135.
- 37 L. Mi, Q. Ding, H. Sun, W. Chen, Y. Zhang, C. Liu, H. Hou, Z. Zheng and C. Shen, One-pot synthesis and the electrochemical properties of nano-structured nickel selenide materials with hierarchical structure, *CrystEngComm*, 2013, **15**, 2624–2630.
- 38 H. Karami, B. Kafi and S. N. Mortazavi, Effect of particle size on the cyclic voltammetry parameters of nanostructured lead dioxide, *Int. J. Electrochem. Sci.*, 2009, **4**, 414–424.
- 39 H. Shen, J. E. Mark, C. J. Seliskar, H. B. Mark and W. R. Heineman, Blocking

- behavior of self-assembled monolayers on gold electrodes, *J. Solid State Electrochem.*, 1997, **1**, 148–154.
- 40 A. O. Idris, N. Mabuba, D. Nkosi and O. A. Arotiba, Electrochemical detection of selenium using glassy carbon electrode modified with reduced graphene oxide, *Int. J. Environ. Anal. Chem.*, 2017, **97**, 534–547.
- 41 P. L. Runnels, J. D. Joseph, M. J. Logman and R. M. Wightman, Effect of pH and surface functionalities on the cyclic voltammetric responses of carbon-fiber microelectrodes, *Anal. Chem.*, 1999, **71**, 2782–2789.
- 42 A. Dauth and J. A. Love, Synthesis and reactivity of 2-azametallacyclobutanes, *Dalt. Trans.*, 2012, **41**, 7782–7791.
- 43 B. D. McCarthy, C. L. Donley and J. L. Dempsey, Electrode initiated proton-coupled electron transfer to promote degradation of a nickel(II) coordination complex, *Chem. Sci.*, 2015, **6**, 2827–2834.
- 44 C. Chia, S. S. Jeffrey and R. T. Howe, Anomalous hysteresis and current fluctuations in cyclic voltammograms at microelectrodes due to Ag leaching from Ag/AgCl reference electrodes, *Electrochem. commun.*, 2019, **105**, 106499.
- 45 B. Pérez-Fernández, D. Martín-Yerga and A. Costa-García, Electrodeposition of nickel nanoflowers on screen-printed electrodes and their application to non-enzymatic determination of sugars, *RSC Adv.*, 2016, **6**, 83748–83757.
- 46 K. J. Rountree, B. D. McCarthy, E. S. Rountree, T. T. Eisenhart and J. L. Dempsey, A Practical Beginner's Guide to Cyclic Voltammetry, DOI:10.1021/acs.jchemed.7b00361.
- 47 F. Shahdost-Fard and M. Roushani, An impedimetric aptasensor based on water soluble cadmium telluride (CdTe) quantum dots (QDs) for detection of ibuprofen, *J. Electroanal. Chem.*, 2016, **763**, 18–24.
- 48 S. Khene, S. Moeno and T. Nyokong, Voltammetry and electrochemical impedance spectroscopy of gold electrodes modified with CdTe quantum dots and their conjugates with nickel tetraamino phthalocyanine, *Polyhedron*, 2011, **30**, 2162–2170.

- 49 R. Maallah, A. Moutcine, C. Laghlimi, M. A. Smaini and A. Chtaini, Electrochemical bio-sensor for degradation of phenol in the environment, *Sens. Bio-Sensing Res.*, 2019, **24**, 100279.
- 50 K. V. Mokwebo, O. S. Oluwafemi and O. A. Arotiba, An electrochemical cholesterol biosensor based on a CdTe/CdSe/znse quantum dots—poly (Propylene imine) dendrimer nanocomposite immobilisation layer, *Sensors (Switzerland)*, 2018, **18**, 1–16.
- 51 J. Qian, L. Jiang, X. Yang, Y. Yan, H. Mao and K. Wang, Highly sensitive impedimetric aptasensor based on covalent binding of gold nanoparticles on reduced graphene oxide with good dispersity and high density, *Analyst*, 2014, **139**, 5587–5593.
- 52 F. Rohrbach, H. Karadeniz, A. Erdem, M. Famulok and G. Mayer, Label-free impedimetric aptasensor for lysozyme detection based on carbon nanotube-modified screen-printed electrodes, *Anal. Biochem.*, 2012, **421**, 454–459.
- 53 H. Zejli, K. Y. Goud and J. Louis, Sensing and Bio-Sensing Research An electrochemical aptasensor based on polythiophene-3-carboxylic acid assisted methylene blue for aflatoxin B1 detection, *Sens. Bio-Sensing Res.*, 2019, **25**, 100290.
- 54 A. E. Radi, J. L. A. Sánchez, E. Baldrich and C. K. O’Sullivan, Reusable impedimetric aptasensor, *Anal. Chem.*, 2005, **77**, 6320–6323.
- 55 S. Upasham, S. Bhadsavle and S. Prasad, Non-invasive monitoring of a circadian relevant biomarker from easily accessible body fluids using hybrid aqueous-ionic buffer interfaces on flexible substrates, *Anal. Methods*, 2019, **11**, 1229–1236.
- 56 Y. Dai and C. C. Liu, A simple, cost-effective sensor for detecting lead ions in water using under-potential deposited bismuth sub-layer with differential pulse voltammetry (DPV), *Sensors (Switzerland)*, 2017, **17**, 1–11.
- 57 H. Cai, Y. Wang, P. He and Y. Fang, Electrochemical detection of DNA hybridization based on silver-enhanced gold nanoparticle label, *Anal. Chim. Acta*, 2002, **469**, 165–172.

- 58 I. Grabowska, N. Sharma, A. Vasilescu, M. Iancu, G. Badea, R. Boukherroub, S. Ogale and S. Szunerits, Electrochemical Aptamer-Based Biosensors for the Detection of Cardiac Biomarkers, *ACS Omega*, 2018, **3**, 12010–12018.
- 59 J. Carlson, A. Wysoczanski and E. Voigtman, Limits of quantitation - Yet another suggestion, *Spectrochim. Acta - Part B At. Spectrosc.*, 2014, **96**, 69–73.
- 60 S. Prasad, A. P. Selvam, R. K. Reddy and A. Love, Silicon nanosensor for diagnosis of Cardiovascular proteomic markers, *J. Lab. Autom.*, 2013, **18**, 143–151.
- 61 R. Kurita, Y. Yokota, Y. Sato, F. Mizutani and O. Niwa, On-chip enzyme immunoassay of a cardiac marker using a microfluidic device combined with a portable surface plasmon resonance system, *Anal. Chem.*, 2006, **78**, 5525–5531.
- 62 H. Matsuura, Y. Sato, O. Niwa and F. Mizutani, Electrochemical Enzyme Immunoassay of a Peptide Hormone at Picomolar Levels with a 10 ng L<sup>-1</sup> level detection limit was developed for important marker for the diagnosis of heart failure ., 2005, **77**, 4235–4240.
- 63 Y. Gong, J. Hu, J. R. Choi, M. You, Y. Zheng, B. Xu, T. Wen and F. Xu, Improved LFIA for highly sensitive detection of BNP at point-of-care, *Int. J. Nanomedicine*, 2017, **12**, 4455–4466.

## 5 CHAPTER 5: Conclusions and Recommendations

### Summary

*This chapter discusses the advantages of using novel water soluble MSA-NiSe<sub>2</sub> QDs in electrochemical sensor detection methods. This chapter also gives a brief overview of the main objectives achieved. Furthermore, this chapter discusses recent trends in sensor development strategies and outlines future recommendations for optimizing the MSA-NiSe<sub>2</sub> QDs based aptasensor performance.*

### 5.1 Conclusions

In conclusion, we reported for the first time the successful production and implementation of novel MSA-NiSe<sub>2</sub> QDs in an aptasensor for the detection of the brain natriuretic peptide (BNP), a biomarker for myocardial infarction. The fabricated MSA-NiSe<sub>2</sub> QDs aptasensor is simple, rapid and easy to use displaying a high selectivity and sensitivity towards its target analyte. The colloidal poly-dispersed MSA-NiSe<sub>2</sub> QDs introduced into the aptasensor was successfully synthesized via a simple and reproducible microwave assisted method. HR-TEM studies confirmed the polydispersity of the QDs with an average diameter of 4 nm which was complemented by SAXSpace. UV-Vis studies of the QDs showed the presence of absorption peaks in the ultraviolet region (200-400 nm) which confirmed the small size of the QDs. In addition, the absorbance spectrum also revealed the direct and indirect bandgap of the QDs, which confirmed the nanophase of the material. XRD studies confirmed that the MSA-NiSe<sub>2</sub> QDs belongs to the bulk cubic phase. HR-SEM studies confirmed the successful immobilization of the aptamer with the MSA-NiSe<sub>2</sub> QDs due to the changes in structure from a spherical shape to a leaf-like structure after the immobilization with the aptamer. The MSA-NiSe<sub>2</sub> QDs on its own showed good electro active behavior confirmed by voltammetry and impedance. Because of the MSA-NiSe<sub>2</sub> QDs electrochemical characteristics, it was employed as a mediating platform between the aptamer and the sensor substrate, in this case, a screen-printed carbon electrode (SPCE). The successful detection of BNP was achieved by the newly fabricated MSA-NiSe<sub>2</sub> QDs based aptasensor, using differential pulse voltammetry (DPV) as detection protocol. It was observed that DPV showed good linearity where  $R^2 = 0.9982$ , and the limit of detection

(LOD) of the aptasensor was as low as 11.98 pg/ml with a sensitivity of 0.4513  $\mu\text{A}/\text{pg}/\text{mL}$  and a limit of quantification (LOQ) of 36.1 pg/ml.

The main goal of this research study was to develop a point-of-care (POC) detection system with high sensitivity and specificity towards BNP. South Africa is still a developing country, and as such, faces many problems within the health-care sector. This is especially true for major health players like myocardial infarction, cancer, tuberculosis etc., where patients have to wait for days or even weeks to get feedback from the doctor. This can be attributed to a short fall when it comes to medical equipment, since the conventional readily available equipment requires large sample volumes and it is invasive. This can then lead to patient uncomfotability and expensive visits to the doctor's office. Advantages of a POC sensor is that it gives results in real time, thus, reducing waiting times. In addition, the smaller the POC sensor chip the smaller the volume required for analysis, and as a result, the less money spent. POCs are also portable and thus can be distributed in areas where accesses to health facilities are poor.<sup>1</sup> One example of a portable POC sensor is a microfluidic electrochemical system as seen in Figure 5.1 below.

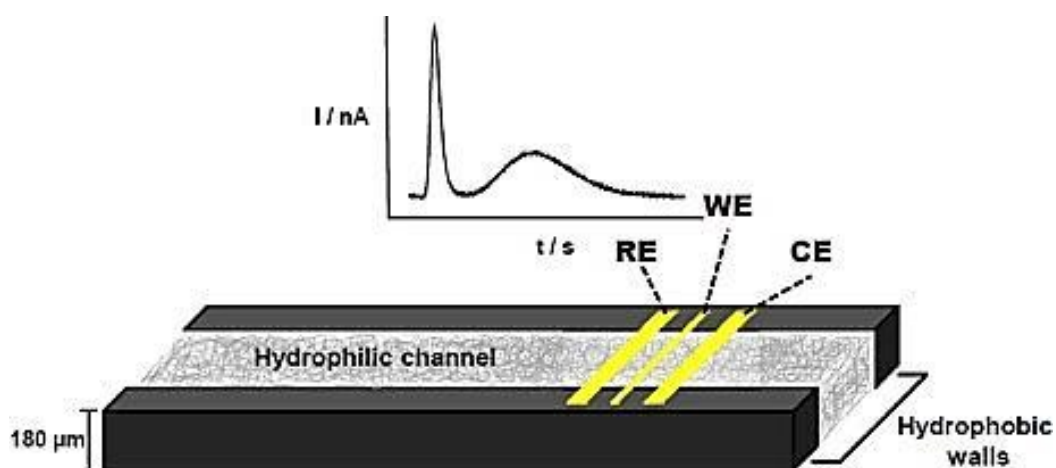


**Figure 5.1:** An Microfluidic system. Reprinted from L. Y. Shiroma, M. Santhiago, A. L. Gobbi and L. T. Kubota, Separation and electrochemical detection of paracetamol and 4-aminophenol in a paper-based microfluidic device, *Anal. Chim. Acta*, 2012, 725, 44–50.

Microfluidics is emerging as a distinct new field when it comes to research and development. Microfluidics has shown great potential in a variety of fields such as environmental monitoring, biomedicine and food analysis. Advantages of microfluidics are increased reliability, multiple sample detection, small carbon footprint and large-scale integration.<sup>2</sup> With the incorporation of nanomaterials like the novel MSA-NiSe<sub>2</sub>-QDs it can lead to microfluidic devices with excellent sensitivity, specificity, reproducibility and versatility which then can be easily commercialized as high throughput devices.<sup>3</sup> A working principle for the proposed microfluidic device could be based on a droplet-based electrochemical digital magnetofluidics system. In this system the movements of the droplets are controlled by magnetic fields that will be generated by three external magnets that will be positioned below the hydrophobic surface. An electrochemical technique such as DPV will then be used for rapid measurements of the analyte in multiple successive droplets.<sup>4</sup>

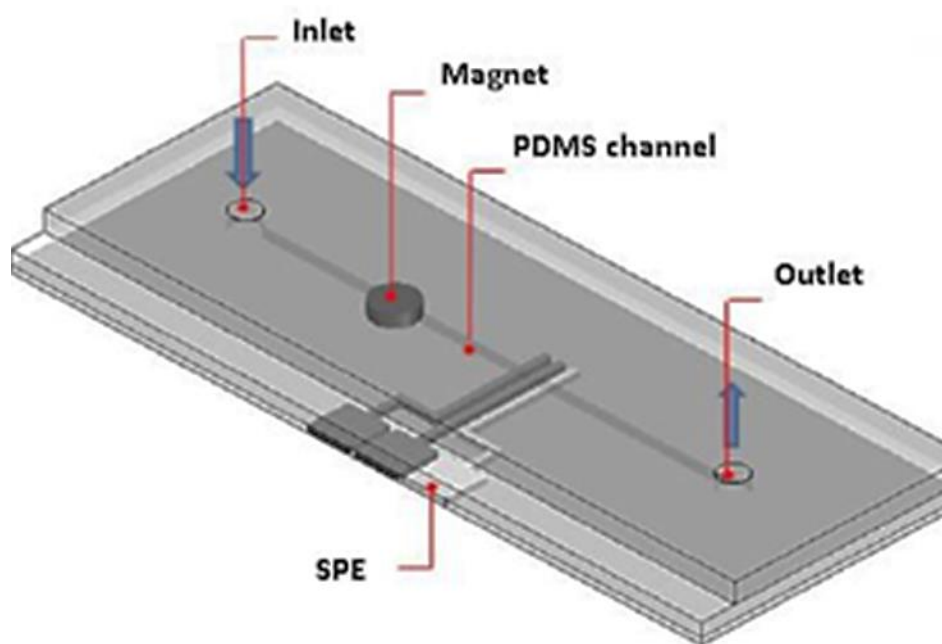


**Figure 5.2:** A magnetic microfluidic system. Reprinted from S. Lindsay, T. Vázquez, A. Egatz-Gómez, S. Loyprasert, A. A. Garcia and J. Wang, Discrete microfluidics with electrochemical detection, *Analyst*, 2007, 132, 412–416.

Moving on from microfluidics to more miniaturized systems, the end goal would be to create a wearable sensor that is inexpensive, non-invasive, simple and that will be able to detect BNP levels in bodily fluids. Wearable sensors over the years has gained a

considerable amount of attention and shown tremendous promise in a wide-range of applications. Electrochemical sensors are considerably promising due to their high performance, miniaturization and low cost.<sup>5</sup> Wearable electrochemical sensors has been applied in real-time, non-invasive analysis for monitoring metabolites and electrolytes in saliva, sweat and tears as indicators of the wearer health status.<sup>6</sup> An example of these wearable sensors is the skin based glucose sensor. This sensor can obtain important information from the skin interstitial fluid (ISF) in a non-invasive way. Researchers found a correlation between the ISF and blood glucose and created a wearable glucose sensor that is based on a reverse iontophoresis electrochemical technique.<sup>7</sup> Below is a representation of a wearable glucose based sensor.

### Wearable epidermal glucose sensors

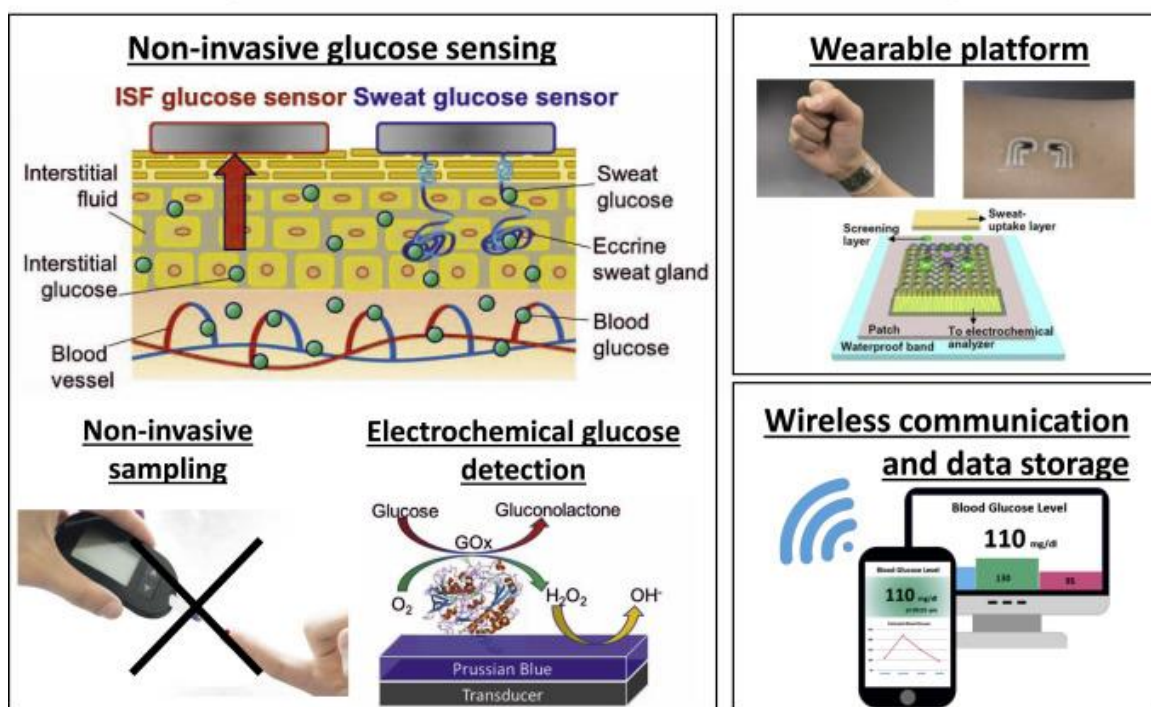


**Figure 5.3:** Representation of a wearable glucose sensor. Reprinted from J. Kim, A. S. Campbell and J. Wang, Talanta Wearable non-invasive epidermal glucose sensors : A review , *Talanta*, 2018, 177, 163–170.

An electrochemical wearable sensor for BNP detection could be developed based on the same concept as the glucose sensor due to the fact that BNP is secreted in the blood. By finding a correlation between the ISF and BNP levels found in the blood the proposed wearable sensor could be developed based on a reverse iontophoresis electrochemical technique.

## 5.2 Recommendations

- Studying various detection methods such as electrochemiluminescence, electrochemical impedance spectroscopy, photoluminescence, amperometric studies to determine the best technique for a high sensitivity and specificity for BNP detection.
- Investigating longer multivalent aptamers with multiple binding sites to improve the sensitivity and specificity for BNP detection. Recent advances in oligonucleotide synthesis are enabling up to 200 bases, which would improve the sensitivity and specificity.
- It will also be useful to focus on more than one myocardial infarction biomarker such as NT-proBNP which is also secreted in the heart the same time as BNP.
- Optimizing incubation times of BNP to improve the sensitivity and specificity of the sensor.
- More in depth research when it comes to different novel materials since it is these nanomaterials that are coupled to the aptasensor to improve its sensitivity and specificity for BNP detection. In addition, different capping agents such as 3-mercaptopropionic acid (3MPA), thioglycolic acid (TGA) etc. can be investigated to see what effect it will have on the characteristics of the NiSe<sub>2</sub> QDs.
- Specificity studies of the sensor on proteins similar to BNP such as cardiac troponin I and other cardiac markers.
- Reproducibility and stability studies of the QDs based sensor should also be investigated.
- Incorporation of the electrochemical aptasensor into microfluidic devices based on a magnetofluidics system.
- Incorporation of the electrochemical aptasensor into a wearable sensor based on the same concept as epidermal glucose sensors.

## References

- 1 W. Zhang, R. Wang, F. Luo, P. Wang and Z. Lin, Miniaturized electrochemical sensors and their point-of-care applications, *Chinese Chem. Lett.*, 2019, **6**, 1–12.
- 2 R. Antony, M. S. Giri Nandagopal, N. Sreekumar and N. Selvaraju, Detection principles and development of microfluidic sensors in the last decade, *Microsyst. Technol.*, 2014, **20**, 1051–1061.
- 3 S. Chen, Z. Wang, X. Cui, L. Jiang, Y. Zhi, X. Ding, Z. Nie, P. Zhou and D. Cui, Microfluidic Device Directly Fabricated on Screen-Printed Electrodes for Ultrasensitive Electrochemical Sensing of PSA, *Nanoscale Res. Lett.*, 2019, **14**, 3–6.
- 4 S. Lindsay, T. Vázquez, A. Egatz-Gómez, S. Loyprasert, A. A. Garcia and J. Wang, Discrete microfluidics with electrochemical detection, *Analyst*, 2007, **132**, 412–416.
- 5 D. R. Seshadri, R. T. Li, J. E. Voos, J. R. Rowbottom, C. M. Alfes, C. A. Zorman and C. K. Drummond, Wearable sensors for monitoring the physiological and biochemical profile of the athlete, *npj Digit. Med.*, 2019, **5**, 1–12.
- 6 A. J. Bandodkar and J. Wang, Non-invasive wearable electrochemical sensors : a review, *Trends Biotechnol.*, 2014, **32**, 363–371.
- 7 J. Kim, A. S. Campbell and J. Wang, Talanta Wearable non-invasive epidermal glucose sensors : A review, *Talanta*, 2018, **177**, 163–170.